Master's thesis

NTNU
Norwegian University of Science and Technology
Faculty of Engineering
Department of Energy and Process Engineering

Adrian Leirvik Larsen

Aerodynamic validation of a Formula Student race car

Master's thesis in Energy and Environmental Engineering
Supervisor: Tania Bracchi
June 2021

Photo: Adrian Leirvik Larsen

NTNU
Kunnskap for en bedre verden

NTNU revolve

Adrian Leirvik Larsen

Aerodynamic validation of a Formula Student race car

Master's thesis in Energy and Environmental Engineering
Supervisor: Tania Bracchi
June 2021

Norwegian University of Science and Technology
Faculty of Engineering
Department of Energy and Process Engineering

NTNU

Kunnskap for en bedre verden

Aerodynamic validation of a Formula Student race car

Adrian Leirvik Larsen

June 10, 2021

Abstract

This thesis work concerns the procedure for preparing and executing wind tunnel experiments in the large-scale wind tunnel at NTNU Gløshaugen. A 1/3rd scale model of the 2019 Revolve NTNU electric vehicle will be used. The preparation of the wind tunnel model and the test section setup is described in detail. Both was designed in CAD and planned to make it as realistic as possible with the time and resources available. The model was 3D printed and prepared prior to the experiments, and the result was sufficient for collecting good data from the wind tunnel tests.

A correlation study using the experimental results and Computational Fluid Dynamics (CFD) simulations for several freestream velocities and yaw angles was performed. The steady k-ϵ turbulence model was used, as it has been utilized by Revolve NTNU for the iterative aerodynamic design process for many years. Other turbulence models, both steady and unsteady, were also used for comparison.

Pressure measurements using pressure taps on the suction side of some element of the vehicle were performed, together with force measurements. Probe scalars in the CFD simulations were used at the same coordinates as the pressure taps for easy comparison. In general, good correlation was found for most of the cases. More work should be done getting a better convergence for some of the CFD simulations, to have more reliable data. However, a good foundation for studying different CFD methods have been laid down by collecting wind tunnel test data.

Sammendrag

Denne oppgaven omhandler prosedyrene for å forberede og gjennomføre eksperimenter i storskala-vindtunnelen på NTNU Gløshaugen. En vindtunnel-modell av Revolve NTNU's elektriske bil fra 2019 i en tredjedels størrelse av originalen ble brukt. Både forberedelsene av modellen og oppsettet i vindtunnelen blir beskrevet i detalj. Begge ble designet i CAD slik at oppsettet skulle bli så realistisk som mulig innenfor de tidsrammene og ressursene som var tilgjengelige. Vindtunnelmodellen ble 3D-printet og behandlet før eksperimentene, som gav tilfredsstillende resultater fra testene.

En sammenligning av resultatene fra vindtunnel-testene og resultater fra CFD-simuleringer ble gjennomført, hvor turbulensmodellen steady k-ϵ ble brukt, da denne modellen har vært utnyttet i den iterative designprosessen til aerodynamikken på bilene til Revolve NTNU i flere år. Det ble også kjørt flere turbulensmodeller for å ha et større sammenligningsgrunnlag.

Trykkmålinger ble gjort ved hjelp av taps på undersiden av flere elementer på bilen, i tillegg til kraftmålinger. Punktmålinger ble gjort i CFD-simuleringene for direkte sammenligning med vindtunnel-testene. Generelt var korrelasjonen mellom det eksperimentelle og simuleringene god. Mer arbeid bør gjøres på simuleringene for å forbedre konvergensen til enkelte av parameterne, men et godt grunnlag for videre studier av korrelasjonen for flere CFD-modeller har blitt lagt.

Problem description

The Formula Student race cars developed by Revolve NTNU use an aerodynamic wing package designed and iterated on over several years using the steady k-ϵ in Simcenter STAR-CCM+ from Siemens Digital Industries Software. While this turbulence model has been tested against several experimental cases, and also against some simple wing elements from previous Revolve NTNU race cars, no detailed flow validation projects have been performed on the full car.

This master thesis project will concern the development of a wind tunnel scale model of the 2019 Revolve NTNU Electric vehicle "Nova". The manufacturing will be performed by Fieldmade, while the preparation of the model and design of the wind tunnel setup will be performed by the author. The manufacturing and preparation process will be briefly described, along with the experimental setup in the test section of the large-scale wind tunnel in the fluid mechanics laboratory at NTNU Gløshaugen. The experiments will be executed across one week, where both load and pressure measurement data will be gathered.

Prior to the experimental tests a CFD study regarding the setup will be conducted, to decide the placement of the model in the test section, and will be used together with the results for the model scaling from the project thesis work. When all experimental data have been gathered, CFD simulations will be run for all different states (freestream velocities and yaw angles) using different turbulence models to check the correlation between simulations and experiments. Thorough analyses and discussions will be conducted to gain an increased understanding of the flow around the vehicle. This will be beneficial for the iterative design process of the aerodynamics of future Revolve NTNU electric vehicles.

Acknowledgements

I would firstly like to thank my supervisor Tania Bracchi for great discussions and helpful guidance throughout my thesis work, together with the rest of the staff at the fluid mechanics laboratory at NTNU. Also a big thank you to the Department of Energy and Process Engineering (EPT) for lending me a desktop computer for my thesis work.

Secondly I want to thank Fieldmade, and especially Brage Vasseljen, for contributing with the 3D printing of the wind tunnel model. Without your help and enthusiasm for this project it would not have been possible to execute. I also want to thank Uninett for providing access to HPC resources and Siemens Digital Industries Software for STAR-CCM+ licences, both through Revolve NTNU.

And finally a huge thank you to Revolve NTNU Formula Student team, where I have been a member for three years, and all its members in those years. It has been a pleasure working with all of you!

Contents

Figures

Tables

Chapter 1

Introduction

1.1 Background

The aerodynamics are one of the most important areas to consider in race car design. A typical Formula Student track has a lot of heavy braking and acceleration zones, as well as both high and low speed corners. That means that the performance of the aerodynamic design needs to function as well as possible across several driving conditions. To get the best out of the design, the strengths and weaknesses need to be well known.

During the design process of the aerodynamic wing package and chassis of a Formula Student car, several hundred iterations using Computer Aided Design (CAD) and Computational Fluid Dynamics (CFD) are being performed to arrive at the best possible design within the time constrains of the project. The time at hand is extremely limited, so having efficient models with a high enough accuracy is vital for being able to design and produce an aerodynamic wing package able to perform in line with our expectations.

A Formula race car uses very complex geometries for generating and affecting the flow structures and aerodynamic forces experienced while driving. That means the CFD models need to be equally complex for the results to be as accurate as possible. However, increased accuracy comes with the cost of increased computational times, which in turns decreases the amount of design iterations possible to complete.

1.1.1 Formula Student

Formula Student is the world's largest competition for engineering students, with close to 1000 teams from universities all over the world competing against each other. There are currently three different classes: combustion, electric and driverless. All classes consist of both static and dynamic events, to test both the pure performance and the reliability of the car, as well as the knowledge and design choices of the team members [1].

The static events include an Engineering Design event, where each team will

present their design choices to a selection of judges from the automobile and motorsport industry. Having solutions that are well thought through and well tested and validated are important here, as well as understanding why a design is good and what the weaknesses and potential improvements are. The other static events are the Business Plan Presentation and Cost and Manufacturing [2].

There are four different dynamic events: Acceleration, Skid Pad, Autocross and Endurance. The Acceleration event tests the acceleration of the car on a $75m$ long and $5m$ wide track. For the Skid Pad event the car will drive in a figure of eight, two laps of each circle, as shown in figure 1.1, to test the cornering abilities of the car. In the Autocross event the vehicle completes one lap around a circuit of less than $1.5km$ in length to test the overall performance of the vehicle. Finally, the Endurance event is designed to test the durability, reliability and efficiency of the car by driving approximately $22km$ with a driver change at half distance [2].

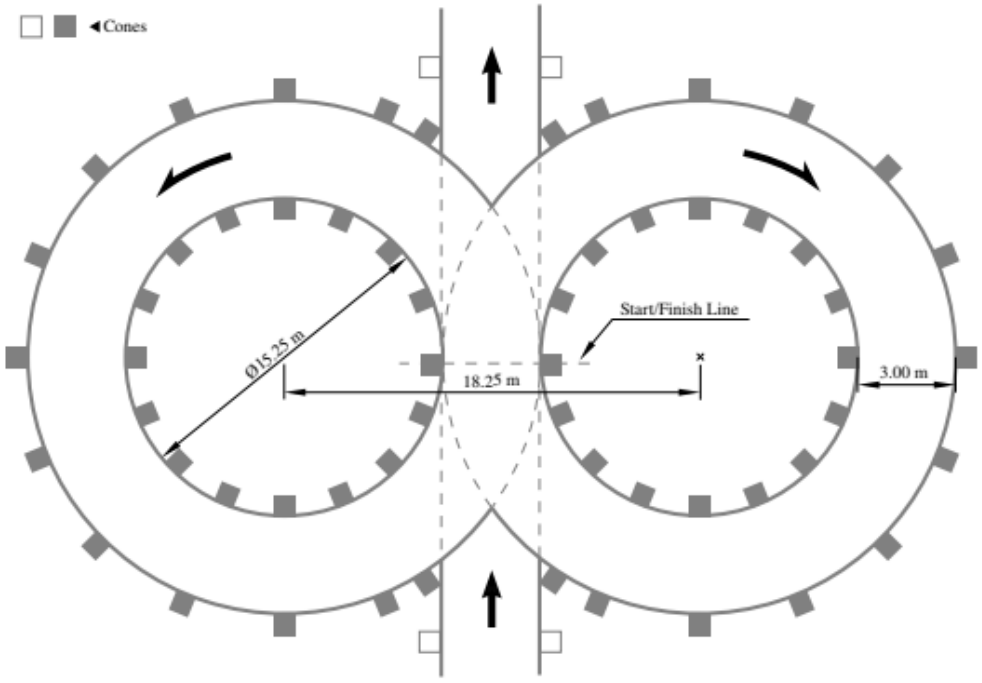

Figure 1.1: Skidpad track layout [2]

1.1.2 Revolve NTNU

Revolve NTNU Formula Student Team was founded in 2010 by a group of students wanting to apply everything they were learning in classes for something practical. They selected the Formula Student competition, and the first combustion race car was finished in 2012. Since then 10 cars have been made by the organization, built for all three classes. The last three years the focus has been on the electric and driverless classes [3]. Revolve NTNU currently ranks tenth on the official Formula

Student world ranking [4]. The 2019 electric vehicle, named "Nova", will be used in this project and master work. Figure 1.2 shows Nova during testing at NTNU Dragvoll in the autumn of 2020.

Figure 1.2: The 2019 Revolve NTNU electric vehicle "Nova". Photo: Adrian Leirvik Larsen

The 2021 Revolve NTNU team consists of more than 70 students divided across ten groups and two cars: Electric and Driverless. Over 20 fields of studies from all years of study are represented.

1.2 Outline

The objective of this thesis work is to quantify the accuracy of the CFD models used in the iterative design process of the aerodynamics of the Revolve NTNU Formula Student electric race cars and increase the knowledge and understanding of both the CFD modelling, the experimental procedures and track testing methods.

The main part of the thesis work will consider the preparation and execution of experiments in the large-scale wind tunnel at NTNU, and the correlation with CFD simulations. Chapter 2 will present the theoretical background for aerodynamics (airfoils, race car design and experimental aerodynamics), turbulence modelling in computational fluid dynamics (CFD) and additive manufacturing used in the production of the wind tunnel model. Details regarding the preparation of the wind tunnel model are presented in chapter 3, including the design choices for geometry simplifications and mounting in the wind tunnel test section, the production and assembly of the model, and the treatment of all parts and surfaces

for more accurate flow behaviour. The wind tunnel test section setup will also be described, elaborating on the choices for mounting of the model and the measurement data obtained. Chapter 3 will also include the CFD simulation setup for the different steady and unsteady RANS turbulence models and meshing methods, together with an explanation and justification of the models used.

The results for both the experimental tests and the CFD simulations, and comparisons between these, will be presented in chapter 4. This includes a grid dependence study, a presentation of both the force and pressure measurements for all the relevant velocity and yaw angle cases compared to the k-ϵ turbulence model, and a comparison of different steady and unsteady turbulence models to the experimental data. In chapter 5 all the results from the experiments and CFD simulations will be discussed and analyzed. A discussion regarding the wind tunnel setup and model preparation will also be presented. Finally a conclusion based on the discussions will be presented in chapter 6, and suggestions for future work will be included in chapter 7.

Chapter 2

Theory

2.1 Aerodynamics

2.1.1 Airfoils

Airfoils are one of the most characteristic and most used objects in aerodynamic theory and design. They are used to generate a lift force normal to the flow direction. Using a symmetrical airfoil at an angle of attack relative to the airflow or a non-symmetric (cambered) airfoil, a low pressure zone with higher flow velocity magnitude (suction surface) and a high pressure zone with lower flow velocity magnitude (pressure surface) is created. This pressure difference generates a force in the direction of the low pressure zone. Figure 2.1 shows the basic terminology of an airfoil. In this case the upper surface is the low pressure zone, meaning a lift force will be generated upwards. If the opposite is the case, the force direction is downwards.

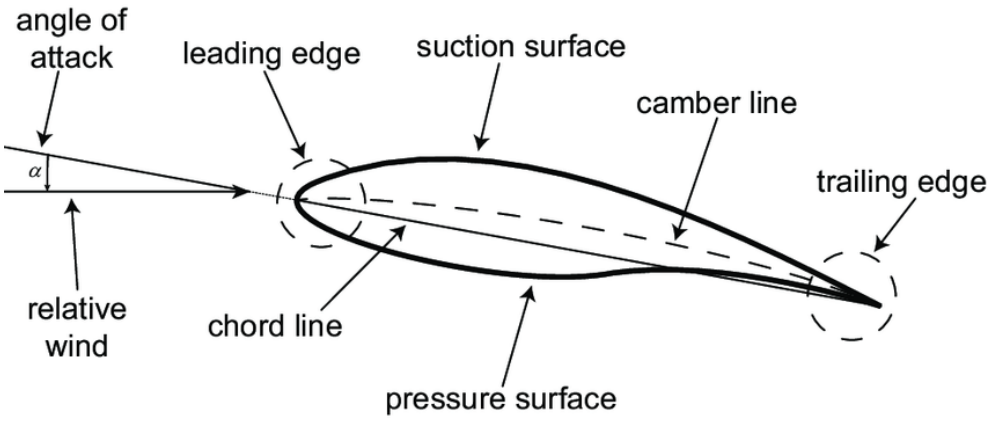

Figure 2.1: Airfoil terminology [5]

The lift and drag are often given as the dimensionless lift and drag coefficients, which are defined in equation 2.1 and 2.2 respectively. L is the lift force in N, D is the drag force in N, and S is the planform airfoil area in m^2. ρ_∞ and V_∞ is

the freestream air density in kg/m^3 and velocity in m/s respectively. The forces are divided by the dynamic pressure times the reference planform area of the airfoil [6].

$$C_{L,airfoil} = \frac{L}{\frac{1}{2}\rho_\infty V_\infty^2 S} \tag{2.1}$$

$$C_{D,airfoil} = \frac{D}{\frac{1}{2}\rho_\infty V_\infty^2 S} \tag{2.2}$$

The dimensionless pressure coefficient is defined in equation 2.3. p is the local static pressure while p_∞ is the freestream static pressure, both given in Pa.

$$C_p = \frac{p - p_\infty}{\frac{1}{2}\rho_\infty V_\infty^2} \tag{2.3}$$

Multi-element wings

A multi-element wing is a wing consisting of several wing elements, in order to increase the total camber of the wing. Figure 2.2 shows the multi-element rear wing of the 2019 Revolve NTNU electric vehicle. The principle behind this is that the boundary layer is energized between each element, meaning that the angle of attack relative to the freestream flow can be increased to extend the total low pressure area and the overall camber of the wing, thus generating more lift (or downforce/negative lift in this case) [7].

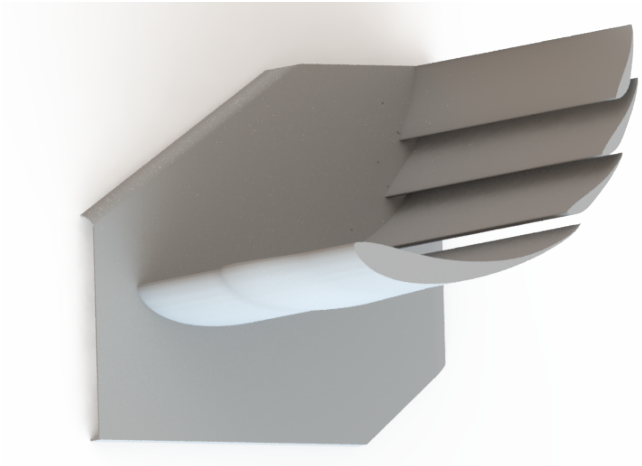

Figure 2.2: Multi-element rear wing with endplate of the 2019 Revolve NTNU electric vehicle. Rendered section view from SolidWorks

Wing tip vortices and endplates

On a finite airfoil shaped wing the pressure difference between the high and low pressure surface cannot be maintained close to the wing tip, resulting in a lower

lift force near the tips. Due to this pressure difference the air from the high pressure side will flow around the wing tip to the low pressure side, shedding a vortex. Figure 2.3 shows this effect. The vortex strength is directly related to the magnitude of the lift, and the combined effect of the vortices on each tip will create a downwash effect downstream in the wake of the wing.

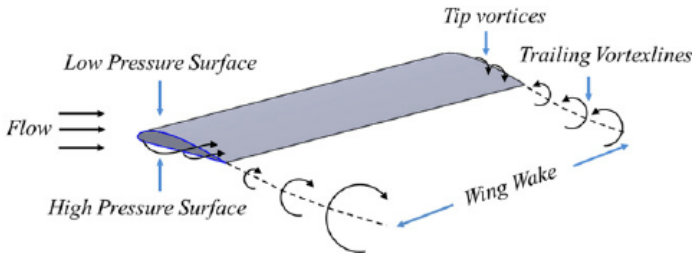

Figure 2.3: Development of wing tip vortices behind a finite wing [8]

By adding an endplate to the tip of a finite wing, as shown in figure 2.2, the leakage of the high pressure air moving around the tip towards the low pressure zone will be reduced. This will result in the pressure difference between the high and low pressure surfaces being maintained better, thus improving the lift near the wing tips and reducing the induced drag. An endplate will effectively increase the aspect ratio (AR) of the wing, defined in equation 2.4. b is the wing span in m, meaning that the aspect ratio is a measure of the width of a wing compared to its chord.

$$AR = \frac{b^2}{S} \tag{2.4}$$

An increase in the aspect ratio of a wing will thus lead to increased lift and decreased induced drag [7].

2.1.2 Race car aerodynamics

When considering the aerodynamic design of a race car, downforce and drag are the two terminologies most often used. Both of them affect the performance of the car in different ways. The downforce affects the cornering performance while the drag affects the straight line speed. Downforce is equivalent to negative lift, meaning that the direction of the lift force is down towards the ground. When using lift and drag coefficients for a full race car, the reference area A is defined as the frontal area normal to the relative wind direction of the vehicle given in m^2. The expressions are given in equations 2.5 and 2.6. [7].

$$C_L = \frac{L}{\frac{1}{2}\rho_\infty V_\infty^2 A} \tag{2.5}$$

$$C_D = \frac{D}{\frac{1}{2}\rho_\infty V_\infty^2 A} \tag{2.6}$$

The tires are the only contact points between the vehicle and the ground, meaning that all forces from the car to the ground and opposite are acting in these four points. Figure 2.4 shows two cornering situations: one where the downforce is $F_z = 200kg$ ($\simeq 2000N$) and one where it is $F_z = 300kg$ ($\simeq 3000N$). The tires start to slide at a slip angle of $\beta = 4deg$. The force produced at this slip angle is $F_y \simeq 150kg$ and $F_y \simeq 230kg$, for $F_z = 200kg$ and $F_z = 300kg$ respectively, while the slip angle is lower when the same cornering force is generated for the $F_z = 300kg$ case. A higher cornering force implies a higher cornering speed [7].

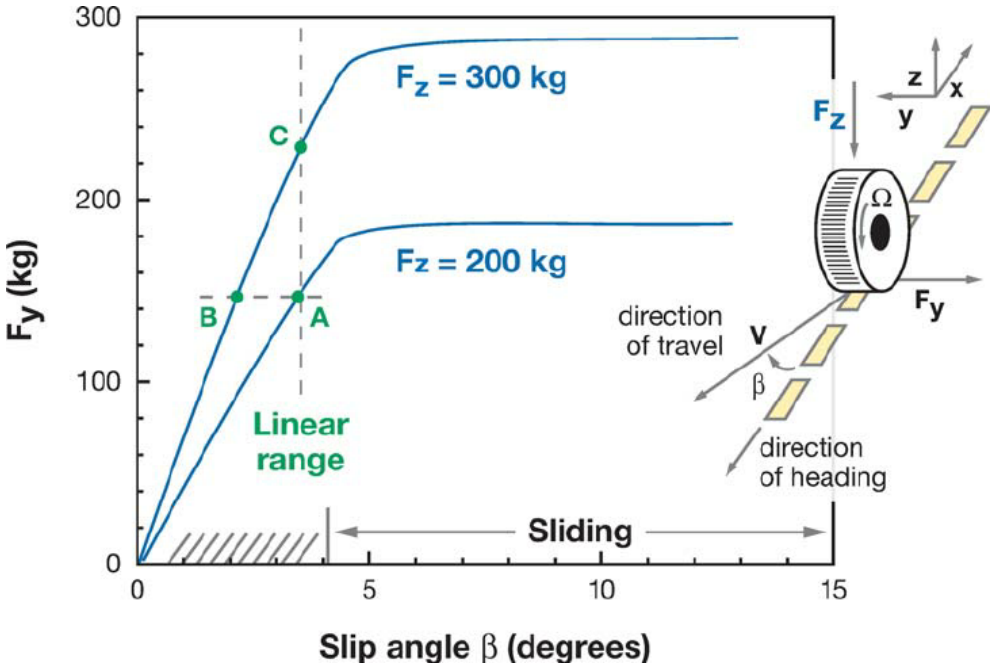

Figure 2.4: Downforce effect on tires [9]

The drag force is working in the opposite direction of the heading, meaning it limits the straight line performance at higher speeds. That means the drag affects the energy efficiency of the vehicle, as the force needed to move the car forwards has to counteract the magnitude of the drag force [7].

The resultant force from the downforce and drag generated across all parts of the car gatheres in a point called the center of pressure. The position of this point in relation to the center of mass has a large effect on how the car behaves and performs on track. If the center of pressure is located in front of the center of mass in x-direction, the front wheels will have a higher vertical force and more grip. This will lead to an oversteered car, meaning the car will turn more than the steering wheel input would suggest. The opposite happens when the center of pressure is located behind the center of mass: the car will understeer, meaning it will turn less than the steering input [7].

Figure 2.5 shows the standard terminologies used to describe the different motions in three dimensions for a race car. The x-axis is in the forward heading

direction and the rotation around this axis is called roll (ϕ). The y-axis represents the side movement normal to the direction of heading. The rotation around the y-axis is pitch (θ). Finally, the upward direction is along the z-axis, and the rotation around this axis is called yaw (ψ).

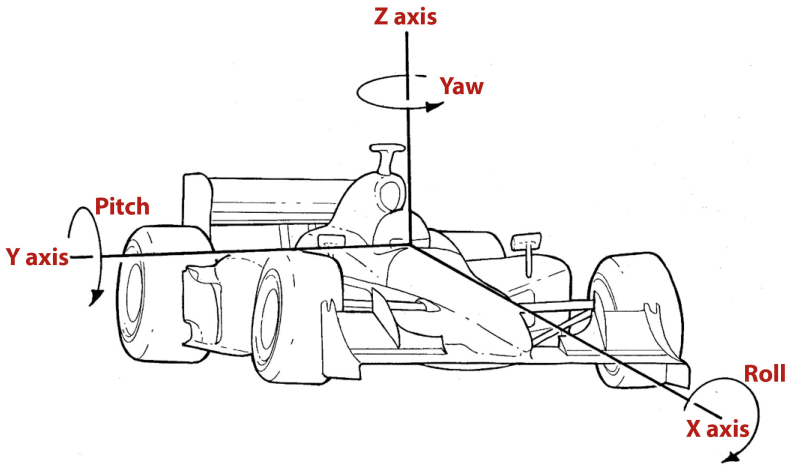

Figure 2.5: Race car coordinate system and motion terminology [10]

2.2 Numerical methods

2.2.1 RANS

Turbulence is described as random, unsteady, three dimensional fluctuations in a flow. These fluctuations are called eddies and need to be resolved in order to fully model the entire turbulent flow. This requires an extremely refined grid in the areas of turbulent flow, leading to very high computational times. However, for most engineering applications information about the details of the turbulent fluctuations is not necessary.

The Reynolds-Averaged Navier-Stokes (RANS) equations solve the time-averaged flow, giving information about the mean quantities of the flow, such as the mean velocity, mean pressure and mean stresses. Equations 2.7 to 2.11 show the RANS equations.

Continuity:

$$\frac{\partial \bar{\rho}}{\partial t} + div(\bar{\rho}\tilde{\mathbf{U}}) = 0 \tag{2.7}$$

Reynolds equations:

$$\frac{\partial \bar{\rho}\tilde{U}}{\partial t} + div(\bar{\rho}\tilde{U}\tilde{\mathbf{U}}) = -\frac{\partial \bar{P}}{\partial x} + div(\mu grad(\tilde{U})) + \left[-\frac{\partial(\overline{\bar{\rho}u'^2})}{\partial x} - \frac{\partial(\overline{\bar{\rho}u'v'})}{\partial y} - \frac{\partial(\overline{\bar{\rho}u'w'})}{\partial z} \right] + S_{M_x} \tag{2.8}$$

$$\frac{\partial \bar{\rho}\tilde{V}}{\partial t}+div(\bar{\rho}\tilde{V}\tilde{\mathbf{U}})=-\frac{\partial \bar{P}}{\partial y}+div(\mu grad(\tilde{V}))+\left[-\frac{\partial(\overline{\bar{\rho}u'v'})}{\partial x}-\frac{\partial(\overline{\bar{\rho}v'^2})}{\partial y}-\frac{\partial(\overline{\bar{\rho}v'w'})}{\partial z}\right]+S_{M_y} \tag{2.9}$$

$$\frac{\partial \bar{\rho}\tilde{W}}{\partial t}+div(\bar{\rho}\tilde{W}\tilde{\mathbf{U}})=-\frac{\partial \bar{P}}{\partial z}+div(\mu grad(\tilde{W}))+\left[-\frac{\partial(\overline{\bar{\rho}u'w'})}{\partial x}-\frac{\partial(\overline{\bar{\rho}v'w'})}{\partial y}-\frac{\partial(\overline{\bar{\rho}w'^2})}{\partial z}\right]+S_{M_z} \tag{2.10}$$

Scalar transport equation:

$$\frac{\partial \bar{\rho}\tilde{\Phi}}{\partial t}+div(\bar{\rho}\tilde{\Phi}\tilde{\mathbf{U}})=div(\Gamma_\Phi grad(\tilde{\Phi}))+\left[-\frac{\partial(\overline{\bar{\rho}u'\phi'})}{\partial x}-\frac{\partial(\overline{\bar{\rho}v'\phi'})}{\partial y}-\frac{\partial(\overline{\bar{\rho}w'\phi'})}{\partial z}\right] \tag{2.11}$$

The first term in equation 2.7 is the rate of change of density and the second is the net flow across the boundaries of the fluid element considered. For an incompressible fluid the equation simplifies to $div(U)=0$.

For equations 2.8 to 2.10 the terms on the left represent the rate of change of momentum, while the terms on the right represent the contributions from pressure forces, viscous forces and body forces.

While a detailed description of the eddies is not necessary, the effects of the turbulence on the mean flow is still needed. Turbulence models are needed to predict the Reynolds stresses ($-\rho\overline{u'^2}$, $-\rho\overline{v'^2}$, $-\rho\overline{w'^2}$, $-\rho\overline{u'v'}$, $-\rho\overline{u'w'}$, $-\rho\overline{v'w'}$) and the scalar transport terms ($\overline{u'\phi'}$, $\overline{v'\phi'}$, $\overline{w'\phi'}$) [11].

2.2.2 k-ϵ turbulence model

The k-ϵ turbulence model is a two-equation model that focuses on the mechanisms that affect the turbulent kinetic energy. $k=\frac{1}{2}(\overline{u'^2}+\overline{v'^2}+\overline{w'^2})$ is the turbulent kinetic energy while ϵ is the rate of dissipation of turbulent kinetic energy. The model uses equations 2.12 and 2.13 for k and ϵ respectively. S_{ij} is the mean rate of deformation.

$$\frac{\partial \rho k}{\partial t}+div(\rho k\mathbf{U})=div\left[\frac{\mu_t}{\sigma_k}gradk\right]+2\mu_t S_{ij}\cdot S_{ij}-\rho\epsilon \tag{2.12}$$

$$\frac{\partial \rho \epsilon}{\partial t}+div(\rho \epsilon\mathbf{U})=div\left[\frac{\mu_t}{\sigma_\epsilon}grad\epsilon\right]+C_{1\epsilon}\frac{\epsilon}{k}2\mu_t S_{ij}\cdot S_{ij}-C_{2\epsilon}\rho\frac{\epsilon^2}{k} \tag{2.13}$$

To calculate the Reynolds stresses the Boussinesq relationship is used, given in equation 2.14.

$$-\rho\overline{u_i'u_j'}=\mu_t\left(\frac{\partial U_i}{\partial x_j}+\frac{\partial U_j}{\partial x_i}\right)-\frac{2}{3}\rho k\delta_{ij}=2\mu_t S_{ij}-\frac{2}{3}\rho k\delta_{ij} \tag{2.14}$$

The eddy viscosity μ_t is given in equation 2.15.

$$\mu_t = C\rho vl = \rho C_\mu \frac{k^2}{\epsilon} \tag{2.15}$$

For the boundary conditions the values for k and ϵ need to be known. When they are not available, which usually is the case for industrial applications, the turbulence intensity T_i and characteristic length of the equipment L may be used using the relations shown in equation 2.16.

$$k = \frac{2}{3}(U_{ref}\, T_i)^2 \qquad \epsilon = C_\mu^{\frac{3}{4}} \frac{k^{\frac{3}{2}}}{l}, \quad l = 0.07L \tag{2.16}$$

σ_k, σ_ϵ, $C_{1\epsilon}$, $C_{2\epsilon}$ and C_μ are dimensionless adjustable constants. The standard k-ϵ model uses the following values [11]:

$$C_\mu = 0.09, \quad \sigma_k = 1.00, \quad \sigma_\epsilon = 1.30, \quad C_{1\epsilon} = 1.44, \quad C_{2\epsilon} = 1.92$$

2.2.3 k-ω SST turbulence model

Due to the fact that the k-ϵ turbulence model provides unsatisfactory results for the near-wall flow with adverse pressure gradients, a hybrid model using the k-ϵ model in the flow far from the wall and the k-ω model close to the wall. The equation for the Reynolds stresses for the k-ω are the same as for the k-ϵ given in equation 2.14, using the eddy viscosity given in equation 2.17, while the transport equation for k is the same as for the standard k-ω and is given in equation 2.18.

$$\mu_t = \rho \frac{k}{\omega} \tag{2.17}$$

$$\frac{\partial(\rho k)}{\partial t} + div(\rho k \mathbf{U}) = div\left[\left(\mu + \frac{\mu_t}{\sigma_k}\right) grad(k)\right] + \left(2\mu_t S_{ij} \cdot S_{ij} - \frac{2}{3}\rho k \frac{\partial U_i}{\partial x_j}\delta_{ij}\right) - \beta^* \rho k \omega \tag{2.18}$$

The ω-equation is given in equation 2.19.

$$\frac{\partial(\rho \omega)}{\partial t} + div(\rho \omega \mathbf{U}) = div\left[\left(\mu + \frac{\mu_t}{\sigma_{\omega,l}}\right) grad(\omega)\right] + \gamma_2 \left(2\rho S_{ij} \cdot S_{ij} - \frac{2}{3}\rho \omega \frac{\partial U_i}{\partial x_i}\delta_{ij}\right)$$

$$-\beta_2 \rho \omega^2 + 2\frac{\rho}{\sigma_{\omega,2}\omega} \frac{\partial k}{\partial x_k} \frac{\partial \omega}{\partial x_k} \tag{2.19}$$

σ_k, $\sigma_{\omega 1}$, $\sigma_{\omega 2}$, γ_2, β_2 and β^* are dimensionless adjustable constants. The SST k-ω model uses the following revised values [11]:

$$\sigma_k = 1.0, \quad \sigma_{\omega,1} = 2.0, \quad \sigma_{\omega,2} = 1.17, \quad \gamma_2 = 0.44, \quad \beta_2 = 0.083, \quad \beta^* = 0.09$$

2.3 Experimental aerodynamics

Experimental aerodynamics are physical tests usually performed in a wind tunnel or a similar installation. A wind tunnel test is also considered a simulation and is used together with CFD to check and validate the performance and flow structures of the real object in its original operating environment. When performing experimental tests and CFD simulations, these conditions need to be replicated as closely as possible. Important parameters to pay attention to include the Reynolds number for the ratio between inertial and viscous forces, the blockage ratio in the wind tunnel test section, and experimental setup and mounting of the model.

The definition of the Reynolds number is given in equation 2.20. L is the reference length in m, in this case the length of the wind tunnel model, and ν is the kinematic viscosity. When doing experimental analyses in a wind tunnel the cross-sectional area of the test section is usually fixed. That means the wind tunnel model needs to be scaled accordingly to keep the blockage ratio at an acceptable level. As can be seen in the expression for the Reynolds number, when the reference length of the model decreases the velocity have to increase to have matching Reynolds numbers. It is possible to use a pressurized wind tunnel or change the air temperature to alter the density and viscosity of the air. This is however a lot more complicated and is not possible in the wind tunnel facilities used for this project.

$$Re = \frac{\rho V_\infty L}{\mu} = \frac{V_\infty L}{\nu} \tag{2.20}$$

The blockage ratio is defined in equation 2.21. The frontal area of the wind tunnel model A_{model} needs to be small enough for the wall effects being present due to the tunnel walls to be as small as possible, while still having a representative geometry to be able to match the Reynolds numbers as closely as possible. A_{tunnel} is the wind tunnel cross-sectional area at the location of the wind tunnel model [12].

$$BR = \frac{A_{model}}{A_{tunnel}} \tag{2.21}$$

Having a too large blockage ratio will significantly increase the velocity of the air flowing around the model. This will lead to deviations in the force coefficients measured and the flow structures around the model compared to the original object. Figure 2.6 shows the effect of blockage, where the flow is confined (B), hence accelerated, as seen from the streamline distribution compared to the open flow (A). There are several different definitions on what the maximum blockage ratio should be in order to obtain sufficient results from experiments in a wind tunnel: Delery et al [12] suggest below 16%, Rae et al [13] suggest below 7.5%, while Hucho [14] suggests less than 10%.

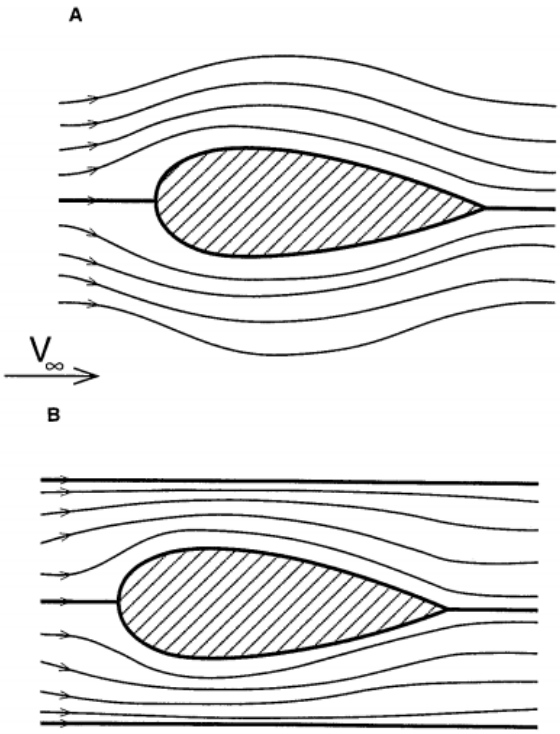

Figure 2.6: Streamlines near a body in an open freestream (A), and when constrained by two rigid walls (B) [7]

2.4 Additive manufacturing

Additive manufacturing, more commonly known as 3D printing, is a range of techniques based on adding layer-upon-layer to create a component from a virtual 3D model. Compared to subtractive manufacturing, where material has to be removed from a solid block, much more complex geometries may be achieved while less material is wasted [15].

2.4.1 FFF

Fused Filament Fabrication (FFF) belongs to the material extrusion family. The material comes in filament form and is being built layer-by-layer in a pre-determined pattern. The material is being melted in the extrusion head and the nozzle before being applied to the part, where it solidifies. This technique uses a 3-axis system that allows movement in x-, y- and z-direction. When one complete layer is finished the extrusion head steps up in z-direction and applies the next layer until the part is completed.

As this is an extrusion technique using three axes, a support structure is needed for parts with overhang. This structure will be removed when the printing process is done leading to a lower surface quality, so care needs to be taken when deciding

the printing orientation. Another important aspect to keep in mind is that the bond strength between each layer is lower than the base strength of the material. For ABS (Acrylonitrile Butadiene Styrene) the tensile strength in the x- and y-directions may be up to four times as great as in z-direction.

Figure 2.7 shows the schematics of an FFF printer, while figure 2.8 shows the FFF printing process. It can be seen how the support structure is included in the part when the printing job is finished. All of this has to be removed and the surface will need additional treatment [15] [16].

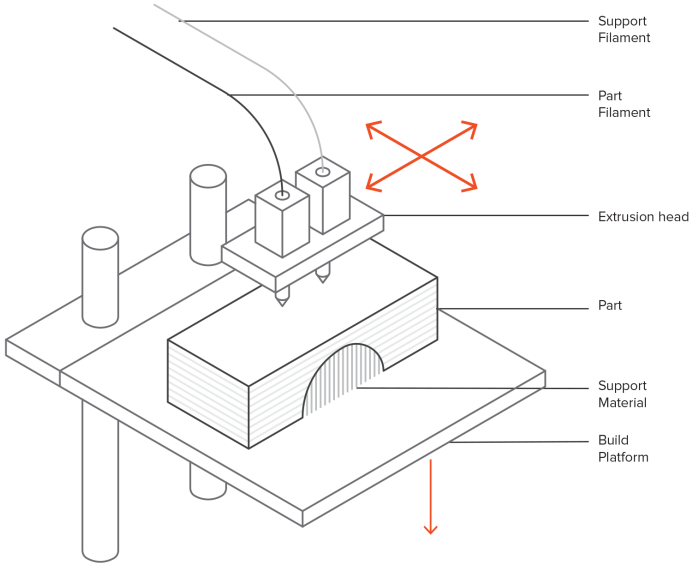

Figure 2.7: Schematics of an FFF printer [15]

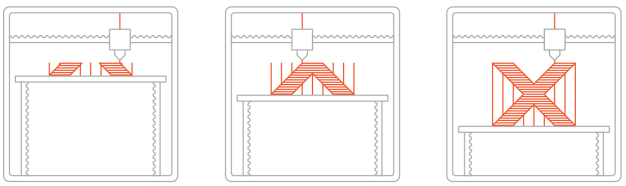

Figure 2.8: The FFF printing process [15]

Chapter 3

Methods

First the design, assembly and preparation of the wind tunnel scale model will be described. Then the wind tunnel methodology will be explained, including the setup of the model itself and the integration of the force and pressure measurement solutions. The CFD modelling techniques will then be presented for the different turbulence models and meshing strategies.

3.1 Wind tunnel model

3.1.1 Design

The wind tunnel model is based on the 2019 Revolve NTNU Electric Formula Student race car. During my project thesis work, the scaling was chosen to be 1/3rd (33%) of the original size, due to manufacturing constraints and the blockage ratio in the test section.

The model was designed with ease of assembly and durability in mind, while the main geometric features of the aerodynamic design had to be preserved. Simplifications of the geometry were made in the suspension and wheel assemblies. As the wheels will be stationary, compared to rotating for the original vehicle, the wheels were filled both in the CFD and wind tunnel model. The driver and cockpit are also parts that are tricky to model accurately, due to movement and complexity. Therefore the cockpit was filled and a simplified driver model was used for both CFD and experiments.

Where possible, all brackets and attachment point were designed so that the majority of the forces are acting towards a wall, lowering the strength requirements for adhesives used to attach all parts. The exceptions to this philosophy are the front and rear wing attachment solutions. Here extra care had to be taken during the assembly and bonding process to make sure the model could handle the forces acting on each element.

For mounting in the wind tunnel test section, a circular hole of 25mm diameter and 30mm height was added in each wheel. The inside of the monocoque was made hollow to make room for a pressure scanner. Pressure tapping holes were

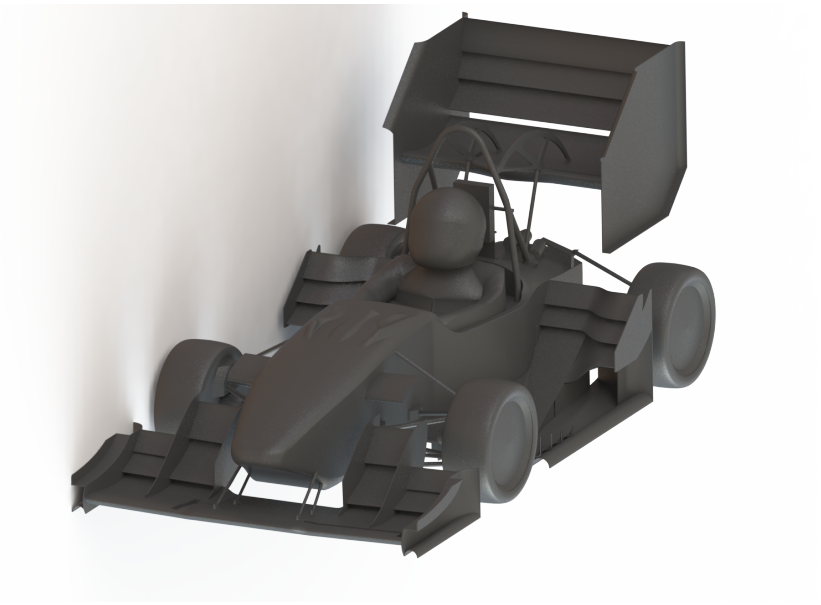

Figure 3.1: Scale model CAD. Render from SolidWorks

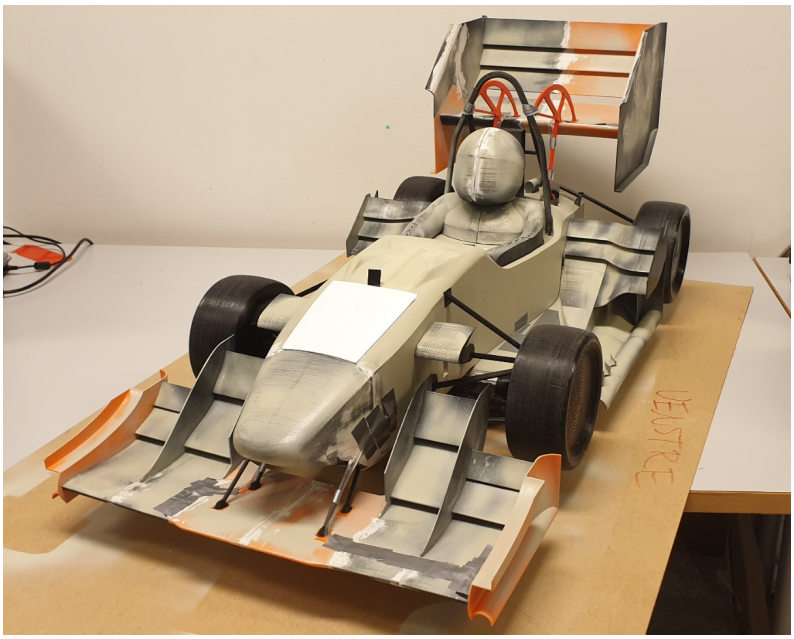

Figure 3.2: Scale model. Photo: Adrian Leirvik Larsen

added to the front wing, rear wing and undertray to be able to measure the static pressure on the suction side of these elements. Additional holes were made in the monocoque for the tubing to the pressure tapping location, as well as for the power and Ethernet cables for the pressure scanner. Two lids in the monocoque were made in order to have easy access to the scanner during the mounting.

Below are two examples of how the printed parts compare to the parts rendered in CAD. Figures 3.3 to 3.5 show the front left suspension and wheel, and front wing assemblies respectively.

(a) Wind tunnel model. Photo: Adrian Leirvik Larsen

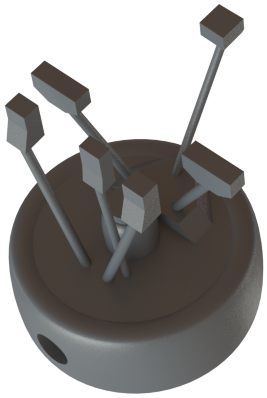

(b) CAD model. Render from SolidWorks

Figure 3.3: CAD vs reality of front left suspension assembly

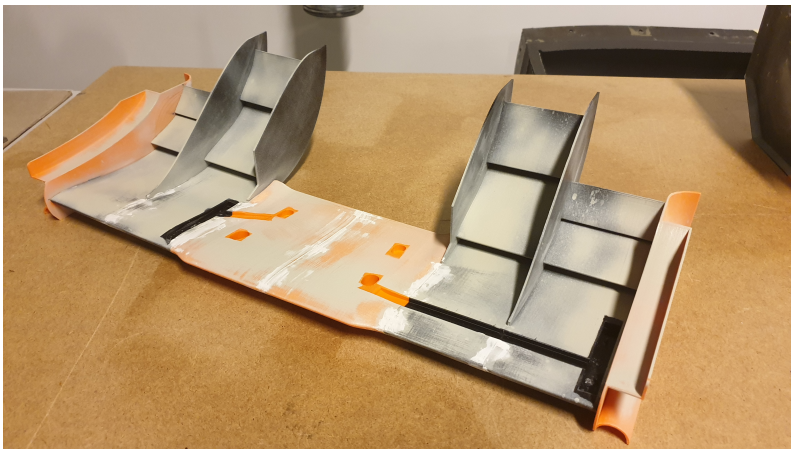

Figure 3.4: FW of wind tunnel model. Photo: Adrian Leirvik Larsen

3.1.2 Manufacturing

The manufacturing was performed by Fused Filament Fabrication (FFF), using the Ultimaker S3 printer. A combination of PLA and Tough PLA was used for the

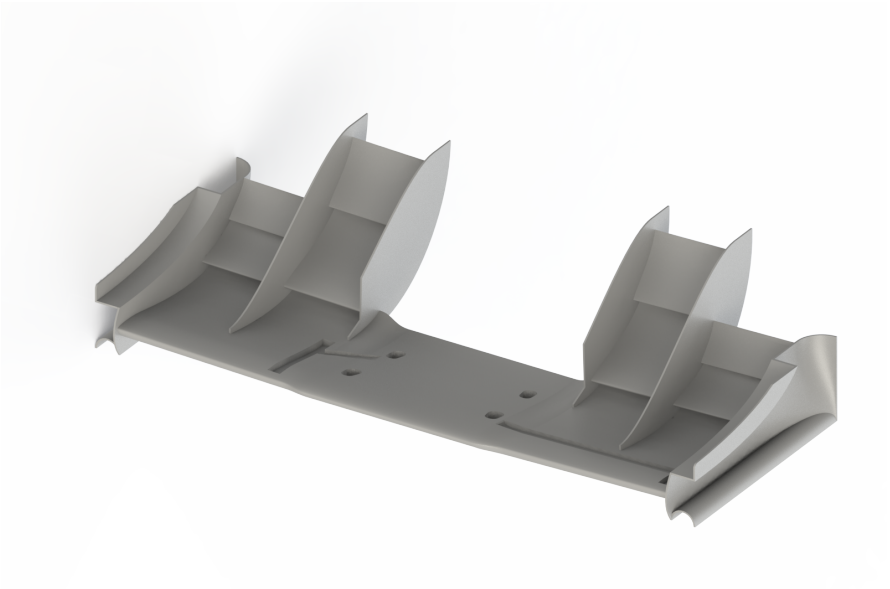

Figure 3.5: FW CAD model. Render from SolidWorks

model, based on the strength requirements for each part. The technical datasheets for both filaments are given in appendix D.

The suspension rods, and the front and rear wing fasteners are the most critical parts in terms of loads. Therefore these parts were made using Tough PLA. The rest of the parts were made using PLA.

For the printing of the parts the model was split into several smaller components to ease the production and optimize the surface finish on the parts that are most important for the airflow around the model.

3.1.3 Assembly and preparation

During the assembly process, the brackets and attachment points were sanded using a sanding paper roughness of 60 to 240, in order for all parts to fit together. The surfaces of all parts were sanded using a roughness of 240. In order to treat areas with irregularities, spackling paste was applied and sanded afterwards. Finally, all parts were clear coated using SprayMax 2K Clear Coat and sanded with paper of roughness 1200.

All parts were attached together using Loctite All Plastics Super Glue. The bonding surfaces were cleaned using isopropyl alcohol, before applying the adhesive. As mentioned earlier, extra care had to be taken when attaching the front and rear wings, due to the direction the forces are acting on the bonding surface.

3.2 Experiments

3.2.1 NTNU large-scale wind tunnel

The large-scale wind tunnel at NTNU Gløshaugen in the fluid mechanics laboratory is the largest wind tunnel of its kind in Norway. During the 2020-2021 academic year the test section underwent a major refurbishment. The main new features are increased optical access to the test section, a removable active turbulence grid and a traversing system for airflow measurement probes [17].

Specifications

The test section is $11,000mm$ long (x-direction), $2700mm$ wide (y-direction) and $1800mm$ high (z-direction). The front of the force balance plate is located $3340mm$ downstream of the inlet. The maximum wind velocity is around $V_\infty = 25m/s$, while the turbulence intensity in the empty test section is about $TI = 1\%$.

Due to the refurbishment not being completed in time for my experiments, some of the new features had not been installed, and was thus not available. This included PIV measurements and the pressure traversing system. The wind speed was also limited to around $V_\infty = 60km/h = 16.67m/s$.

3.2.2 Experimental setup

Each wheel of the wind tunnel model was equipped with a hole for attaching supports from the force balance to the model. As only the forces acting on the model is of interest, these supports should not be in contact with anything but the model and force balance plate. Therefore a wooden plate was made with a hole for each support to cover the gap in the wind tunnel floor. Figure 3.6 shows the supports mounted on the force balance and the placement of the plate to cover up the floor. The supports were placed so that the center point between them is coincident with the center point of the force balance plate.

One of the greatest limitation in this experiment compared to a road test of the vehicle is the absence of a moving ground. The ground effect generated by the proximity of the vehicle to the ground will be weaker when the ground is stationary. An option is to place the model on a belt moving at the same speed as the air passing the vehicle. While this would have been the most accurate solution it was deemed too time and resource consuming for the scope of this project. However, instead of placing the model on the wind tunnel floor, it was raised $100mm$ from the ground and a plate was mounted underneath (called "ground effect plate"). The reason is to move the model out of the boundary layer created at the wind tunnel floor. When a ground vehicle is driving over a stationary road surface this boundary layer does not exist, meaning that the results will deviate if no action is taken to limit this error. Figure 3.7 shows how the boundary layer and velocity profile differ between a road test (A) and wind tunnel experiment (B). It can clearly be seen how the velocity profile between the underside of the vehicle and

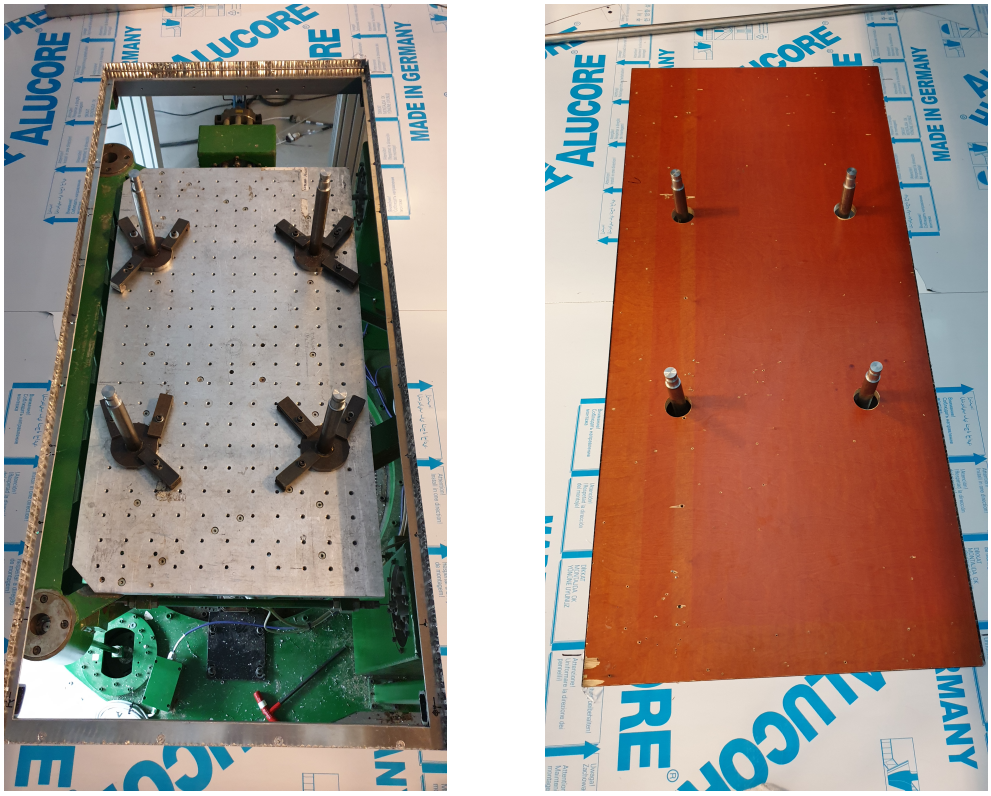

Figure 3.6: Mounting of model supports and floor plate. Photo: Adrian Leirvik Larsen

ground differ between the two cases due to the boundary layer developing upstream, and this will affect the flow structures and forces generated, both overall and local.

While adding a ground effect plate will not be as accurate as a rolling floor, it gives a better representation than mounting the model on the floor. The setup is displayed in figure 3.9. The tubes going across the test section are mounted on supports along the rails going along the entire length of the test section.

Measurements have been performed in an empty test section to estimate the boundary layer thickness at various locations. As the wind tunnel test section refurbishment was set to be completed shortly before my experiments were due to commence, data from the old test section had to be considered when deciding the experimental setup. Figure 3.8 shows the velocity profile at the location of the wind tunnel model. It can be seen that the boundary layer at this location is estimated to be around $200mm$ at the floor. The boundary layer measurements performed in the new test section show a boundary layer thickness of around 250 to $300mm$.

Due to challenges in mounting the tubes underneath the ground effect plate at the side of the test section and being able to support its weight, the ground effect

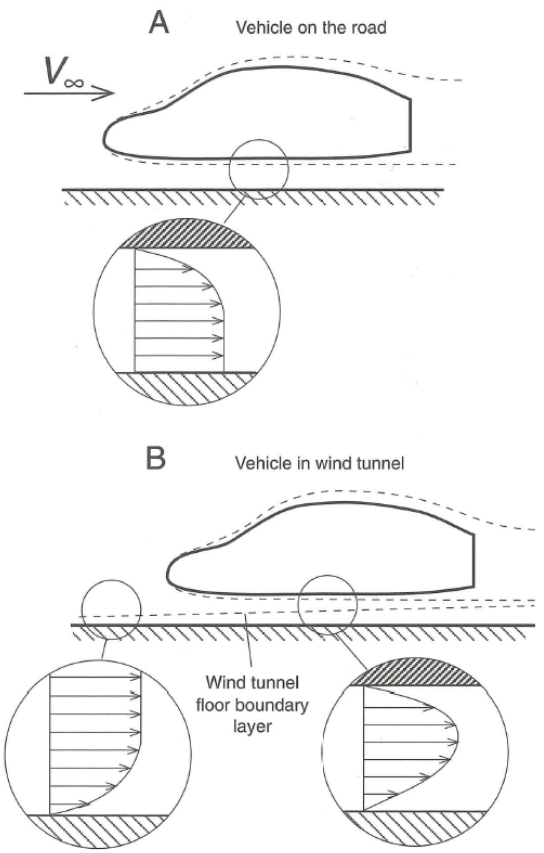

Figure 3.7: Differences between a vehicle on the road (A) and vehicle in a wind tunnel (B) for the boundary layer development on the ground [7]

plate was placed 100mm above the floor. However, as the most significant changes in the fluid velocity happens closer to the wall, this was considered sufficient.

During my project thesis work a CFD study on the effects of the simplifications of having a stationary ground and wheels was performed. A comparison between mounting the wind tunnel model on the wind tunnel floor and lifting it out of the boundary layer using an additional plate was also made. The results are summarized in table 3.1.

The numbers from the CFD simulations show a 17% decrease in lift and a 5% decrease in drag, when the ground is fixed (no-slip condition) and the wheels are stationary (zero rpm) for the full-scale case. For the scaled case the decrease is 23% and 14% respectively. When the scaled model was placed on a plate raised 100mm from the ground surface, the differences are less significant (17% and 11%). It was therefore decided to use the ground effect plate setup, as shown in figure 3.9.

When scaling down to $1/3rd$ of the original vehicle size, the freestream velo-

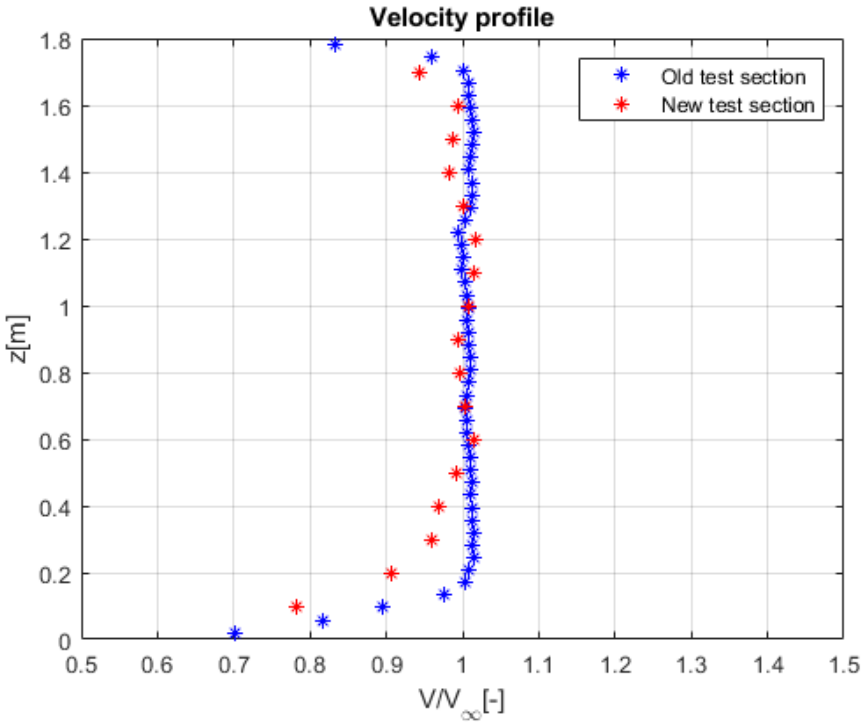

Figure 3.8: Velocity profiles for old and new test section. Measurments by Tania Bracchi, NTNU (old) and Leon Li, NTNU (new)

Table 3.1: Simulation domain study summary

Case	$C_L[-]$	$C_D[-]$	Rear DF[%]	No. of cells	CPU time[s]
Standard	4.57	1.52	43.7	$3.88*10^7$	$1.79*10^6$
Stationary ground	3.87	1.45	52.2	$3.97*10^7$	$1.81*10^6$
Stationary wheels	4.48	1.52	43.7	$3.88*10^7$	$1.83*10^6$
Stationary wheels + ground	3.79	1.45	52.5	$3.97*10^7$	$1.83*10^6$
Standard $20km/h$	4.11	1.49	44.7	$3.88*10^7$	$1.82*10^6$
Scaled	3.97	1.53	43.2	$7.05*10^6$	$3.75*10^5$
Scaled, stat. wheels + ground	3.06	1.31	56.4	$6.93*10^6$	$3.77*10^5$
Scaled with plate	3.29	1.36	49.5	$7.09*10^6$	$3.78*10^5$

city V_∞ also has to be adjusted so that the Reynolds number Re, defined in equation 2.20, matches for the different cases. That means for a $1/3rd$ scale model the velocity is three times larger than for the full-scale vehicle. The freestream velocity $V_\infty = 60km/h = 16.67m/s$ in the wind tunnel experiments will thus be equivalent to $V_\infty = 20km/h = 5.56m/s$ for a road test of the vehicle.

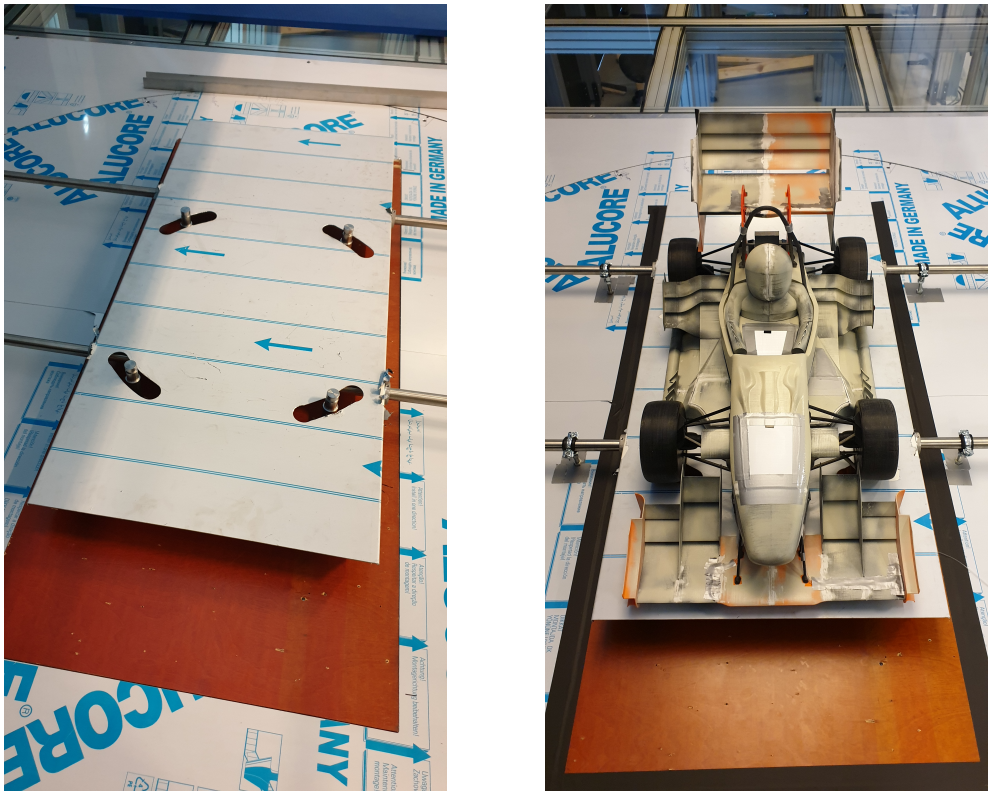

Figure 3.9: Mounting of ground effect plate and wind tunnel model. Photo: Adrian Leirvik Larsen

3.2.3 Measurement setup, procedure and data acquisition

During the wind tunnel experiments freestream velocities between $V_\infty = 10km/h = 2.78m/s$ and $V_\infty = 60km/h = 16.67m/s$, corresponding to the Reynolds numbers presented in table 3.2. The length scale is $L = 1000mm = 1m$ and the kinematic viscosity is $\nu = 1.48 * 10^{-5} m^2/s$.

Table 3.2: Freestream velocities and Reynolds numbers

$V[km/h]$	$V[m/s]$	$Re[-]$
10	2.78	$1.88*10^5$
20	5.56	$3.76*10^5$
30	8.33	$5.63*10^5$
40	11.11	$7.51*10^5$
50	13.89	$9.39*10^5$
60	16.67	$1.13*10^6$

Force balance

A 6-component force balance from Carl Schenck AG is located underneath the test section of the wind tunnel. Each load cell gives a voltage in V, which needs to be converted to a load in N. To find the correct conversion factors a calibration needs to be performed, by adding known loads to each cell individually. This gives a conversion matrix to convert from voltages to forces and forces to force moments. The uncertainties are estimated to be $\pm 10mg$ when converted from N to kg [18].

The force balance consists of three vertical and three horizontal load cells, which are being converted into the forces and moments in x-, y- and z-direction (drag, side and lift forces, and roll, pitch and yaw moments).

Freestream pressure/velocity

A pitot-static tube was used to measure the total and static pressures in the freestream airflow. The difference between these readings gives the dynamic pressure used to estimate the airspeed relative to the wind tunnel test section walls. A Setra Model 239 pressure transducer reads a voltage in V, which needs to be converted to pressure in Pa using the rotational speed in rpm of the wind tunnel fan and the output voltage. The accuracy is given as $\pm 0.14\% FS$ [19].

The pitot-ptatic tube was placed $800mm$ upstream of the forward-most point of the scale model, $350mm$ from the ground and $200mm$ from the test section wall ($1150mm$ from the center). The setup is shown in figure 3.10.

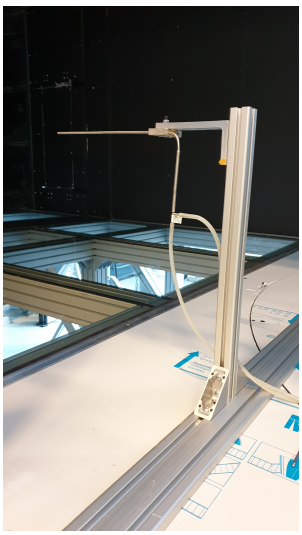

Figure 3.10: Pitot-static tube. Photo: Adrian Leirvik Larsen

The calibration of the pressure transducer was performed using the FCO560 Pressure/Flow Calibrator. The accuracy is given as $< 0.1\%$ [20]. The pressure and voltage was read for several rpm values for the fan to find a constant with unit Pa/V to convert the voltage readings in V from the transducer into pressure in Pa,

which was then converted into velocity in m/s by the dynamic pressure relation $q = \frac{1}{2}\rho_\infty V_\infty$, where q is the dynamic pressure in Pa.

The atmospheric pressure p_{atm} was measured each day experiments in the wind tunnel was performed and used to correct the air density ρ_∞ for calculating the freestream velocity V_∞. The atmospheric pressure readings are presented in table 3.3. A thermocouple was used to measure the temperature T in K in the test section, which is also needed to calculate the air density.

Table 3.3: Atmospheric pressure readings

Day	Date	$p_{atm}[mmHg]$	$p_{atm}[Pa]$
1	30.03	755.4	100,712
2	31.03	759.8	101,298
3	01.04	761.4	101,512
4	02.04	759.5	101,258
5	03.04	761.0	101,458

Pressure tapping

The wind tunnel model contained a 64-channel Scanivalve MPS4264 pressure scanner used to measure the static pressure at the suction side surfaces of the front wing main element (8 measurement points), rear wing main element (8) and undertray (11). The accuracy of the scanner is given as $\pm 0.06\% FS$ [21]. Pressure taps were installed into the parts and connected to the pressure scanner with urethane tubing. The taps were cut from a stainless steel tube of $1.1mm$ outer diameter, slightly larger than the inner diameter of the urethane tubing ($1.02mm$) to prevent leakage.

Figures 3.11 to 3.14 show the pressure tapping locations in the CFD model, which are equivalent to the tapping coordinates on the wind tunnel model. Originally a 32-channel pressure scanner was planned to be used, which is why only 27 taps were placed on the wind tunnel model. Because of this the front wing taps named 33-36 and m37-m40 ("m" stands for "mirrored" in the CFD model), undertray taps named 01-11, and the rear wing taps named 17-20 and m21-m24 were the only ones placed on the wind tunnel model. An overview is shown in table 3.4. By executing wind tunnel runs with positive and negative yaw angles ψ all data for all yaw angles was collected for all pressure taps. Symmetry was assumed for both the experiments and CFD simulations.

The pressure tapping coordinates were decided based on a combination of areas of interest and where it was possible to place the taps due to geometry shapes and sizes. The two rows in x-direction on the front and rear wings were chosen to compare the low pressure zones both close to and far away from the endplates, while the distribution along each row was to get data for different pressure gradients as far back towards the trailing edge as possible for this geometry. The taps along the y-direction on the undertray were added to measure the pressure

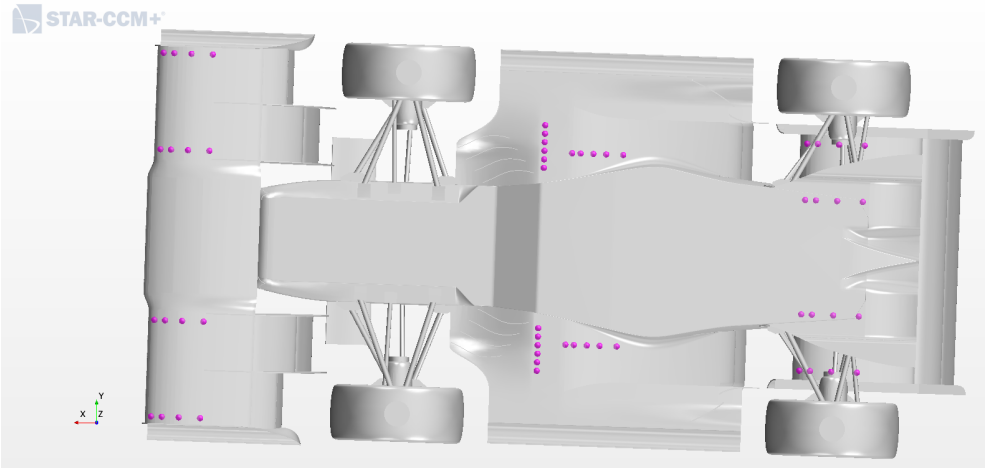

Figure 3.11: Pressure tapping placement on the full model in CFD

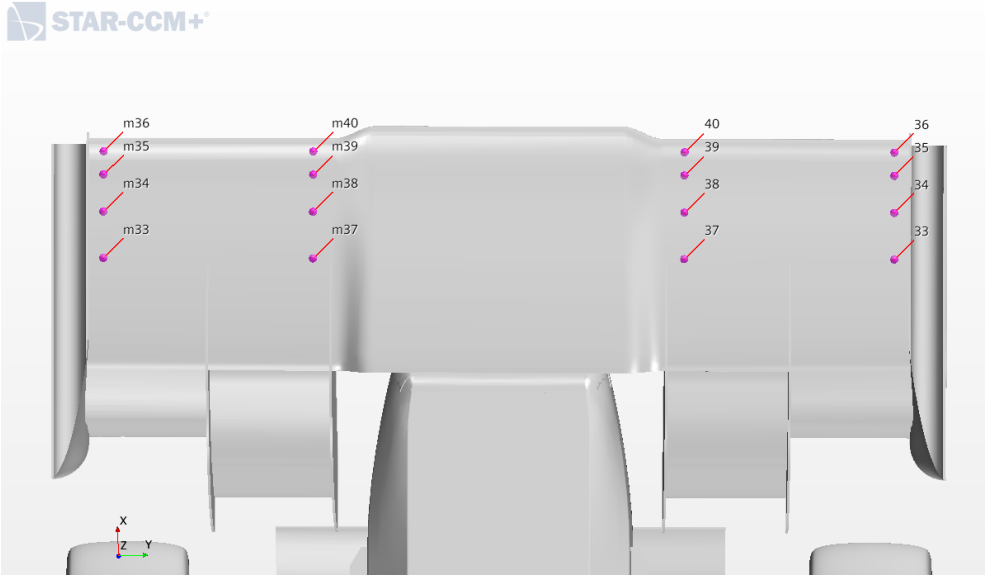

Figure 3.12: Pressure tapping placement on the front wing in CFD

differences downstream of the inlet strakes in the area of lowest ground clearance other than the underside of the chassis. Finally, the row in the x-direction along the undetray tunnel is to get data for the adverse pressure gradient in this area.

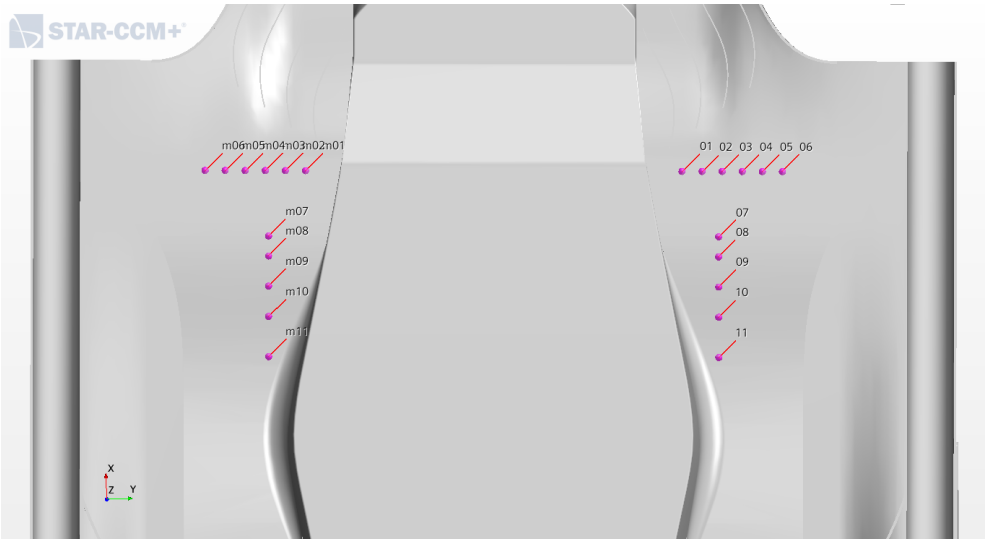

Figure 3.13: Pressure tapping placement on the undertray in CFD

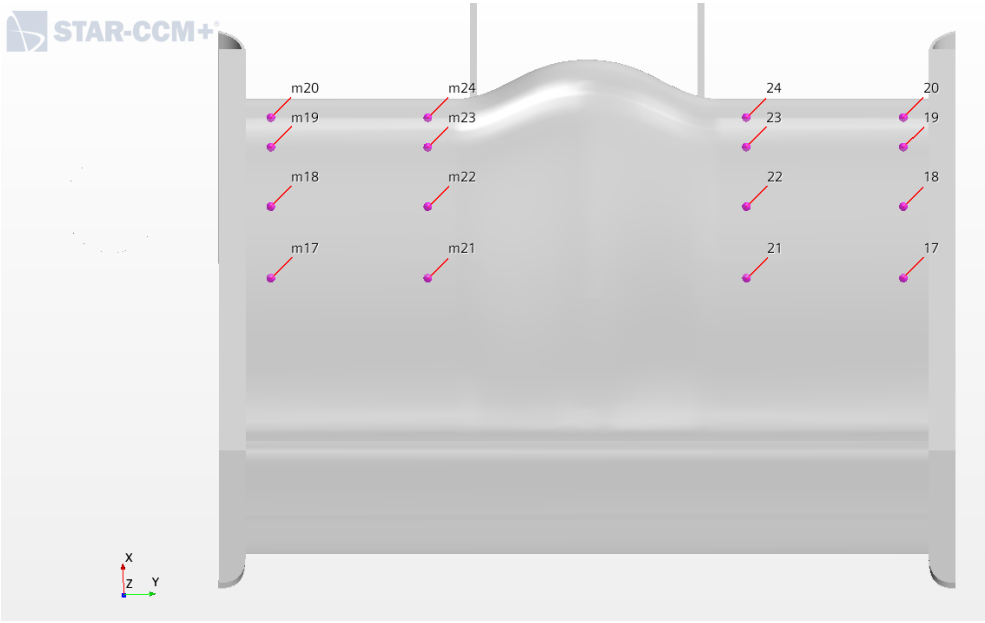

Figure 3.14: Pressure tapping placement on the rear wing in CFD

3.3 CFD simulations

3.3.1 Geometry preparation and meshing

The geometry for all parts of the CFD model is created in Solidworks and imported into STAR-CCM+ as a Parasolid. The surface wrapper with contact prevention is used to create a closed, non-intersecting surface due to the large number of in-

Table 3.4: Pressure tapping overview for front wing (FW), undertray (UT) and rear wing (RW)

Assembly	Taps experiments	Taps CFD
FW	33-36 m37-m40	33-40 m33-m40
UT	01-11	01-11 m01-m11
RW	17-20 m21-m24	17-24 m17-m24

tersecting parts. The imported geometry in STAR-CCM+ is shown in figure 3.15, while the model and setup in the wind tunnel is shown in figure 3.16 for comparison.

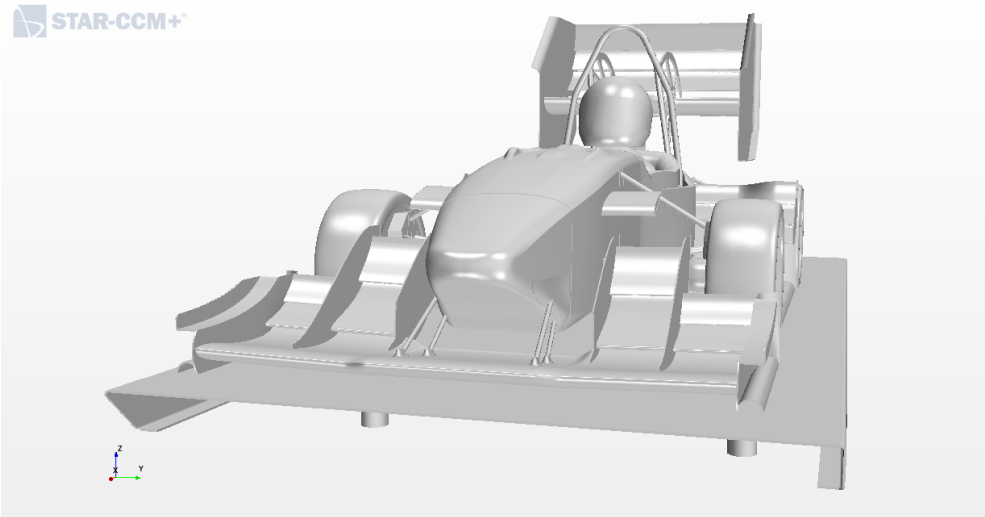

Figure 3.15: CFD model with wind tunnel setup

The walls and roof of the domain tunnel are defined as symmetry planes to enforce parallel flow at these surfaces. The inlet and outlet are defined as a velocity inlet and pressure outlet respectively. The inlet velocity is set to a constant value depending on the case being studied, while the pressure is set to zero at the outlet for all cases.

The geometry is meshed using the Trimmed Cell Mesher together with the Prism Layer Mesher. Orthogonal prismatic cells are added next to wall surfaces to improve the accuracy of the solution near walls. Mesh refinement regions are added in areas where a finer mesh is required due to higher gradients or areas of more interest, in this case the ground effect, front and rear wings, among others. The volume mesh around the whole car is shown in figure 3.17, while figures 3.18 and 3.19 show the volume mesh around the rear wing elements, front wing main

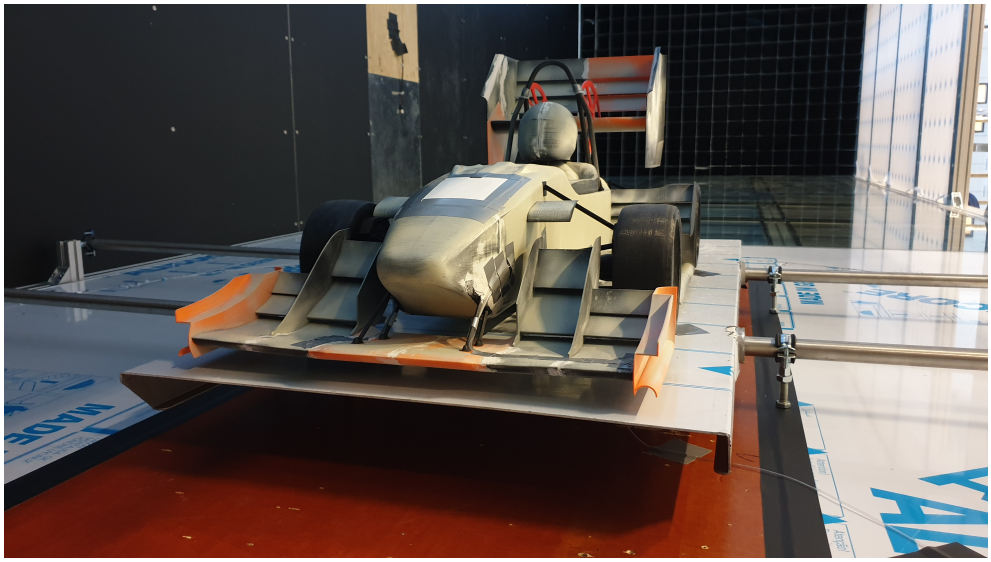

Figure 3.16: Wind tunnel model. Photo: Adrian Leirvik Larsen

element, nose and ground effect plate respectively. The structured volume mesh together with the prism layer mesh on all surfaces can clearly be seen in these figures. The surface mesh of the front of the model is shown in figure 3.20.

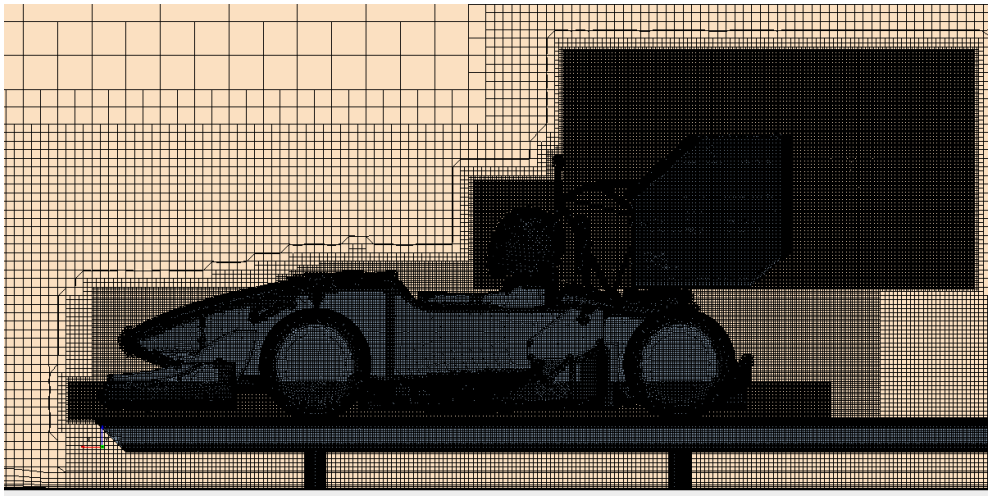

Figure 3.17: Volume mesh full car

Since the geometry has been scaled to $1/3rd$ of the original size of the vehicle, the mesh has also been scaled accordingly. The wall y+ values on the surface of the vehicle are shown in figure 3.21.

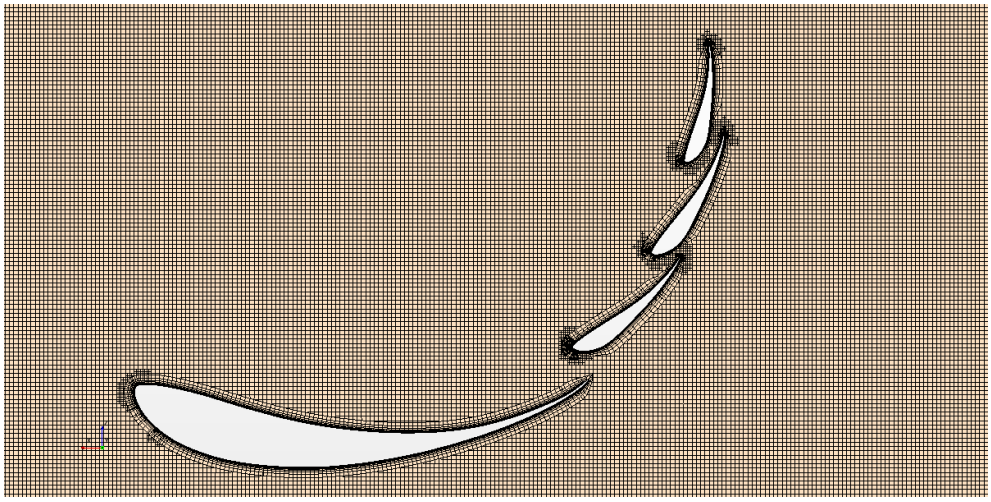

Figure 3.18: Volume mesh rear wing

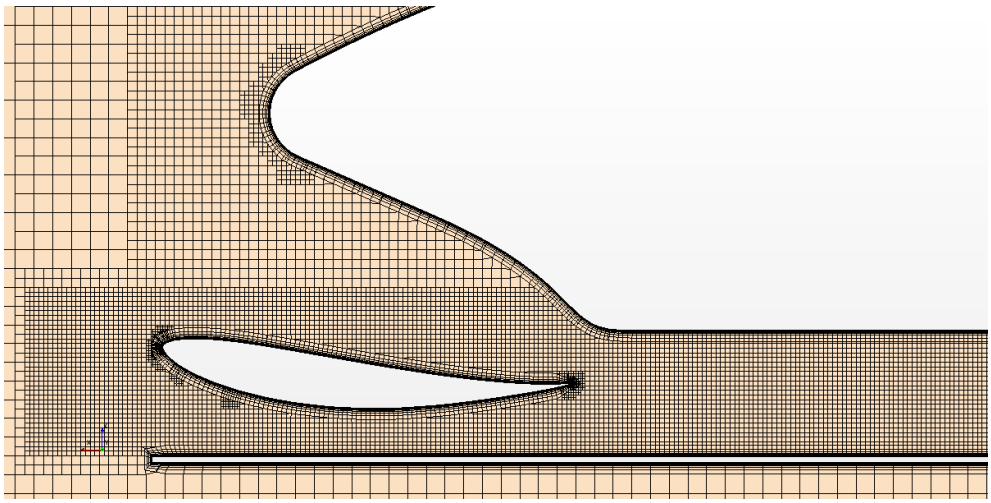

Figure 3.19: Volume mesh front wing, nose and ground effect plate

3.3.2 Turbulence modelling

For the iterative design process of the Revolve NTNU electric vehicles, the steady Realizable k-ϵ Two-layer turbulence model has been utilized, as it offers a fair trade-off between accuracy and computational time. This is based on the work of Sagmo from 2016 [22], both for the turbulence modelling and meshing techniques. The Two-Layer All-y+ Wall Treatment is selected, which uses the standard "law of the wall", together with the segregated flow solver, as no high Mach numbers, shock waves or compressibility effects are expected.

These are the models used for the simulations for all states of freestream velocity V_∞ and yaw angles ψ. Due to time constraints during the design process of the aerodynamic wing package, the computational time is the most important

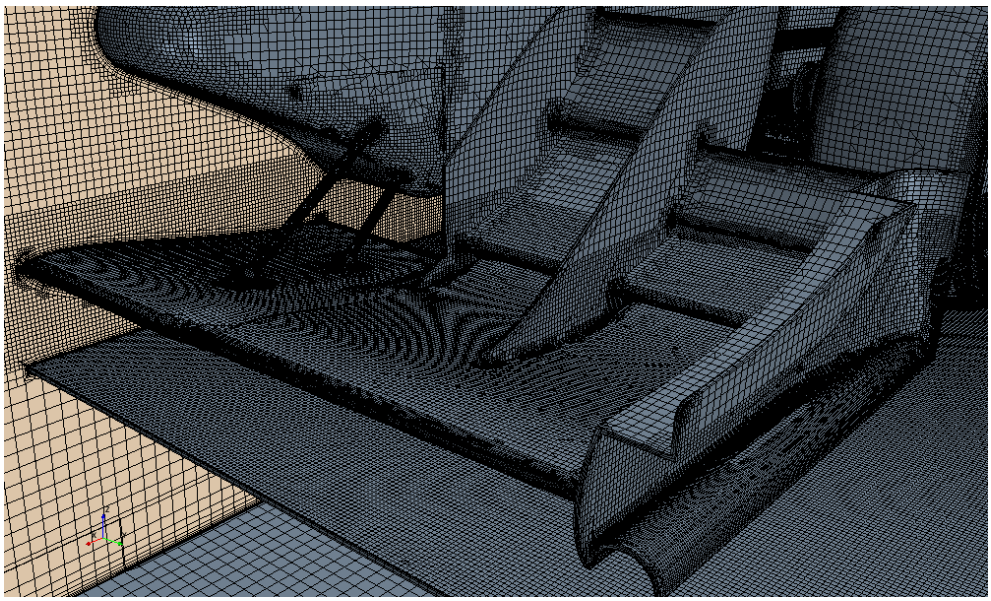

Figure 3.20: Surface mesh front wing, nose and ground effect plate

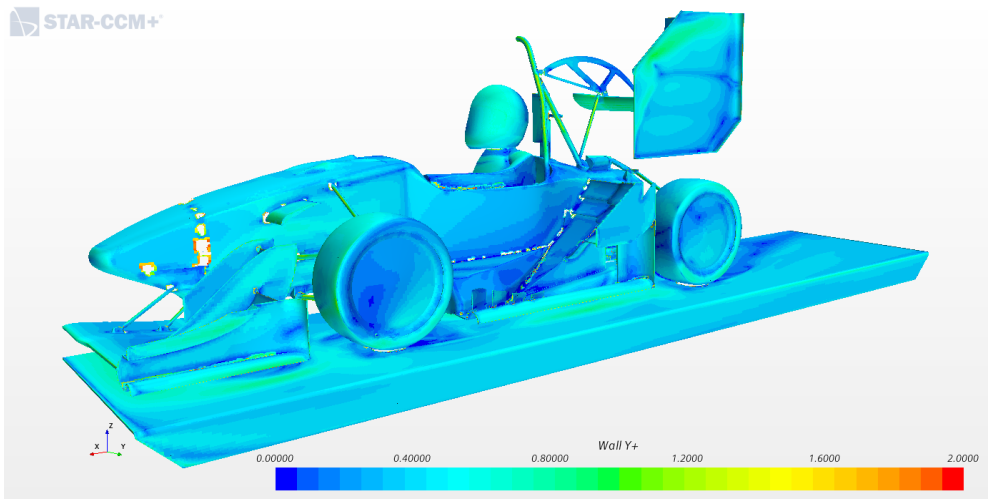

Figure 3.21: Wall y+ distribution across the vehicle surface

parameter to take into consideration. Additionally, there is no need to accurately solve all parts of the turbulent flow structures, as only the performance of the system as a whole are of interest. Therefore this model has been used for several years, and is the reason it is being used in this project for a thorough comparison to the experimental results.

For comparison between CFD and experiments the steady and unsteady k-ω SST turbulence model, in addition to the unsteady k-ϵ model, will be used for a single case, $V_\infty = 60km/h = 16.67m/s$ and $\psi = 0deg$. For the unsteady cases

the implicit scheme with a time-step of 0.01s, 50 inner iterations and a 2s time period is used.

The force and force coefficient reports in STAR-CCM+ are used for the lift and drag. A probe scalar for each pressure tap location is used to measure the static pressure at the front and rear wings and undertray of the vehicle. The pressure tapping locations for the full car are shown in figure 3.11 for a $\psi = 2deg$ case, while a more detailed overview of the front wing, undertray and rear wing is shown in figures 3.12, 3.13 and 3.14 respectively, and summarized in table 3.4.

Chapter 4

Results

4.1 Grid dependency steady RANS k-ϵ

A simple grid dependency study for the steady RANS k-ϵ turbulence model was performed using three different grids. The results for the lift and drag forces and coefficients, rear downforce (DF) percentage and CPU time are shown in table 4.1. The velocity used is $V_\infty = 60km/h = 16.67m/s$.

Table 4.1: Grid dependency for lift and drag for half-car

Grid	No. of cells	L[N]	D[N]	C_L[-]	C_D[-]	Rear DF[%]	CPU time[s]
n1	3.75*10^7	75.41	33.17	3.484	1.532	52.6	1.64*10^6
n2	1.57*10^7	74.29	32.10	3.432	1.483	51.4	6.87*10^5
n3	7.99*10^6	72.66	31.07	3.357	1.435	48.9	3.40*10^5

As the results for the lift and drag are changing when the grid size is changed, the finest grid size, n1, is used for all cases.

4.2 Force measurements

4.2.1 Steady RANS k-ϵ vs experiments

Figure 4.1 shows the drag measurements for all freestream velocities ($V_\infty = 20km/h = 5.56m/s$ to $V_\infty = 50km/h = 13.89m/s$) and yaw angles ($\psi = -5deg$ to $\psi = 5deg$) for both the experimental ("e") and simulated ("s") cases. The drag is defined as being positive in x-direction opposite to the heading direction of the vehicle.

Figure 4.2 shows the lift measurements for all freestream velocities ($V_\infty = 20km/h = 5.56m/s$ to $V_\infty = 50km/h = 13.89m/s$) and yaw angles ($\psi = -5deg$ to $\psi = 5deg$) for both the experimental and simulated cases. The lift has been defined as positive downwards in z-direction, meaning "lift" in this case is equivalent to "downforce" or "negative lift".

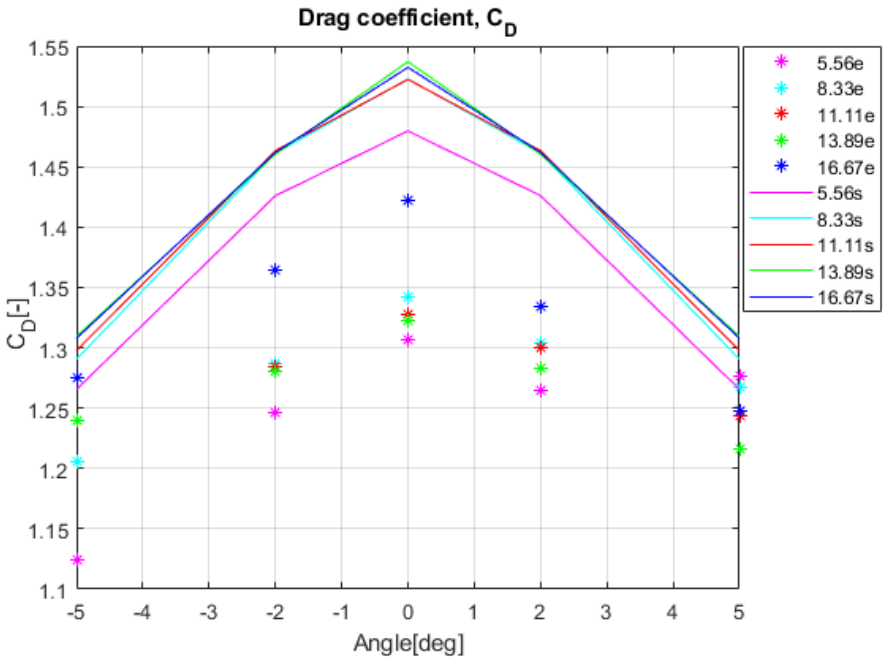

Figure 4.1: Drag coefficients for all freestream velocities V_∞ in m/s and yaw angles ψ in deg

For most of the lift force results from the experiments it can clearly be seen in figure 4.2 that the measurements are way off the values expected and found in the CFD simulations. These are due to a possible fault with some of the load cells, and will thus not be discussed in great detail and will be omitted from the conclusion. Because of this the center of pressure location or the rear downforce percentage for the experimental cases will not be considered. Figure 4.3 shows only the CFD data for the lift coefficients for comparison between the different velocities and yaw angles.

The lowest freestream velocity presented is $V_\infty = 20km/h = 5.56m/s$, but runs were also performed at $V_\infty = 10km/h = 2.78m/s$. Due to the uncertainties and risk of disturbances at such low velocities these results are omitted.

All standard deviations for the results for the voltage measurements are given in appendix C.

4.2.2 Comparison of turbulence models and experiments

In table 4.2 the lift and drag forces and coefficients for the k-ϵ and k-ω SST (steady and unsteady) are presented. Once again the experimental results for lift force and coefficient are clearly wrong and will not be extensively discussed.

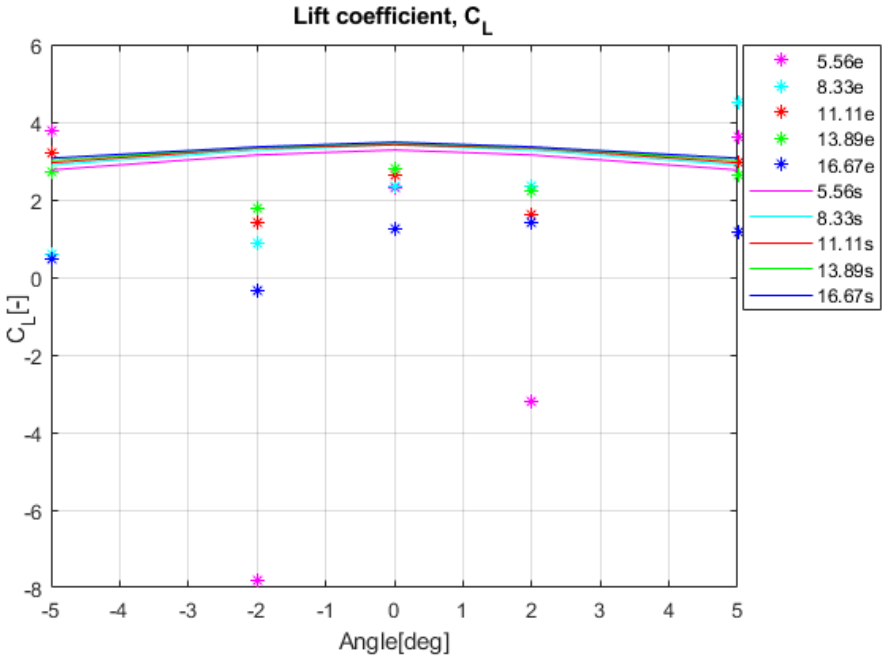

Figure 4.2: Lift coefficients for all freestream velocities V_∞ in m/s and yaw angles ψ in deg

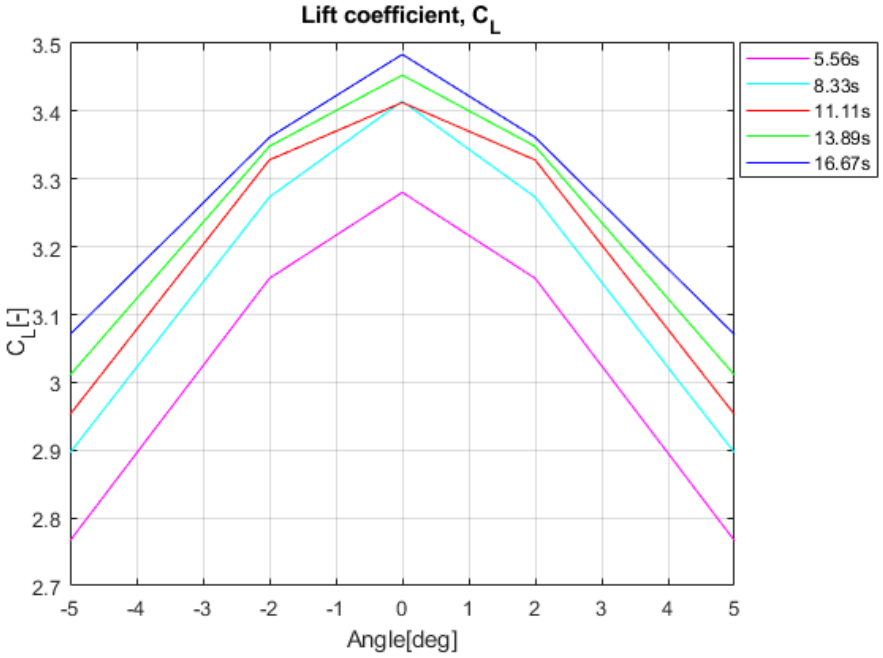

Figure 4.3: Lift coefficients for all freestream velocities V_∞ in m/s and yaw angles ψ in deg from CFD

Table 4.2: Lift and drag forces and coefficients for turbulence models and experiments for the $V_\infty = 60km/h = 16.67m/s$, $\psi = 0deg$ case

	Steady k-ϵ	Unsteady k-ϵ	Steady k-ω	Unsteady k-ω	Experiments
$C_L[-]$	3.484	3.422	3.398	3.150	1.238*
$C_D[-]$	1.532	1.439	1.444	1.380	1.422
$L[N]$	75.41	74.07	73.54	68.17	27.33*
$D[N]$	33.17	31.14	31.24	29.88	31.40
Rear DF [%]	52.6	49.8	53.7	53.3	-
CPU time $[s]$	1.64*10^6	4.99*10^6	2.42*10^6	5.09*10^6	n/a

4.3 Pressure measurements

4.3.1 Steady RANS k-ϵ vs experiments

As explained in section 3.2.3 symmetry was assumed about the xz plane, meaning that only half of the pressure taps presented in figures 3.12 to 3.14 were included on the wind tunnel model. The taps numbering in the results will thus be equivalent to the locations of the taps 01-11, 17-24 and 33-40 for negative yaw angles ψ, and equivalent to m01-m11, m17-m24 and m33-m40 for positive yaw angles ψ.

All standard deviations for the results for the pressure measurements are given in appendix C.

Front wing

The pressure distributions for a plane in the xz-plane at the same y-location as each row of pressure taps are shown in figures 4.4 and 4.5, while figure 4.6 shows the surface pressure on the front wing suction side together with the pressure tap locations, all for $V_\infty = 60km/h = 16.67m/s$. The coordinates of each tap are equivalent for both the experimental and simulation results. Figures B.1 to B.8 in appendix B show the static pressure measurements for the front wing suction side for all freestream velocities ($V_\infty = 20km/h = 5.56m/s$ to $V_\infty = 50km/h = 13.89m/s$) and yaw angles ($\psi = -5deg$ to $\psi = 5deg$) for both the experimental and simulated cases. The pressure data is presented using the coefficient of pressure C_p relative to the freestream pressure reference, while the yaw angle ψ is given in degrees relative to straight line driving. The abbreviation "FW" is used for "front wing" in all figures.

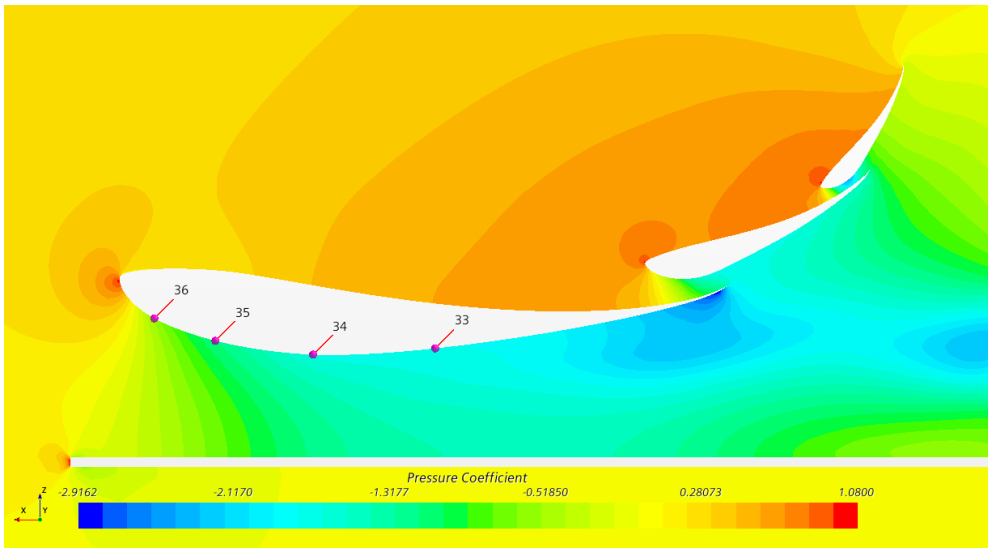

Figure 4.4: Pressure distribution for front wing $y = 0.213m$ with pressure taps coordinates at $V_\infty = 60km/h = 16.67m/s$ and $\psi = 0deg$

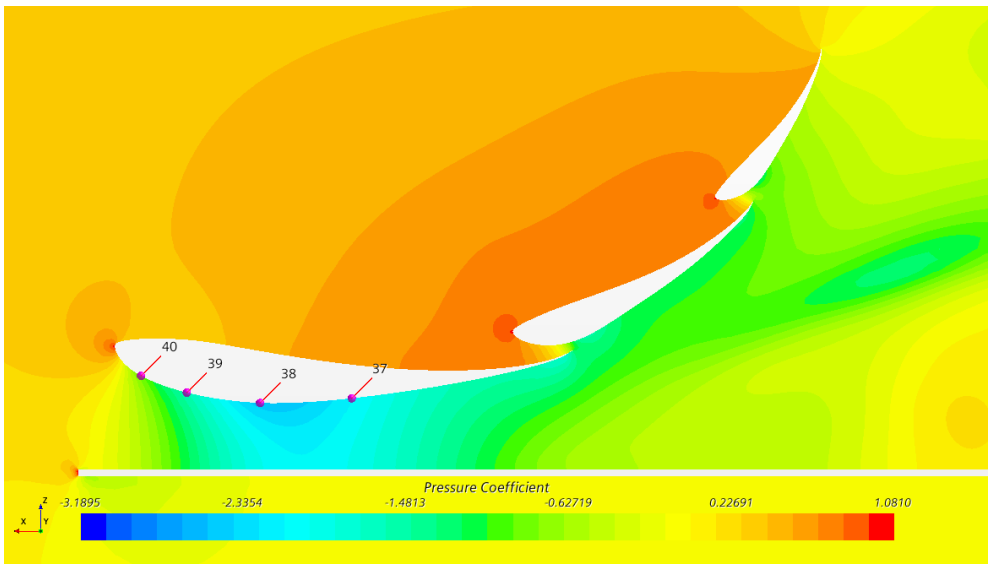

Figure 4.5: Pressure distribution for front wing $y = 0.100m$ with pressure taps coordinates at $V_\infty = 60km/h = 16.67m/s$ and $\psi = 0deg$

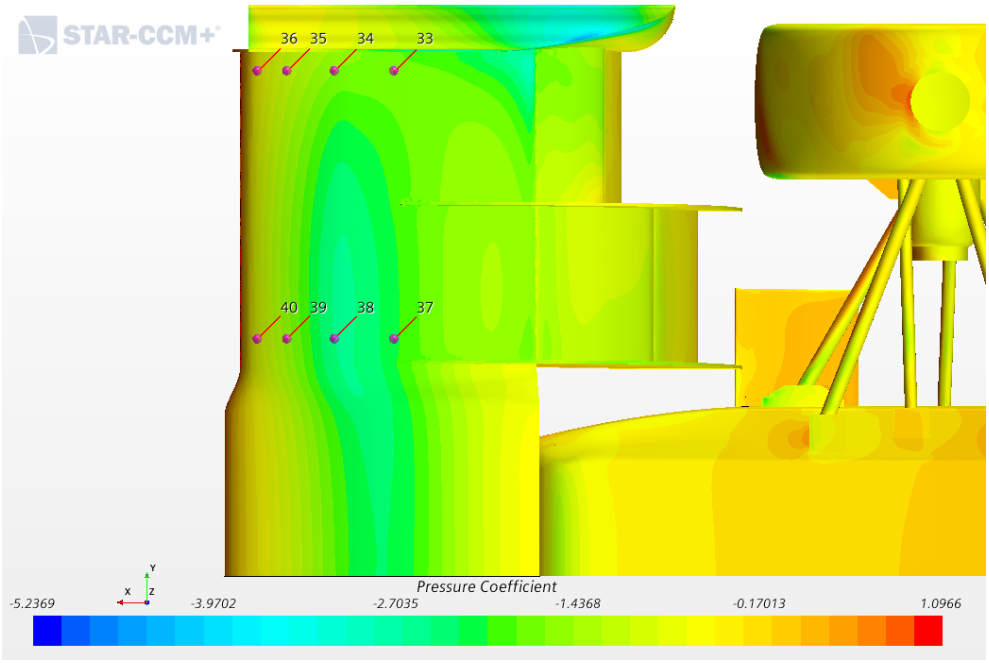

Figure 4.6: Pressure distribution for front wing suction side surface with pressure taps coordinates at $V_\infty = 60km/h = 16.67m/s$ and $\psi = 0deg$

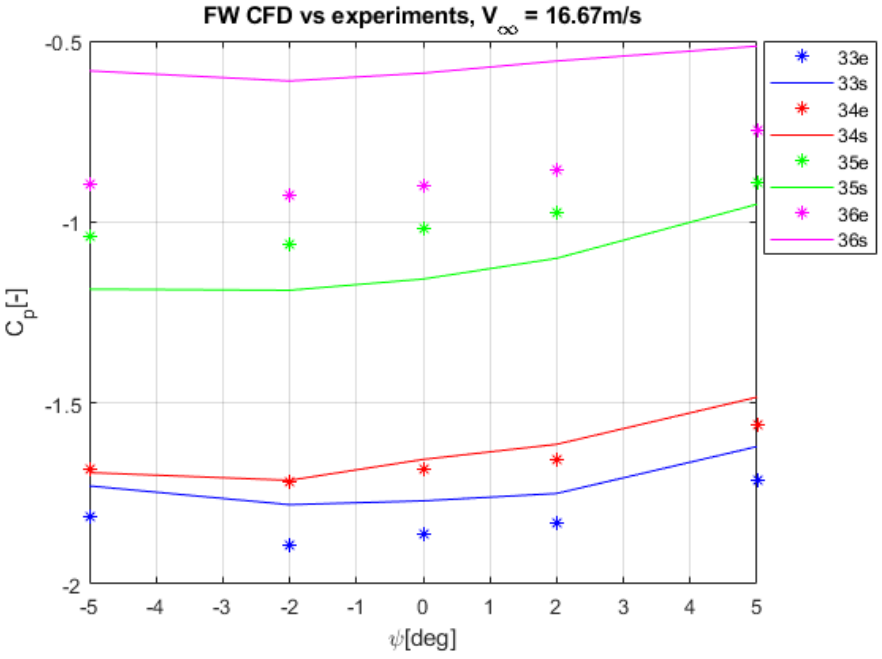

Figure 4.7: Static pressure measurements for front wing taps 33-36 at $V_\infty = 60km/h = 16.67m/s$

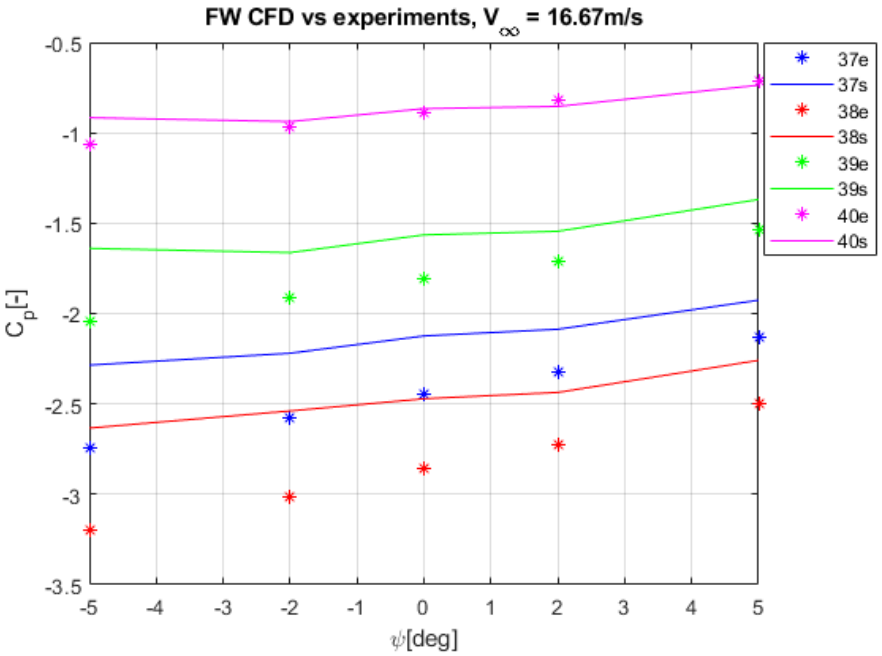

Figure 4.8: Static pressure measurements for front wing taps 37-40 at $V_\infty = 60km/h = 16.67m/s$

Undertray

The pressure distributions for a plane in the yz-plane and xz-plane at the same x- and y- location as each row of pressure taps are shown in figures 4.9 and 4.10 respectively, while figure 4.11 shows the surface pressure on the undertray together with the pressure tap locations, all for $V_\infty = 60km/h = 16.67m/s$. The coordinates of each tap are equivalent for both the experimental and simulation results. Figures B.9 to B.16 in appendix B show the static pressure measurements for the undertray for all freestream velocities ($V_\infty = 20km/h = 5.56m/s$ to $V_\infty = 50km/h = 13.89m/s$) and yaw angles ($\psi = -5deg$ to $\psi = 5deg$) for both the experimental and simulated cases. The pressure data is presented using the coefficient of pressure C_p relative to the freestream pressure reference, while the yaw angle ψ is given in degrees relative to straight line driving. The abbreviation "UT" is used for "undertray" in all figures.

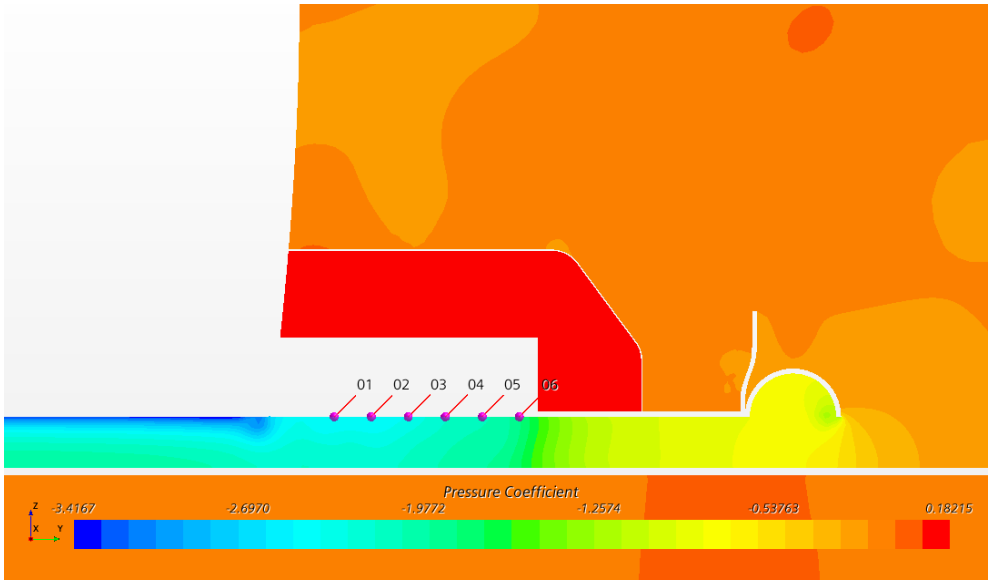

Figure 4.9: Pressure distribution for undertray $x = 0.093m$ with pressure taps coordinates at $V_\infty = 60km/h = 16.67m/s$ and $\psi = 0deg$

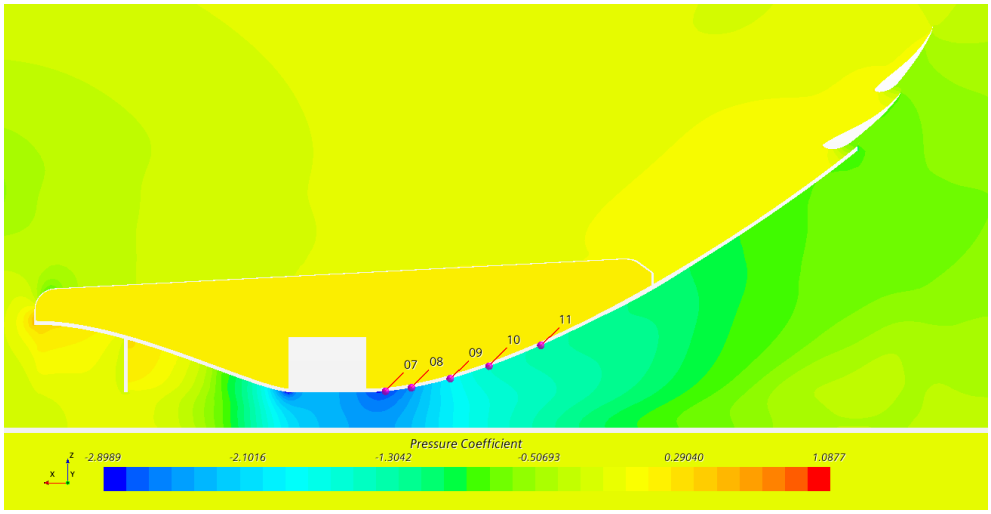

Figure 4.10: Pressure distribution for undertray $y = 0.112m$ with pressure taps coordinates at $V_\infty = 60km/h = 16.67m/s$ and $\psi = 0deg$

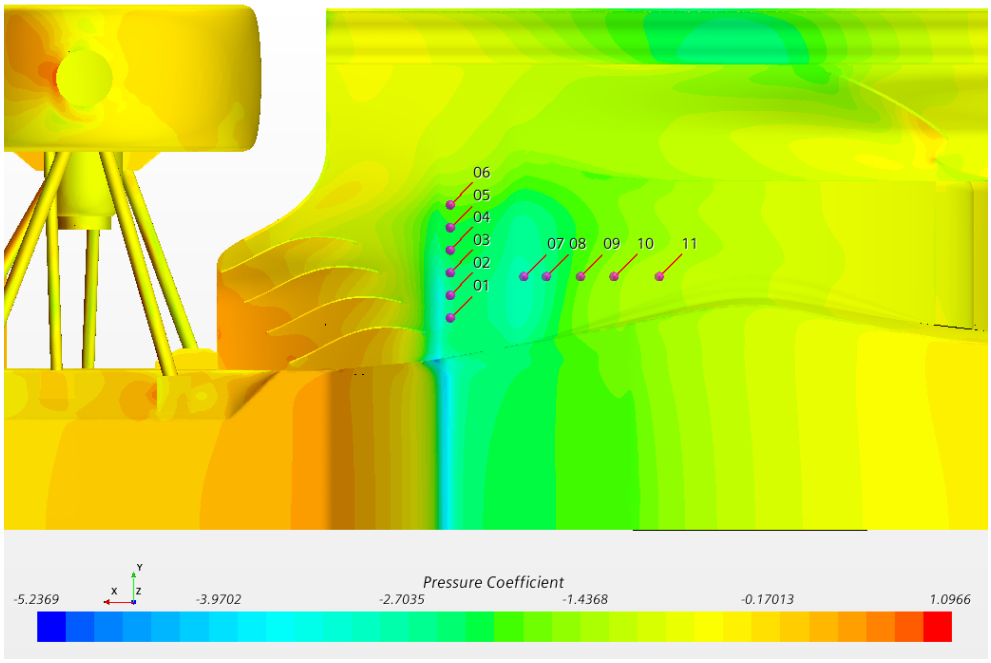

Figure 4.11: Pressure distribution for undertray surface with pressure taps coordinates at $V_\infty = 60km/h = 16.67m/s$ and $\psi = 0deg$

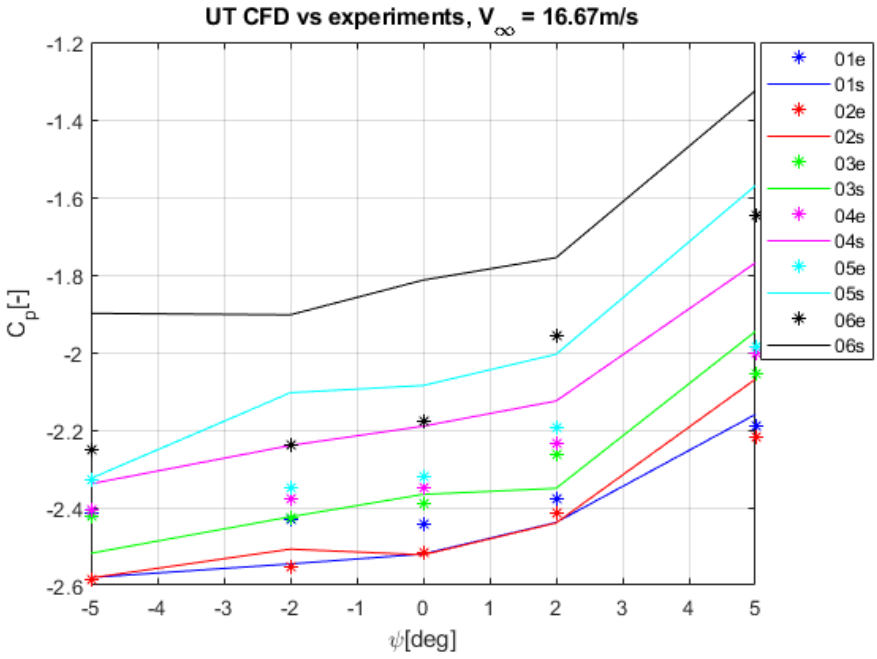

Figure 4.12: Static pressure measurements for undertray taps 01-06 at $V_\infty = 60km/h = 16.67m/s$

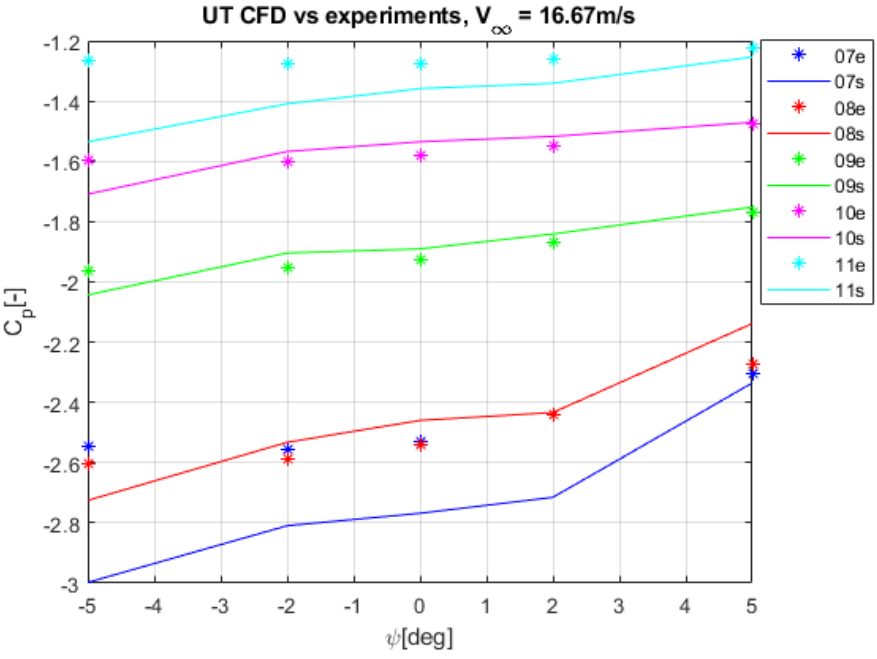

Figure 4.13: Static pressure measurements for undertray taps 07-11 at $V_\infty = 60km/h = 16.67m/s$

Rear wing

The pressure distributions for a plane in the xz-plane at the same y-location as each row of pressure taps are shown in figures 4.14 and 4.15, while figure 4.16 shows the surface pressure on the rear wing suction side together with the pressure tap locations, all for $V_\infty = 60km/h = 16.67m/s$. The coordinates of each tap are equivalent for both the experimental and simulation results. Figures B.17 to B.24 in appendix B show the static pressure measurements for the rear wing suction side for all freestream velocities ($V_\infty = 20km/h = 5.56m/s$ to $V_\infty = 50km/h = 13.89m/s$) and yaw angles ($\psi = -5deg$ to $\psi = 5deg$) for both the experimental and simulated cases. The pressure data is presented using the coefficient of pressure C_p relative to the freestream pressure reference, while the yaw angle ψ is given in degrees relative to straight line driving. The abbreviation "RW" is used for "rear wing" in all figures.

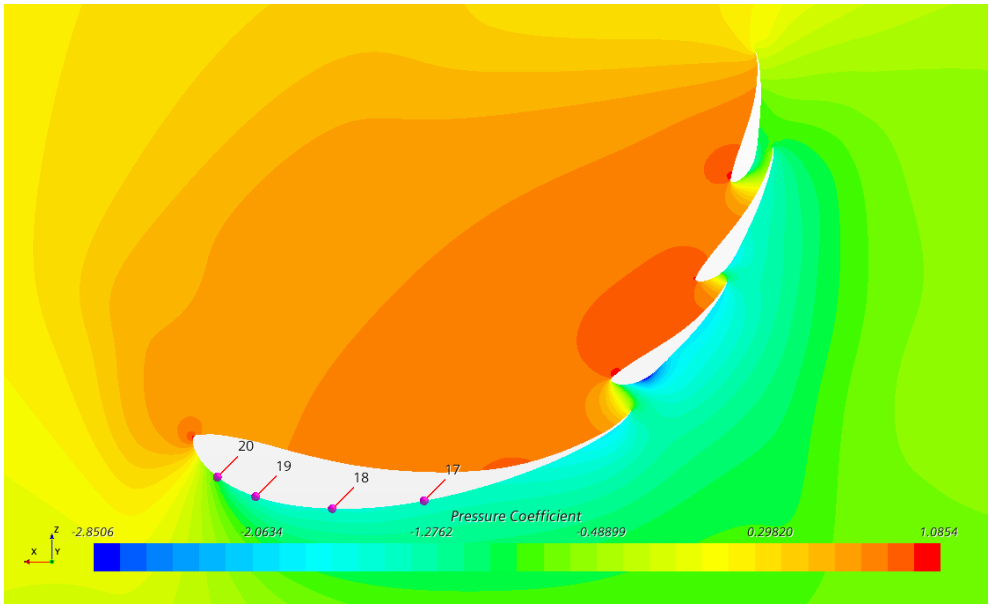

Figure 4.14: Pressure distribution for rear wing $y = 0.133m$ with pressure taps coordinates at $V_\infty = 60km/h = 16.67m/s$ and $\psi = 0deg$

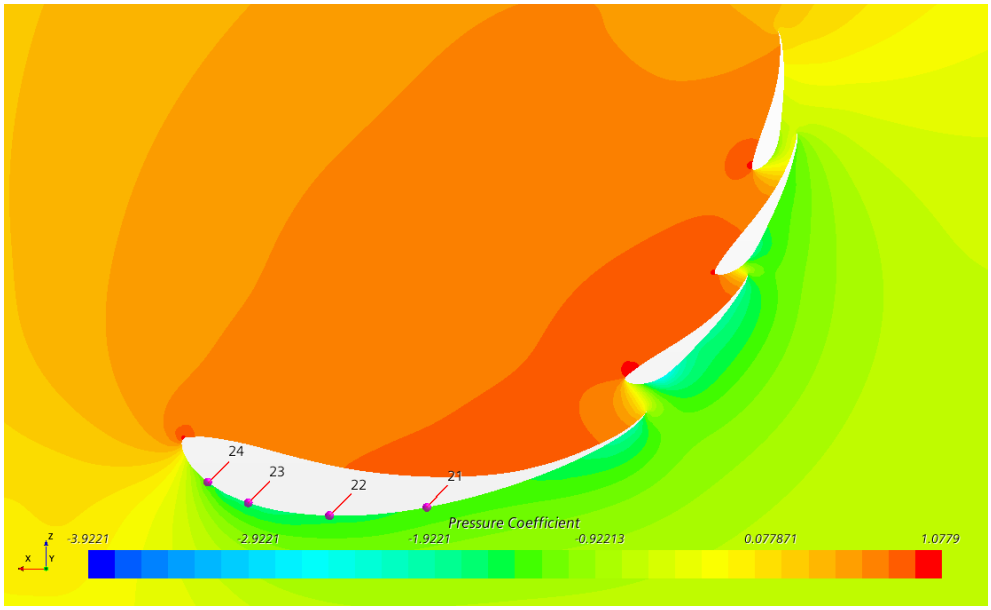

Figure 4.15: Pressure distribution for rear wing $y = 0.067m$ with pressure taps coordinates at $V_\infty = 60km/h = 16.67m/s$ and $\psi = 0deg$

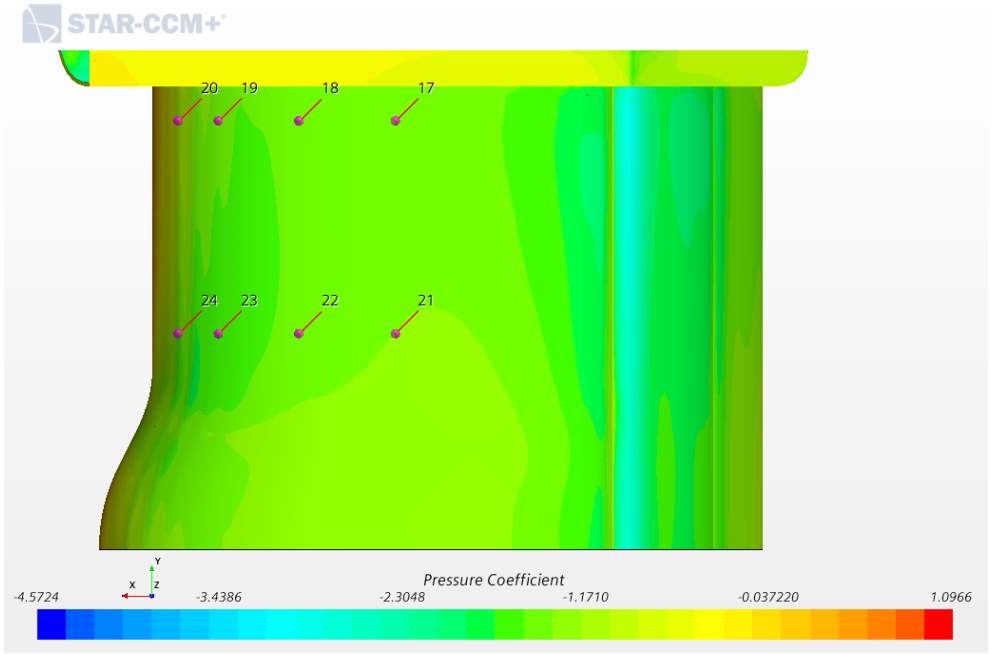

Figure 4.16: Pressure distribution for rear wing suction side surface with pressure taps coordinates at $V_\infty = 60km/h = 16.67m/s$ and $\psi = 0deg$

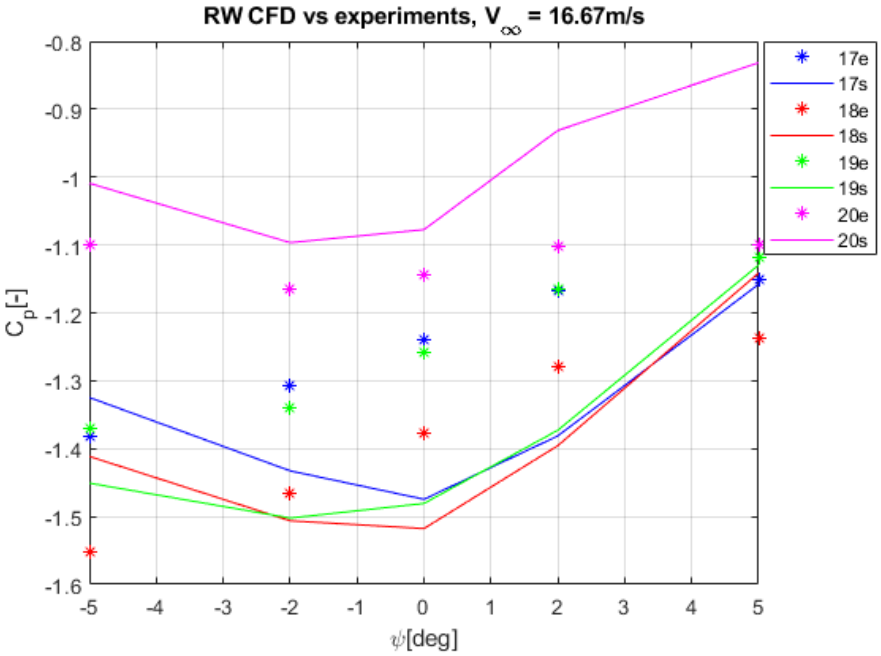

Figure 4.17: Static pressure measurements for rear wing taps 17-20 at $V_\infty = 60km/h = 16.67m/s$

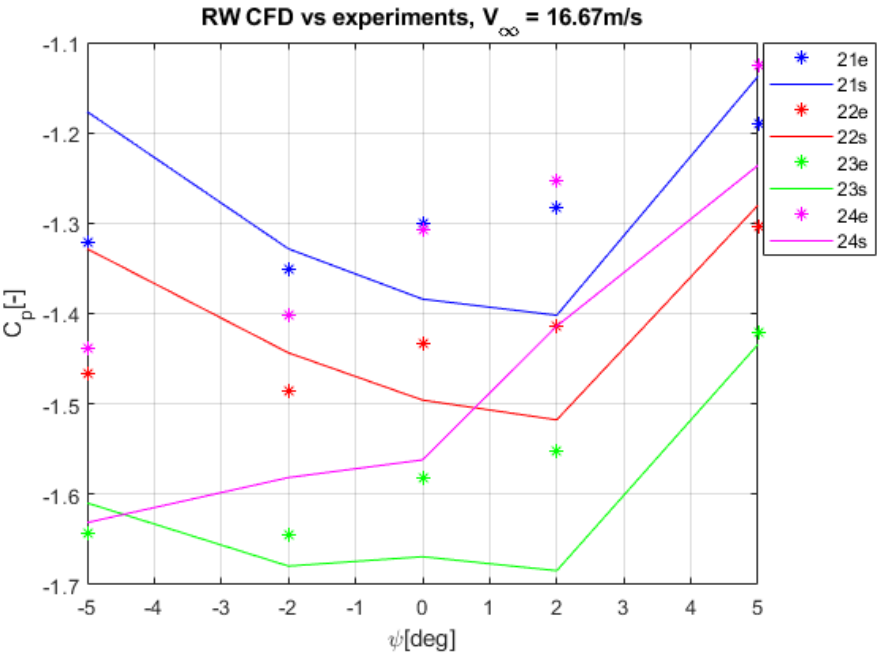

Figure 4.18: Static pressure measurements for rear wing taps 21-24 at $V_\infty = 60km/h = 16.67m/s$

4.3.2 Comparison of turbulence models to experiments

In figures 4.19 to 4.21 the pressure tapping results at the front and rear wing suction sides, and undertray for the k-ϵ and k-ω SST (steady and unsteady) turbulence models and experimental case are presented. All are run at $V_\infty = 60km/h = 16.67m/s$ and $\psi = 0deg$, and the pressure coefficient is plotted against each pressure tap on the front wing, undertray and rear wing.

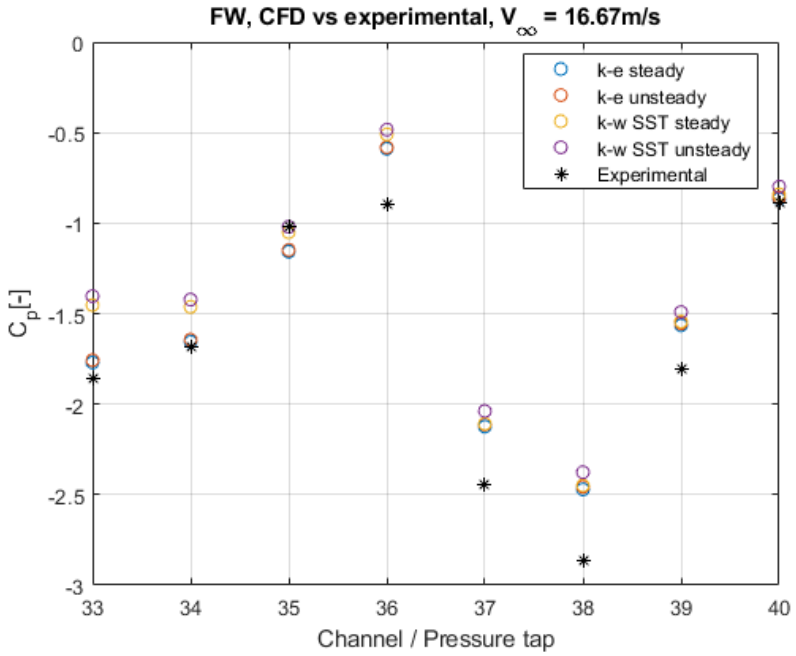

Figure 4.19: Comparison of turbulence models and experimental results for front wing taps 33-40 at $V_\infty = 60km/h = 16.67m/s$ and $\psi = 0deg$

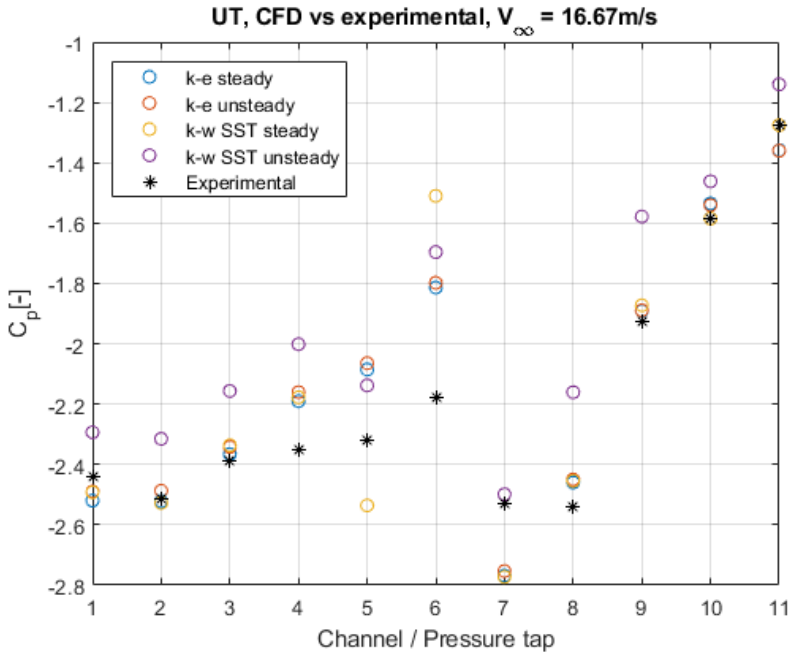

Figure 4.20: Comparison of turbulence models and experimental results for undertray taps 01-11 at $V_\infty = 60km/h = 16.67m/s$ and $\psi = 0deg$

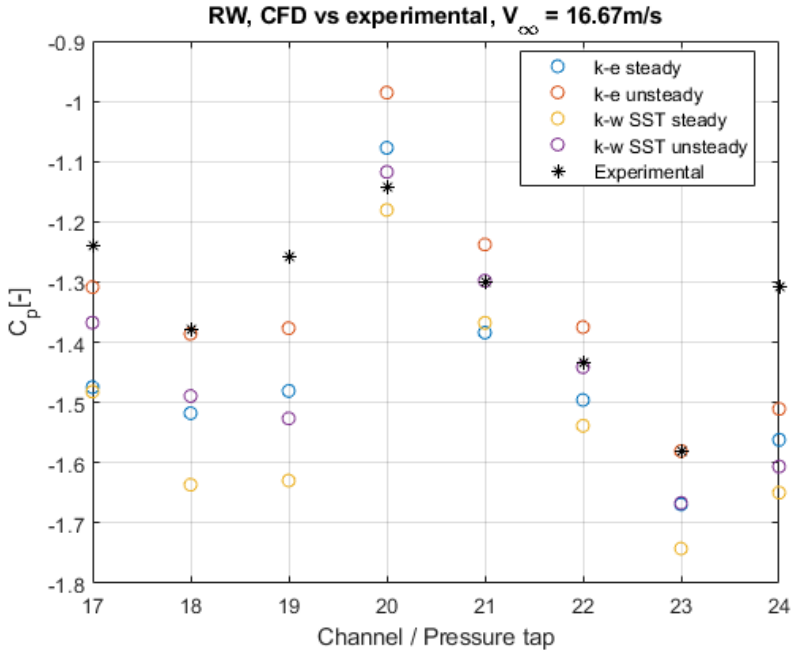

Figure 4.21: Comparison of turbulence models and experimental results for rear wing taps 17-24 at $V_\infty = 60km/h = 16.67m/s$ and $\psi = 0deg$

Chapter 5

Discussion

A brief discussion of the experiments will first be presented, regarding the model preparation, experimental setup in the wind tunnel and relevance in terms of the correlation and application to the full-size vehicle. The main part of this project concerns the steady RANS k-ϵ turbulence model, equivalent to that used in the iterative design process of the aerodynamics of the electric vehicles. This means that the correlation between this model and the experimental data will be discussed for all velocities and yaw angles, for both the force and pressure data. Then the results for the comparison between different steady and unsteady turbulence models for $V_\infty = 60km/h = 16.67m/s$, $\psi = 0$ and experimental data will be discussed.

5.1 Experimental setup

The wind tunnel model itself, shown in figure 3.2, was 3D printed using both PLA and Tough PLA filaments. During the wind tunnel experiments no parts of the model had any failures, deformations or strong vibrations, meaning that for these kind of velocities 3D printing in PLA using FFF works very well. The preparation of the model surfaces gave all parts a smooth enough finish and a geometry matching the CAD models, with a few exceptions. Some of the trailing edges of the airfoils had some deviations from the CAD model due to the thin geometry. That meant some additional work had to be done to get a satisfactory finish in these areas. For further application of this manufacturing technique a solution may be to round off the training edges slightly to improve the quality, given that the same adjustments are done in the CAD models used for the CFD simulations.

The main area of improvement for the wind model design is the tolerances for the brackets and attachment points. Carefully examining of the printing technique and material specifications will help setting the correct dimensions for all fastening points and brackets. A large amount of the model preparation for this project was simply to sand all brackets to make them fit. While it didn't affect the quality of the model and experiments, it was a tedious task which may easily be

avoided with a bit more knowledge and considerations around the manufacturing process.

Due to the fact that the preparations for the experiments took more time than I anticipated, there wasn't time to do as much work on the CFD simulations as I wanted. The results being that some of the results from the simulations are not showing as good convergence as they should have done to be certain of the validity of the results. A more thorough discussion on this topic follows below.

5.2 Steady RANS k-ϵ vs experiments

5.2.1 Force measurements

The results for the overall drag coefficients for the steady k-ϵ turbulence model and experimental data are presented in figure 4.1. It can be seen that the values for the CFD simulations using the steady k-ϵ model are generally overpredicted by up to 10-12% compared to the experimental results. Work by Sagmo [22] and Mildestveit [23] suggested a deviation up to 15% for the steady k-ϵ model. While this results is slightly unexpected, there may be some possible explanations for it. Deviations in the geometry between the wind tunnel model and CAD model may affect the drag. Another reason may be that the CFD simulations are predicting an earlier separation on certain elements than what the case is for the experiments.

For the drag coefficients it can be seen that the measurements for $V_\infty = 20km/h = 5.56m/s$ behaves slightly differently for the experimental cases when changing the yaw angle ψ. This is most likely due to some small measurement disturbances or errors. When measuring at such low velocities very small disturbances will have major impacts on the results, meaning that the deviations seen in this case is considered measurement errors.

Looking at the residuals, downforce (negative lift) and drag convergence plots for the $V_\infty = 60km/h = 16.67m/s$, $\psi = 0deg$ case in figures A.1, A.2 and A.3 in appendix A it is apparent that some more work should be done to arrive at a better convergence. While the downforce and drag numbers appears to have converged the residuals are still a bit high, meaning that this may contribute to the slight deviation between simulation and experimental results. Some more care should be taken during the meshing procedure, choice of the number of iterations and the stopping criteria.

As stated earlier the values for the experimental lift coefficients will not be discussed extensively due to major faults in the measurements. They are still presented in figures 4.2 and 4.3. It is worth noting however that if the experimental results had shown a lower downforce (less negative lift) than the simulations, it would have contributed to explaining the deviations in drag results, as a reduction in lift would have resulted in a reduction in lift-induced drag. Functioning lift measurements would also have provided information about the center of pressure, and thus the aerodynamic performance elaborated in section 2.1.2 could have been discussed.

5.2.2 Pressure measurements

Front wing

The front wing pressure distributions are presented in figures 4.4, 4.5 and 4.6 for $V_\infty = 60km/h = 16.67m/s$. The probe scalars in the pressure distribution figures corresponds to the data points for the pressure tap measurements at $\psi = 0deg$ in figures 4.7 and 4.8. It can be seen that the pressure coefficient readings for the experimental case is slightly lower (i.e. more negative) than the simulated values. That means the simulations predict a too high pressure for the $V_\infty = 60km/h = 16.67m/s$ case. The exception is the pressure tap number 35, where the simulation gives a lower pressure than the experimental data. This may be due to the fact that this point is in an area with a high pressure gradient and close to the front wing endplate, as well as the fact that some irregularities on the wind tunnel model surfaces may be present. Thus these areas are hard to predict correctly.

Looking at the plots of the front wing for all velocities V_∞ and yaw angles ψ, figures B.1 to B.8, it can be seen that the pressure measurements closest to the front wing endplate ($y = 0.213m$, taps 33-36) for the front wing from the simulations are slightly overpredicted (i.e. more negative) compared to the experimental data, while the opposite is general the case for the measurements closer to the middle of the front wing ($y = 0.100m$, taps 37-40). The most notable exception being the tap closest to the leading edge and endplate (tap 36), as the deviation is considerably larger here.

In general the correlation for the pressure measurements for the front wing suction side is rather good. The behaviour moving between different velocities and yaw angles is equal for the experimental and simulated cases, and the deviations are within 10-15%, with a few exceptions. Both predict an increase in pressure when moving from $\psi = -5deg$ to $\psi = 5deg$. For the measurements and simulation numbers at the lowest freestream velocities the results deviate more, but as for all cases the results are more exposed to larger relative deviations due to the lower values measured and the effect only small deviations or disturbances will have on the results.

Undertray

The pressure distributions presented in figures 4.9, 4.10 and 4.11 are for the $V_\infty = 60km/h = 16.67m/s$, $\psi = 0deg$ case, and the probe scalars corresponds to the data points for the pressure tap measurements shown in figures 4.12 and 4.13. For taps 01-06 the simulation data seems to correlate better with the experimental results for the innermost taps, where the lowest pressure occurs. For the outermost measurements the simulations give too high pressure readings compared to the experiments. Looking at the taps 07-11 the simulations and experimental data seem to correlate nicely, except for an overpredicted negative pressure value for the simulations at tap 07.

The same trend as described above may be seen for most of the velocities

and yaw angle plot for the undertray, given in figures B.9 to B.16 in appendix B. The correlation between the simulations and experimental data is rather good for the higher velocity cases. When the velocity is lower the behaviour when moving between different yaw angles deviates more between the simulations and experiments, especially at $\psi = -5deg$ and $\psi = 5deg$. Due to the complex geometry of a Formula race car it is often hard to predict the performance for low velocities, especially in yaw.

Rear wing

Figures 4.14, 4.15 and 4.16 show the pressure distribution for the $V_\infty = 60km/h = 16.67m/s$, $\psi = 0deg$ case together with the probe scalar locations corresponding to the pressure tapping locations in figures 4.17 and 4.18. Generally the simulations seem to slightly overpredict the negative pressure values for this case compared to the experimental data, except for tap 20 on the leading edge and for the most negative yaw angles.

For the rest of the freestream velocity V_∞ and yaw angles ψ, given in figures B.17 to B.24, there are some deviations for the $\psi = -5deg$ and $\psi = 5deg$ cases. The simulations predicts a higher pressure (i.e. less negative) than the experiments for these yaw angles for most of the velocities.

An important thing to consider when analysing the correlation of the rear wing is that it is the element furthest downstream, meaning that all other geometry on the model, both in CFD and experiments, will directly affect the performance and flow structures around the rear wing. That means that even the smallest disturbances or irregularities upstream of the rear wing will affect it and may be the reason the deviations are larger compared to the other elements discussed earlier. While the deviations of around 10-15% are around the same as for the front wing measurements, the behaviour when changing the yaw angle differ more.

5.2.3 Summary - Steady RANS k-ϵ vs experiments

The simulation results give a slightly higher drag and generally more negative pressure than the experimental results. The CFD model is more ideal than the 3D printed model used in the wind tunnel experiments, so it is expected that the aerodynamic performance will be slightly better for the idealized CFD case. For the drag measurements the opposite was experienced, meaning that the CFD modelling may need some more work.

It is also expected that the deviations between the experimental and simulated results increase when moving downstream of the model, as small disturbances will have an influence on the flow structures downstream of that point. The behaviour when moving between different velocities and yaw angles deviates more for the undertray and rear wing than for the front wing.

As all pressure taps are located at the wall, the deviations may be present due to the known unsatisfactory results of the k-ϵ turbulence model close to the walls, especially in areas of adverse pressure gradients. An example may be the deviation

in the pressure development in figures 4.17 and 4.18, where for changing yaw angles the behaviour differ between the experimental and simulated results.

5.3 Comparison of turbulence models to experiments

5.3.1 Force measurements

Table 4.2 shows the results for the lift and drag values for all turbulence models. As explained earlier no thorough discussion of the lift values will be done. While the drag values show a good correlation for all models (less than 10% deviation from the experimental data), the steady k-ϵ model seem to overpredict the drag force compared to the other turbulence models. At the same time the unsteady k-ω SST model underpredicts the drag.

The residuals and parameter convergence for the unsteady k-ϵ model shown in figures A.4, A.5 and A.6 in appendix A. The residual plot shows a sufficient convergence, which is being confirmed by the convergence of the downforce and drag monitors. That means that using a physical time of 2s and 50 inner iterations is sufficient for this case.

For the k-ω SST model the residuals, lift and drag convergence is shown in figures A.7, A.8 and A.9 for the steady case and in figures A.10, A.11 and A.12 for the unsteady case in appendix A. It can clearly be seen that the convergence is not as good as it should have been. The drag and downforce values have some oscillations, but seem to vary around a constant value. More work on the meshing and convergence will have to be done for these turbulence models to be able to draw more definite conclusions.

5.3.2 Pressure measurements

Figures 4.19, 4.20 and 4.21 show the pressure values for all taps on the wind tunnel and CFD model compared to the steady and unsteady k-ϵ and k-ω SST turbulence models for the $V_\infty = 60km/h = 16.67m/s$, $\psi = 0deg$ case. First looking at the front wing, figure 4.19, it can be seen that all turbulence models have good correlation for most of the pressure measurements. It appears that the k-ω SST model (both steady and unsteady) predicts a too high (less negative) pressure towards the trailing edge next to the endplate (taps 33 and 34). However, while all of the models seem to predict a too high pressure compared to the experimental data, the overall behaviour of the pressure development across the suction side surface seems nicely predicted by all models.

Moving further downstream to the undertray, figure 4.20, there is a general trend that the unsteady k-ω SST model predicts a too high pressure, while there are some deviations around taps 05 and 06 for the steady k-ω SST model. As for the front wing the experimental results gives slightly more negative numbers than the simulated cases.

Looking at the results for the rear wing, figure 4.21, the experimental values tend to be slightly less negative than the results from the simulations, although the results are generally more spread out across all data sets than for the front wing and undertray, making it harder to spot a pattern. As discussed earlier, being the element furthest downstream larger deviations are expected around this element.

As the front wing and undertray are in close proximity to the ground, and thus strongly affected by the ground effect underneath the model, only a small deviation in ride height of the wind tunnel model compared to the CAD model used in the CFD simulations may lead to changes in the measured values. While the model was carefully placed in the test section and the ground clearance was thoroughly measured, it is an aspect to take into consideration when analysing the results.

5.4 Aerodynamic performance

As explained in section 2.1.1 the effect of adding an endplate to the end of a wing will increase the lift close to the wing tip. A loss of lift will still be present closer to the endplate, but this effect is less prominent. While no experiments was performed using the wings of the vehicle without an endplate, it can be seen that even though there is a difference between the pressure measurements close to and far away from the endplate for the experimental data it is not very large. The rear wing is most representative for this effect, as the front wing is also affected by the ground effect, bringing some more factors into consideration. The results for $V_\infty = 60km/h = 16.67m/s$ presented in figures 4.17 and 4.18 show a small difference in the experimental values for the two rows of pressure taps.

Utilizing the ground effect efficiently is a very important design criteria for a Formula race car. The pressure measurements done on the undertray (taps 01-06) are located in the area of smallest ground clearance. While some deviations between the CFD simulations and experiments can be noticed in 4.12, the effect of proximity to the ground can be clearly seen. Work on getting the underside of the vehicle modelled more accurately should be a priority for all designers of ground vehicles, as it is a very efficient way of generating downforce compared to the increase in drag.

When the yaw angle of the vehicle is changed, the lift coefficient for the CFD simulations presented in figure 4.3 shows a 10-15% loss when changing from $\psi = 0deg$ to $\psi = \pm 5deg$. One of the reasons for this is the effect of the wheel wake on the side- and undertrays. This is both hard to model accurately and a major contributor to disturbed flow downstream of the wheel assembly. A change in yaw angle will alter which elements the wheel wake affects the most, thus changing the aerodynamic performance significantly. A very similar trend can also be seen for the drag measurements in figure 4.1 for both the CFD simulations and experiments. Due to this the ability to handle the wheel wake is a very important design criteria in race car design.

Chapter 6

Conclusion

Using additive manufacturing to construct a wind tunnel model works well, and is a method that is improving constantly. Care has to be taken though when designing the model and deciding the manufacturing techniques in order to arrive at the best possible surface finishes and to avoid more preparation work than necessary between the production is finished and the model is completed. By using the material and printer properties this technique is recommended for similar applications. The model may also be constructed so that parts can be replaced to test several different designs.

The measurement setup was well planned and thought through. Placing the pressure scanner (and other potential measurement equipment) inside the model is a very good way of keeping the tubing distances short, while minimizing the amount of cables and tubes needed to go out of the model and test section, thus avoiding unnecessary disturbances. The setup of using the ground effect plate made the experiments more realistic than placing the model on the wind tunnel floor. The stands for the force balance measurements also worked well, despite the errors with the lift data. To make an even more realistic setup a rolling floor and rotating wheels on the model would have had to be installed, but this was considered way too time consuming for this project and will also be difficult to implement in the test section used for these experiments.

The general correlation between the experiments and CFD simulations were good, and within what was expected and accepted. For the $V_\infty = 60km/h = 16.67m/s$ cases the deviations are no more than 15% with a few exceptions. The further downstream of the vehicle model the measurements are taken, the larger the deviations become in some areas, due to these parts being affected by geometry differences upstream. CFD simulations will always be an approximation of the real case, and thus never 100% accurate. Performing comparisons between the simulations and experiments gives a good and important indication of how accurate a certain model is and where in the flow field the largest deviations occur. The experimental results found in this project definitely helps to understand how the vehicle behaves in different states compared to CFD results, and will be of large value for future Revolve NTNU teams to increase the knowledge and

understanding of CFD and race car aerodynamics.

While a good comparison between CFD and experiments was performed, more work should be put into the CFD modelling to arrive at better convergence for the parameters of interest. The residuals and parameter convergence were not sufficient for some of the turbulence models used in the correlation analyses. More attention should be put into the meshing quality and to make sure the mesh suits the turbulence model and expected flow structures. The experimental results gathered during this thesis work will form a great foundation for investigating different turbulence models for a Formula student car application. Studies considering both the accuracy and computational time may be performed to arrive at the best possible CFD modelling for developing the aerodynamic design more accurately.

Chapter 7

Future work and suggested improvements

7.1 Wind tunnel testing

If similar experiments were to be performed again, the main recommended improvements are for the measurements and data acquisition techniques. By fully utilizing the Scanivalve MPS4264 up to 64 pressure taps may be placed around the model, creating a more detailed pressure map of several parts of the vehicle. Another good option is to use the pressure traversing system, making a detailed map of the wake behind the model and at several different locations in the test section. Finally, the new test section in the wind tunnel offers better optical access, meaning that using visualisation methods such as PIV is a good option to visualize the flow structures at certain areas around the vehicle model.

Looking at a more time and resource consuming option, the wind tunnel setup may be improved by implementing a rolling floor underneath the vehicle. As presented in chapter 3 more than 20% of the total downforce is lost when using a fixed floor compared to a rolling floor. While a ground effect plate improves the modelling of the area between the vehicle and ground it is not as accurate as having a rolling floor moving at the same velocity as the freestream air. Together with a rolling floor, a wind tunnel model with turning wheels will be needed to make the whole setup as realistic as possible. In order to construct this setup, a belt able to travel at the wind velocities of the wind tunnel will be required for the rolling floor. Motorized wheels rotating at the equivalent velocity as the belt will be needed for the model. The whole setup should be mounted to the force balance to be able to collect downforce measurements.

This setup will be very time consuming and require a lot of resources. While it has the potential to provide very good results for the aerodynamic design of the Revolve NTNU electric vehicles, it is not recommended to proceed with a project like this in the near future.

7.2 Track testing

For the aerodynamic development of the Revolve NTNU electric vehicles, time and resources should be put into developing good methods for aerodynamic validation during track testing. By collecting pressure and force data while driving the team members will gain great knowledge of the actual performance of the vehicle compared to the simulated performance.

The first suggestion is to add pressure taps to the suction side of the front and rear wings, similar to the wind tunnel model and to several professional motorsport teams. An EvoScann P-8A pressure scanner may be mounted inside the main elements and eight taps in two rows added to the suction side. A concept developed by the author for the 2021 Revolve NTNU electric vehicle is shown in figure 7.1. The pressure scanner is placed to the right in the figure, while tubing will go along the tracks in the element to each tap. The power and signal cables will be attached to the front wing fastener rods and connected to the low voltage system and CAN bus of the vehicle. A lid will be made to hide all the instrumentation to disturb the airflow as little as possible.

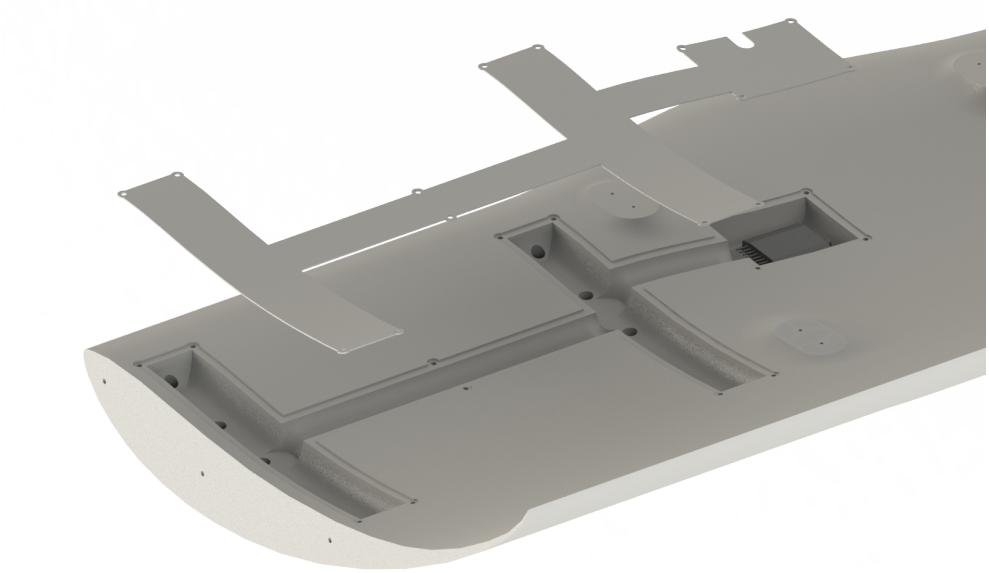

Figure 7.1: Pressure tapping concept on the rear wing of the 2021 Revolve NTNU electric vehicle. Exploded view render in SolidWorks

Another new measurement concept worth developing for the Revolve NTNU aerodynamics group is an aero rake/grid, which consists of an array of several Kiel probes. This technique is used in several motorsport categories to model the wake structures on various different areas of the car, most commonly the wheel wakes. As the wake behind the wheels is hard to model accurately in CFD and is a major

area of uncertainty in race car design, collecting measurements and mapping how the wake develops and behaves during track testing could prove very beneficial for the aerodynamic designers and the vehicle performance.

7.3 CFD simulation development

This project focused mostly on the steady k-ϵ model for the correlation analyses. While some other turbulence models was used as well, more thorough work should be done for determining which turbulence model has the best correlation with the experimental results gathered from the wind tunnel experiments. Both steady and unsteady turbulence models should be considered. It is also possible to investigate the possibility of using methods like the Detached eddy simulation (DES) for some baseline simulations during the design process. While this model was not a part of this thesis work, it may be worth looking into how well that correlates with the experimental data, taking the added computational cost into consideration. This topic is discussed in more detail by Mildestveit from 2019 [23].

Bibliography

[1] F. S. G. GmbH. (). 'Fsg: Formula student germany,' [Online]. Available: https://www.formulastudent.de/fsg/. (accessed: 08.06.2021.

[2] F. S. G. GmbH. (). 'Formula student rules 2020,' [Online]. Available: https://www.formulastudent.de/fsg/rules/. (accessed: 14.12.2020).

[3] R. NTNU. (). 'About us,' [Online]. Available: https://www.revolve.no/about-us. (accessed: 08.06.2021).

[4] F. S. G. GmbH. (). 'Formula student electric - world ranking list,' [Online]. Available: https://fs-world.org/E/. (accessed: 08.06.2021).

[5] A. Lara-Quintanilla, 'Development of a fast shape memory alloy based actuator for morphing airfoils,' p. 11, 2016. DOI: 10.4233/uuid:c0b3d6bc-9f30-420d-acc3-c2e542c529dd.

[6] J. D. A. Jr., *Fundamentals of aerodynamics*, ser. McGraw-Hill series in aeronautical and aerospace engineering. McGraw-Hill Education, 2017, ISBN: 9781259129919.

[7] J. Katz, *Race Car Aerodynamics: designing for speed*, ser. Automotive Books Manuals. Bentley Publishers, 1995, ISBN: 0-8376-0142-8.

[8] T. K. Guha, W. Oates and R. Kumar, 'Characterization of piezoelectric macrofiber composite actuated winglets,' *Smart Materials and Structures*, vol. 24, Jun. 2015. DOI: 10.1088/0964-1726/24/6/065043.

[9] J. Katz, 'Aerodynamics of race cars,' *Annual Review of Fluid Dynamics*, vol. 38, no. 1, pp. 27–63, 2006. DOI: 10.1146/annurev.fluid.38.050304.092016.

[10] J. Campbell-Brennan. (). 'Racecar vehicle dynamics explained,' [Online]. Available: https://www.racecar-engineering.com/tech-explained/racecar-vehicle-dynamics-explained/. (accessed: 06.06.2021).

[11] W. M. H. K. Versteeg, *An Introduction to Computational Fluid Dynamics: The Finite Volume Method*, ser. Pearson Education. Pearson Education Limited, 1995,2017, ISBN: 978-0-13-127498-3.

[12] P. G. e. a. J. Delery B. Chanetz, *Experimental Aerodynamics: An Introductory Guide*, ser. Springer Tracts in Mechanical Engineering. Springer Nature Switzerland, 2020, ISBN: 978-3-030-35562-3.

[13] A. P. William H. Rae Jr. Jewel B. Barlow, *Low-speed wind tunnel testing*, ser. Wind tunnels. John Wiley Sons, 1984,1999, ISBN: 0-471-55774-9.

[14] W. H. Hucho, *Aerodynamics of Road Vehicles*, ser. Motor vehicles — Aerodynamics. Butterworth-Heinemann Ltd, 1987, ISBN: 0-408-01422-9.

[15] B. G. Ben Redwood Filemon Schöffer, *The 3D Printing Handbook: Technologies, design and application*. Coers Roest, 2017, ISBN: 978-90-827485-0-5.

[16] D. M. Olaf Diegel Axel Nordin, *A Practical Guide to Design for Additive Manufacturing*, ser. Springer Series in Advanced Manufacturing. Springer Nature Singapore, 2020, ISBN: 978-981-13-8281-9.

[17] J. Hearst. (). 'Fluid mechanics laboratory and wind tunnel,' [Online]. Available: `https://www.ntnu.edu/ept/laboratories/aerodynamic`. (accessed: 10.06.2021).

[18] *6-component force balance*, Carl Schenck AG, 1984.

[19] *High accuracy low differential pressure transducer*, Model 239, Rev. Q, Setra Systems, Inc., Sep. 2020.

[20] *Pressure / flow calibrator*, FCO560, Furness Controls, Oct. 2017.

[21] *Miniature pressure scanner*, MPS4264, Scanivalve Corp., 2017.

[22] K. F. Sagmo, 'Computational fluid dynamics simulations of a Formula Student race car - Effects predicted by the modelling of a steady state cornering vehicle,' M.S. thesis, NTNU, Norway, 2016.

[23] J. H. Mildestveit, 'Application of Detached Eddy Simulation on a Formula Student Race Car,' M.S. thesis, NTNU, Norway, 2019.

Appendix A

Residuals and parameter plots

Steady k-ϵ

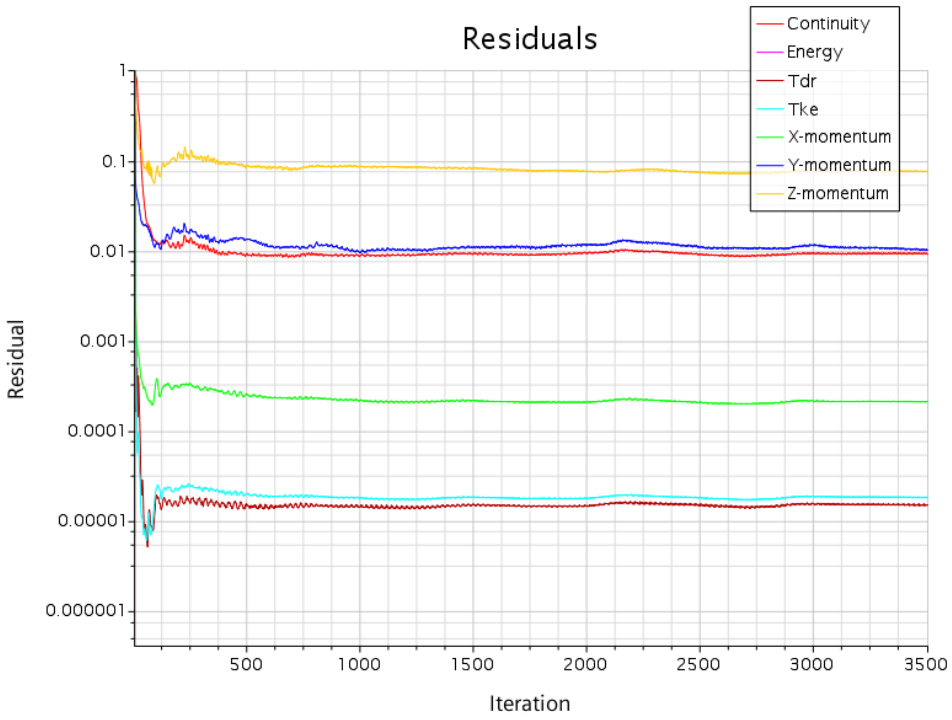

Figure A.1: Residuals steady k-ϵ, $V_\infty = 60km/h = 16.67m/s$, $\psi = 0deg$, half-car

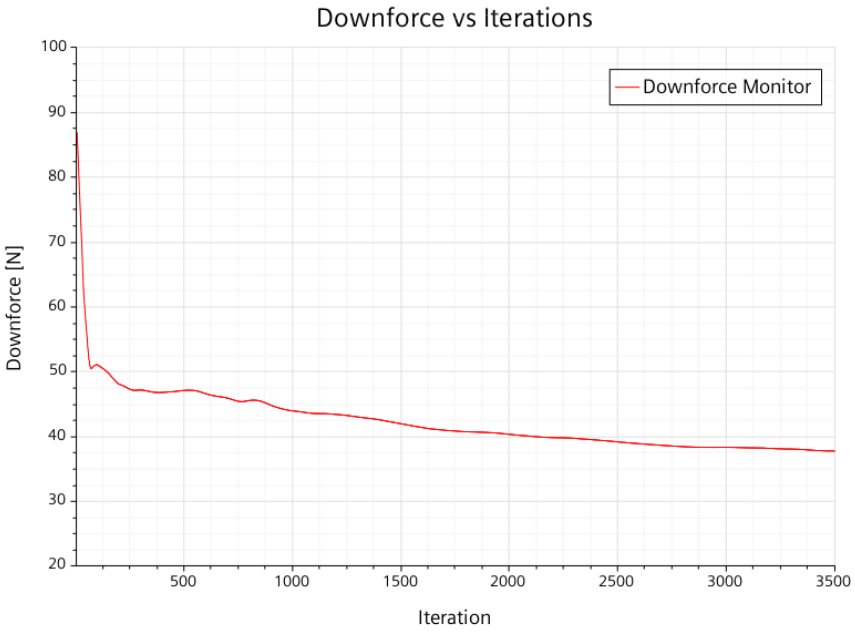

Figure A.2: Downforce monitor steady k-ϵ, $V_\infty = 60km/h = 16.67m/s$, $\psi = 0deg$, half-car

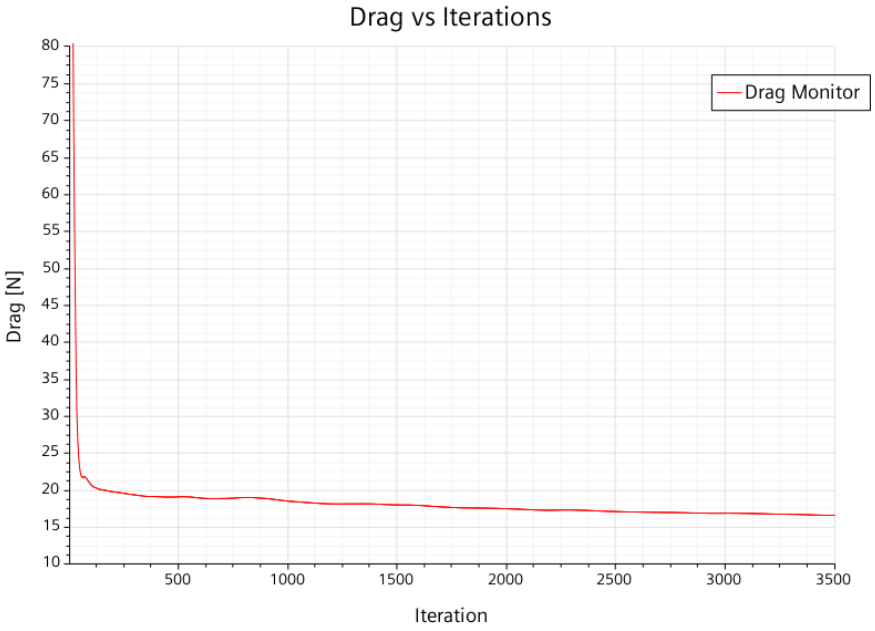

Figure A.3: Drag monitor steady k-ϵ, $V_\infty = 60km/h = 16.67m/s$, $\psi = 0deg$, half-car

Unsteady k-ϵ

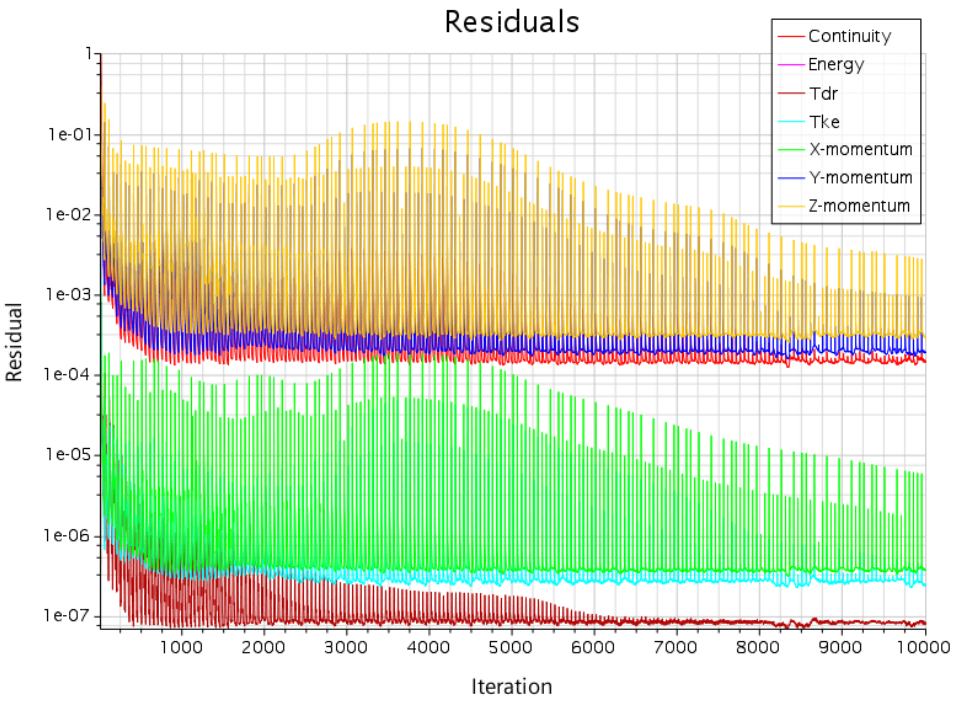

Figure A.4: Residuals unsteady k-ϵ, $V_\infty = 60km/h = 16.67m/s$, $\psi = 0deg$, half-car

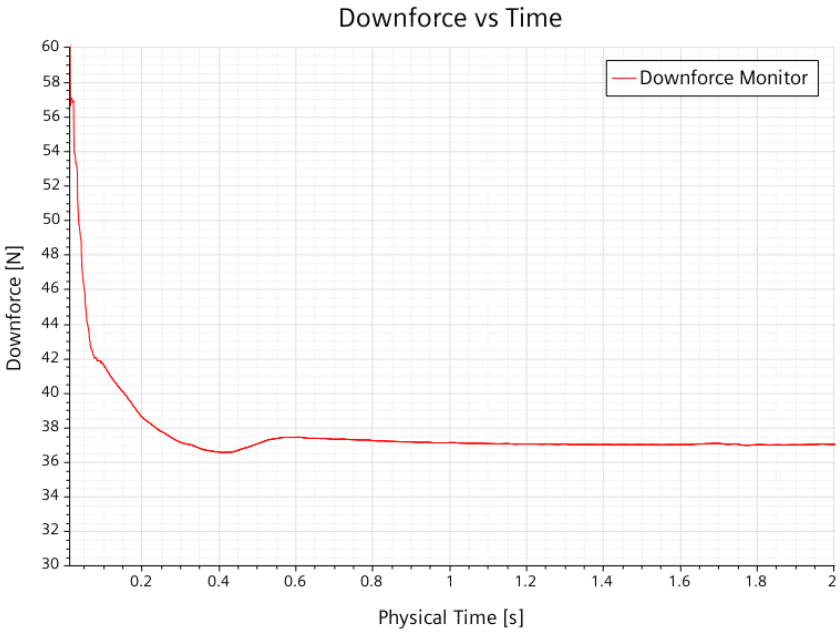

Figure A.5: Downforce monitor unsteady k-ϵ, $V_\infty = 60km/h = 16.67m/s$, $\psi = 0deg$, half-car

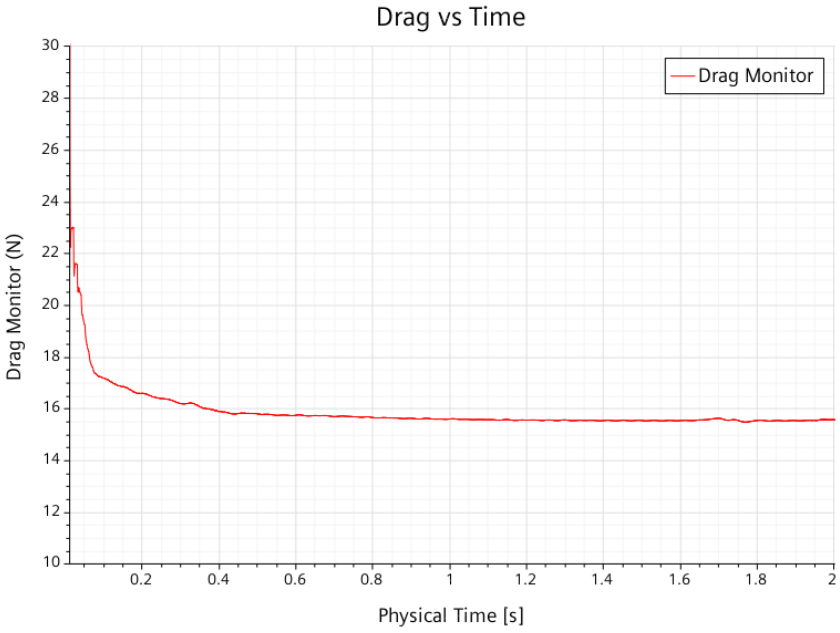

Figure A.6: Drag monitor unsteady k-ϵ, $V_\infty = 60km/h = 16.67m/s$, $\psi = 0deg$, half-car

Steady k-ω SST

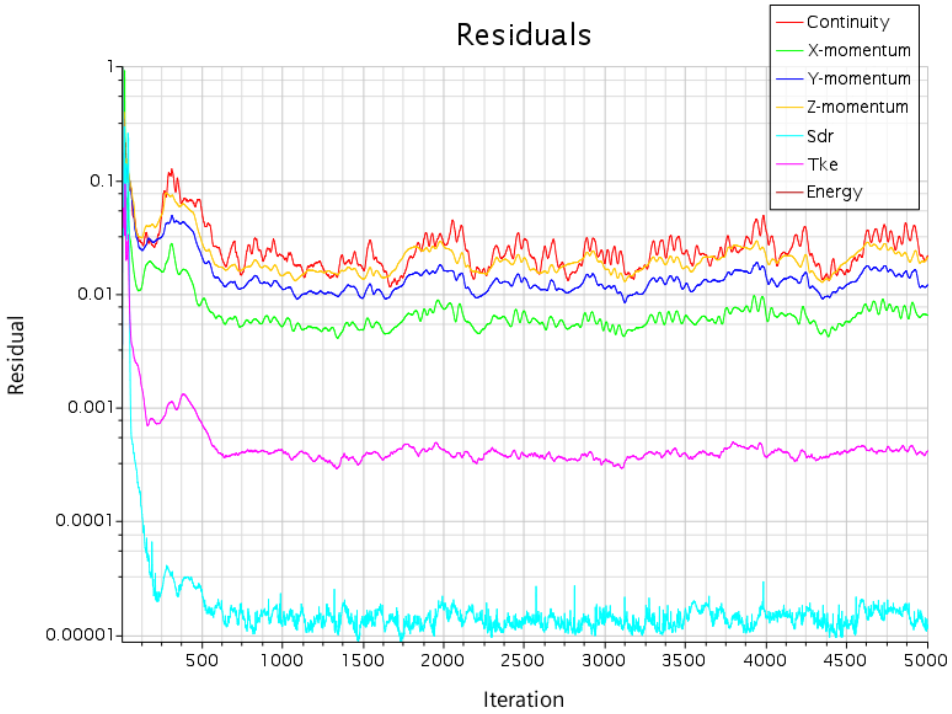

Figure A.7: Residuals steady k-ω SST, $V_\infty = 60km/h = 16.67m/s$, $\psi = 0deg$, half-car

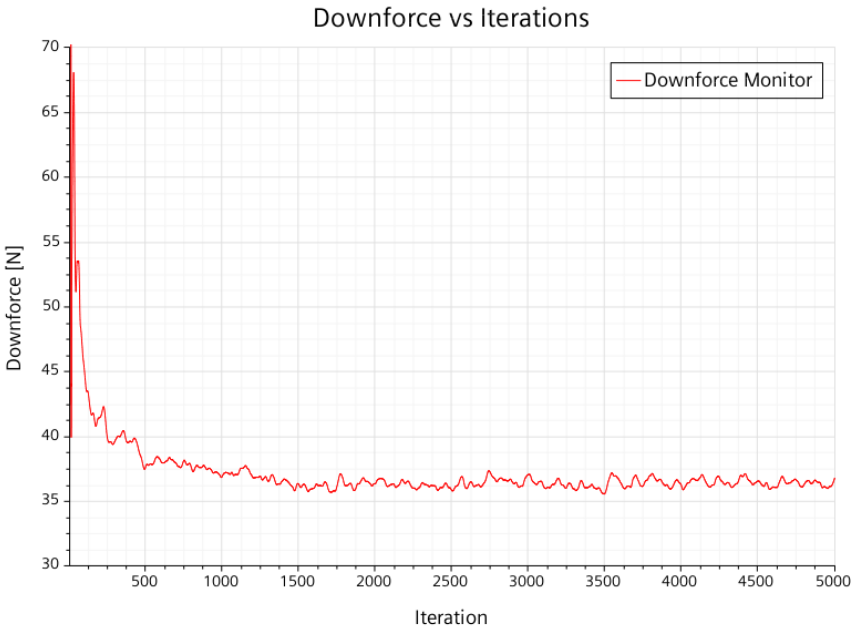

Figure A.8: Downforce monitor steady k-ω SST, $V_\infty = 60km/h = 16.67m/s$, $\psi = 0deg$, half-car

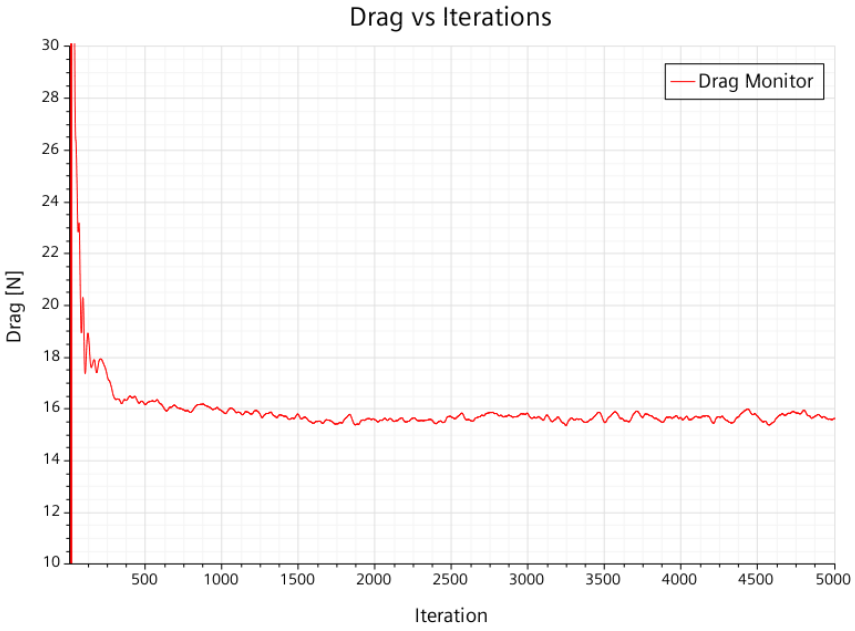

Figure A.9: Drag monitor steady k-ω SST, $V_\infty = 60km/h = 16.67m/s$, $\psi = 0deg$, half-car

Unsteady k-ω SST

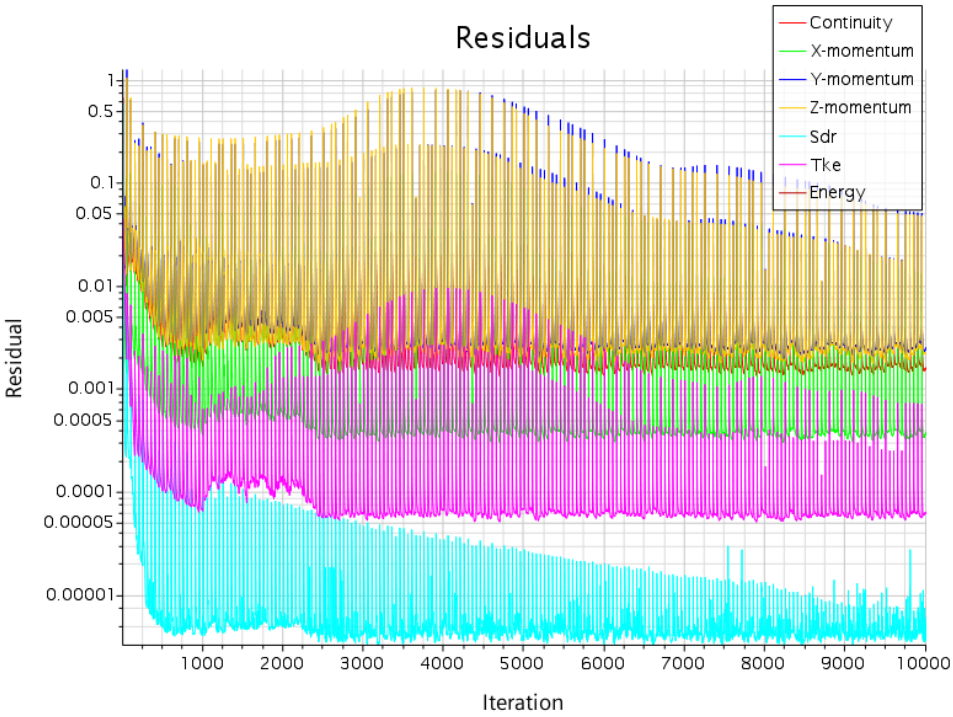

Figure A.10: Residuals unsteady k-ω SST, $V_\infty = 60km/h = 16.67m/s$, $\psi = 0deg$, half-car

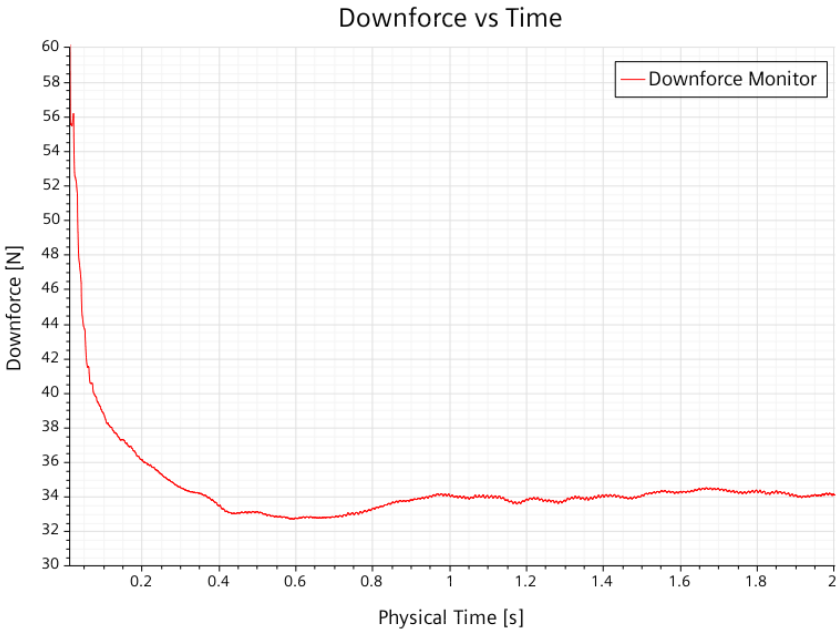

Figure A.11: Downforce monitor unsteady k-ω SST, $V_\infty = 60km/h = 16.67m/s$, $\psi = 0deg$, half-car

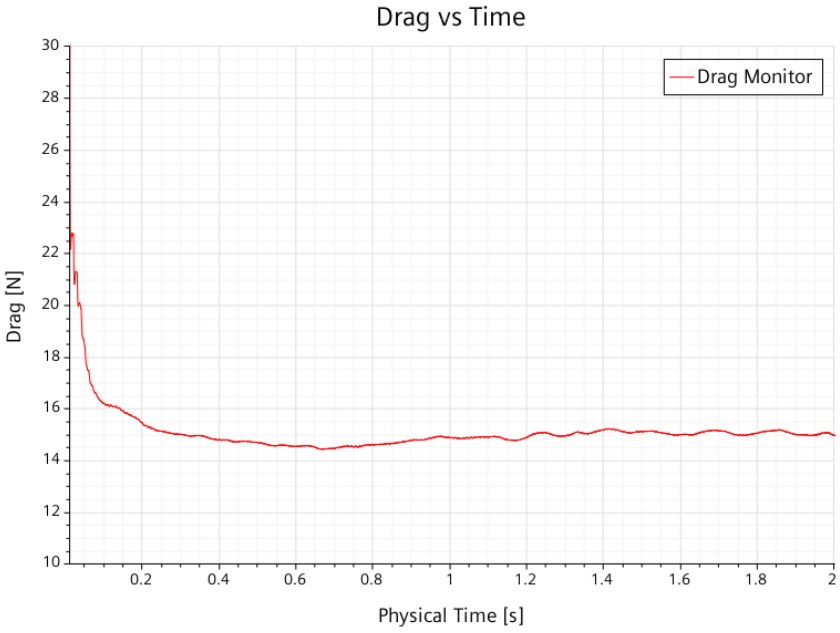

Figure A.12: Drag monitor unsteady k-ω SST, $V_\infty = 60km/h = 16.67m/s$, $\psi = 0deg$, half-car

Appendix B

Pressure plots, k-ϵ vs experimental

Front wing

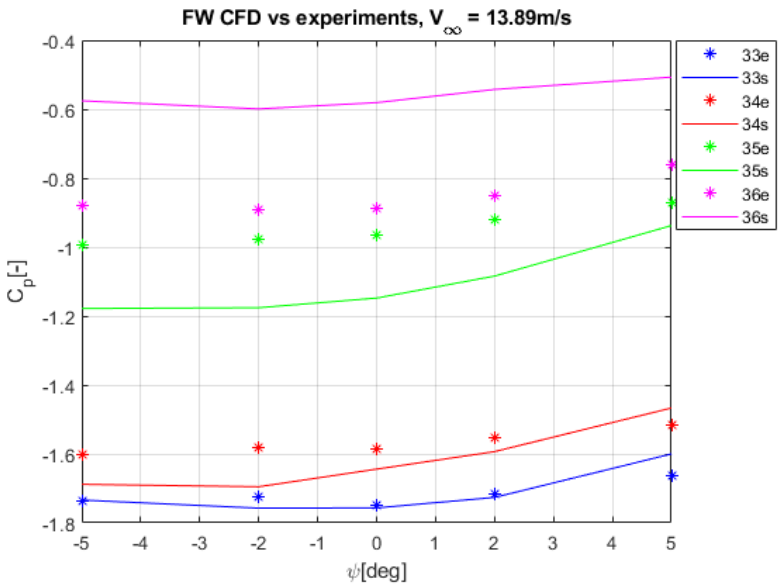

Figure B.1: Static pressure measurements for front wing taps 33-36 at $V_\infty = 50km/h = 13.89m/s$

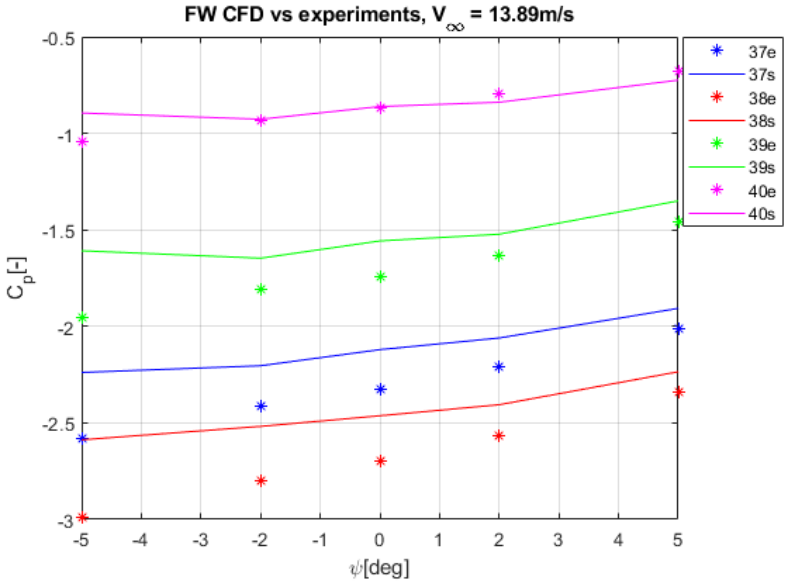

Figure B.2: Static pressure measurements for front wing taps 37-40 at $V_\infty = 50km/h = 13.89m/s$

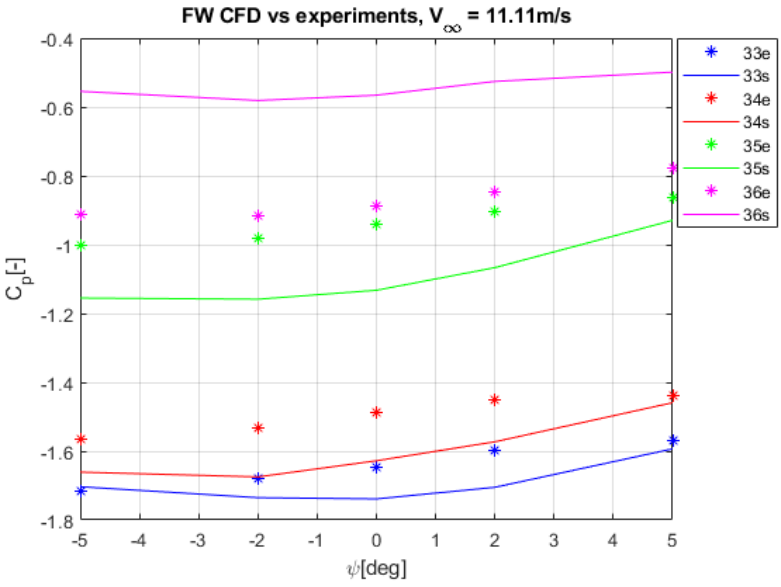

Figure B.3: Static pressure measurements for front wing taps 33-36 at $V_\infty = 40km/h = 11.11m/s$

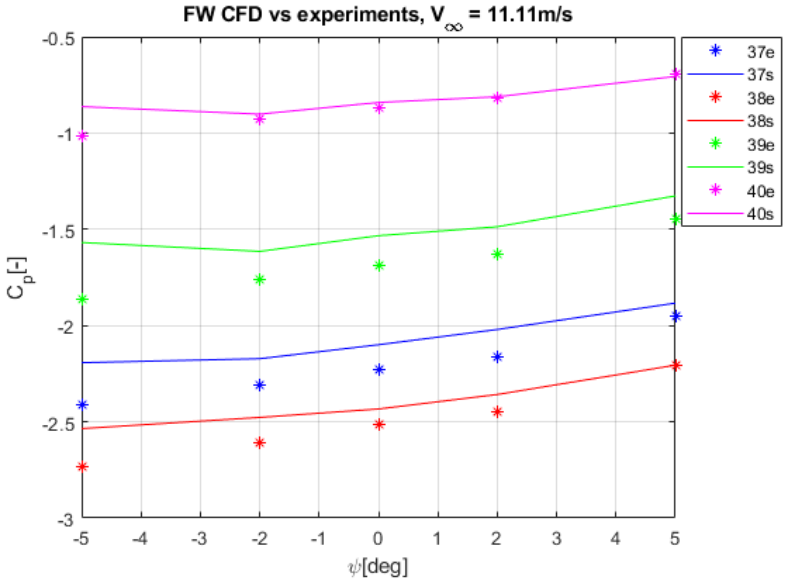

Figure B.4: Static pressure measurements for front wing taps 37-40 at $V_\infty = 40km/h = 11.11m/s$

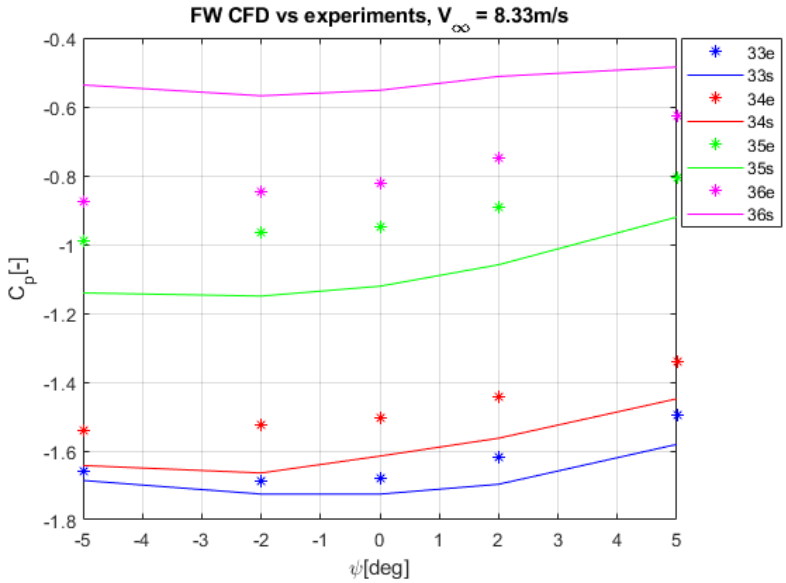

Figure B.5: Static pressure measurements for front wing taps 33-36 at $V_\infty = 30km/h = 8.33m/s$

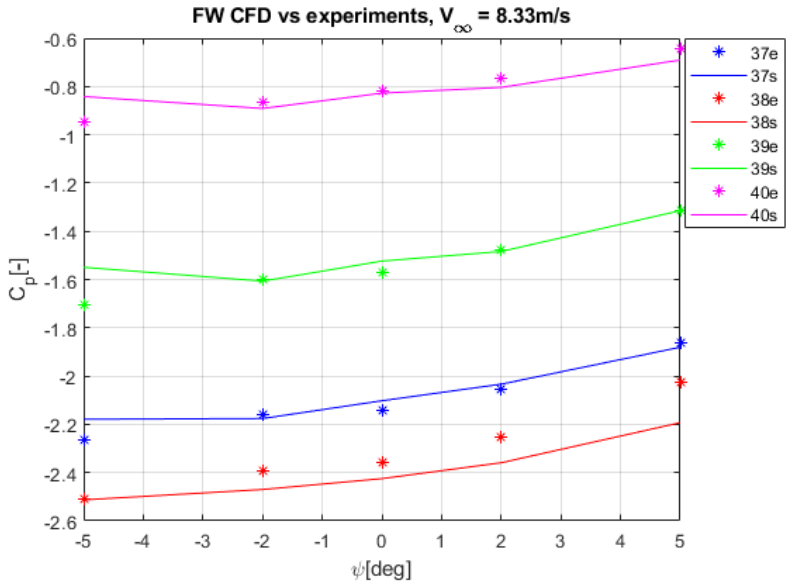

Figure B.6: Static pressure measurements for front wing taps 37-40 at $V_\infty = 30km/h = 8.33m/s$

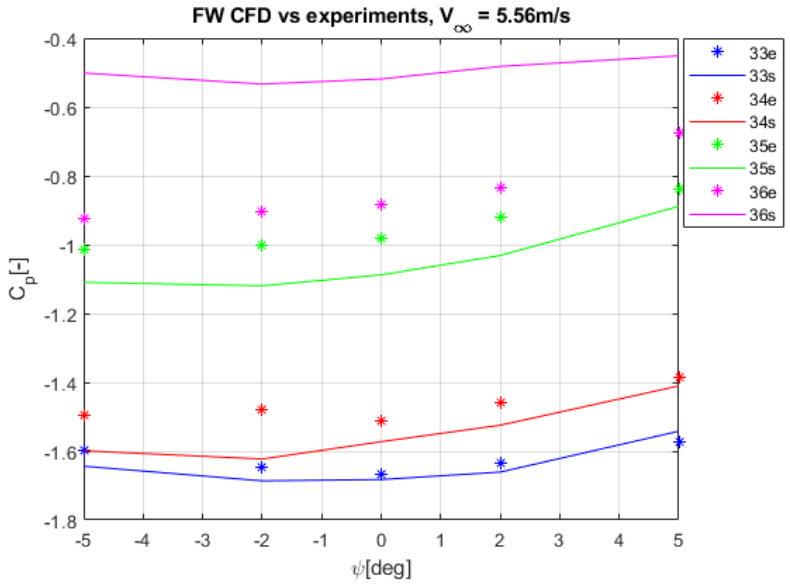

Figure B.7: Static pressure measurements for front wing taps 33-36 at $V_\infty = 20km/h = 5.56m/s$

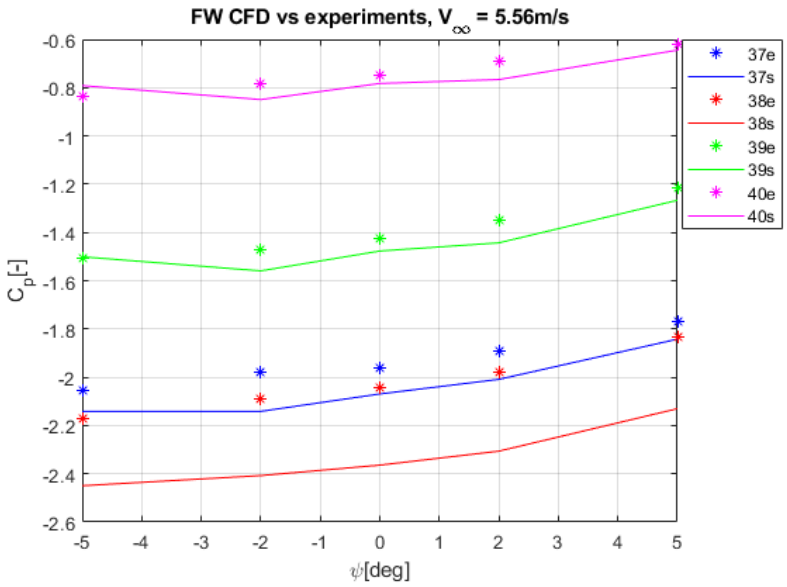

Figure B.8: Static pressure measurements for front wing taps 37-40 at $V_\infty = 20km/h = 5.56m/s$

Undertray

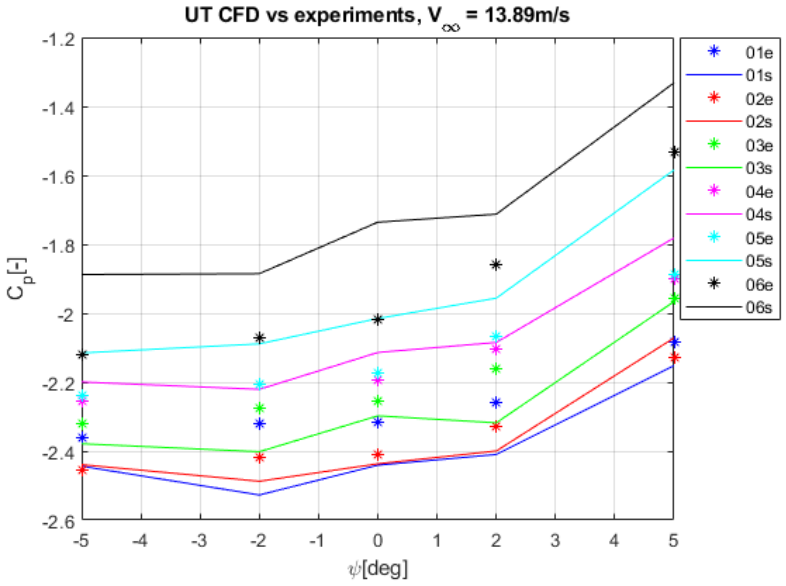

Figure B.9: Static pressure measurements for undertray taps 01-06 at $V_\infty = 50km/h = 13.89m/s$

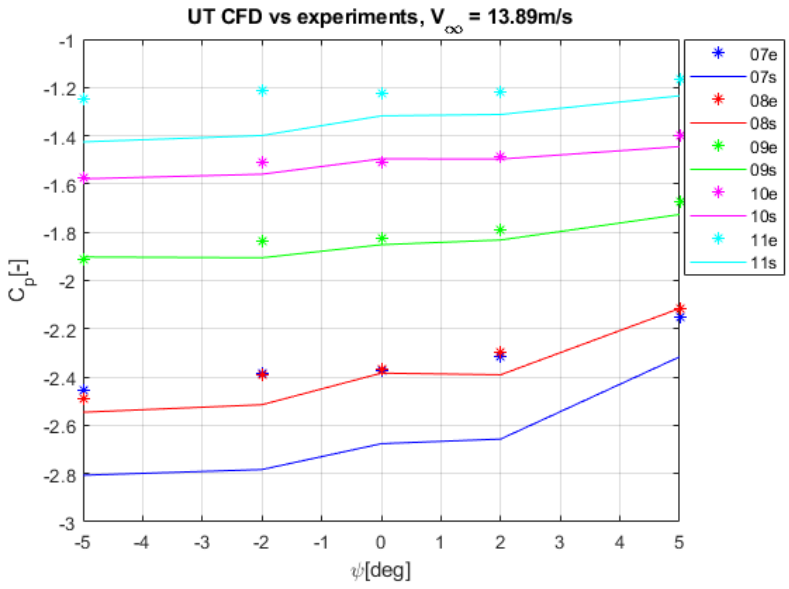

Figure B.10: Static pressure measurements for undertray taps 07-11 at $V_\infty = 50km/h = 13.89m/s$

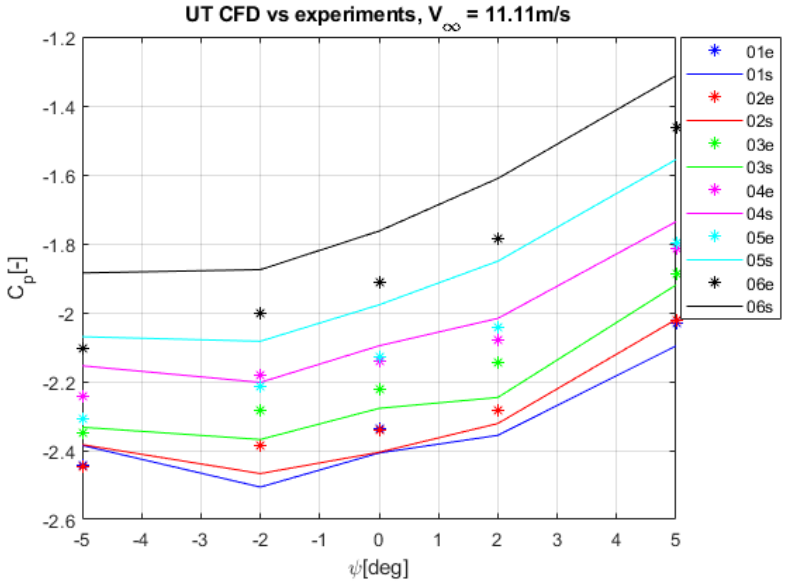

Figure B.11: Static pressure measurements for undertray taps 01-06 at $V_\infty = 40km/h = 11.11m/s$

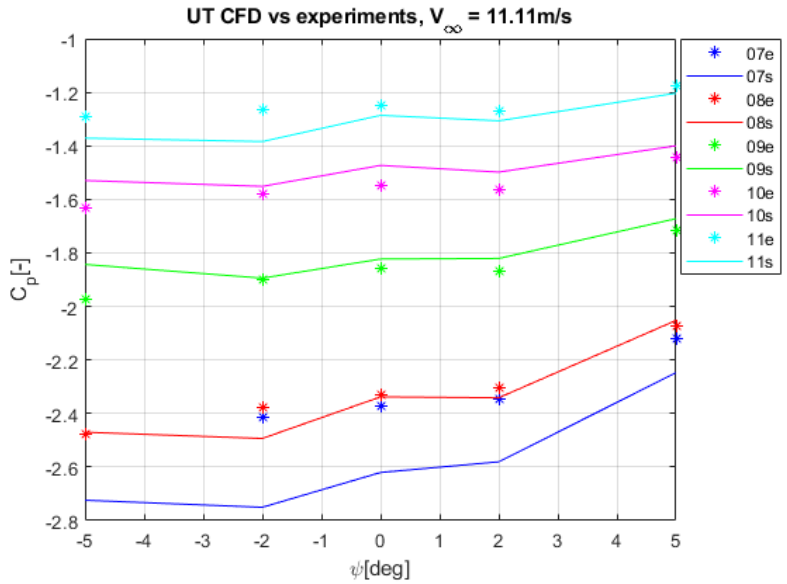

Figure B.12: Static pressure measurements for undertray taps 07-11 at $V_\infty = 40km/h = 11.11m/s$

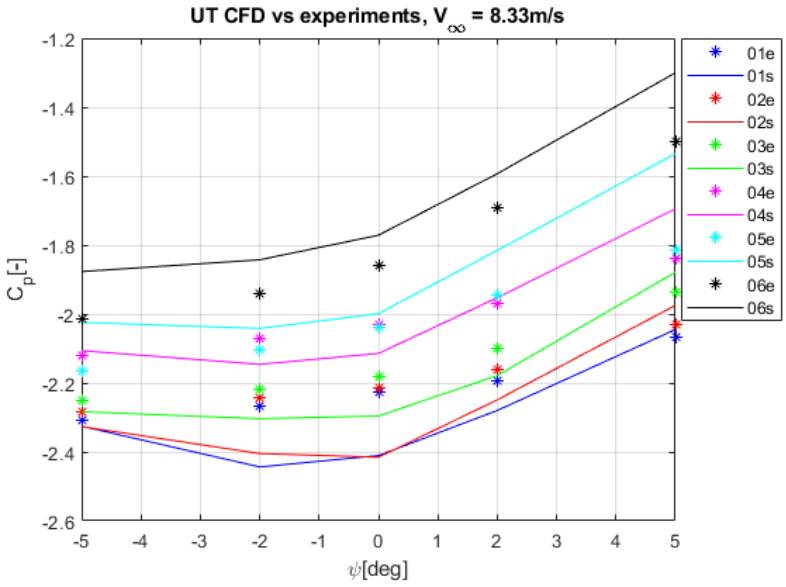

Figure B.13: Static pressure measurements for undertray taps 01-06 at $V_\infty = 30km/h = 8.33m/s$

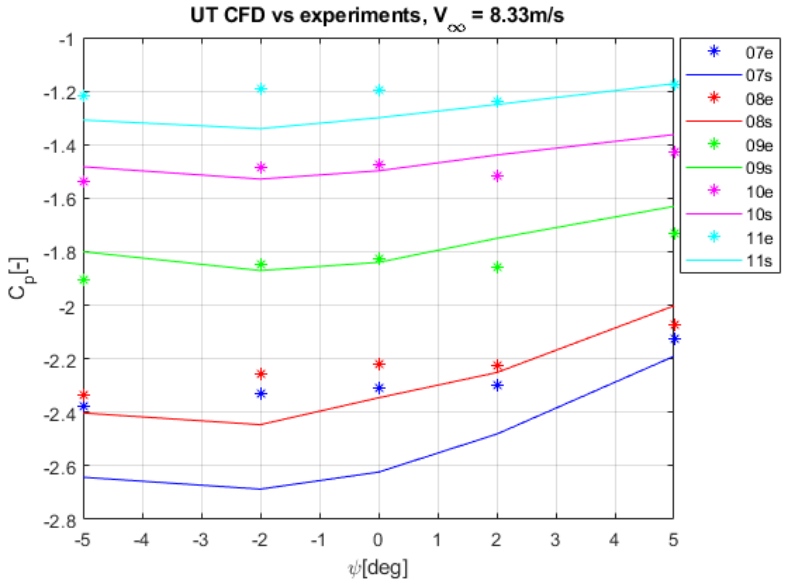

Figure B.14: Static pressure measurements for undertray taps 07-11 at $V_\infty = 30km/h = 8.33m/s$

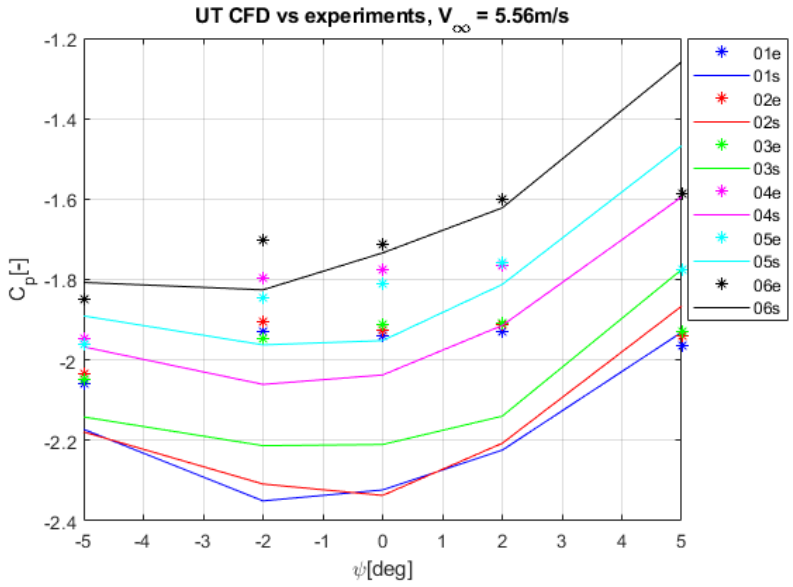

Figure B.15: Static pressure measurements for undertray taps 01-06 at $V_\infty = 20km/h = 5.56m/s$

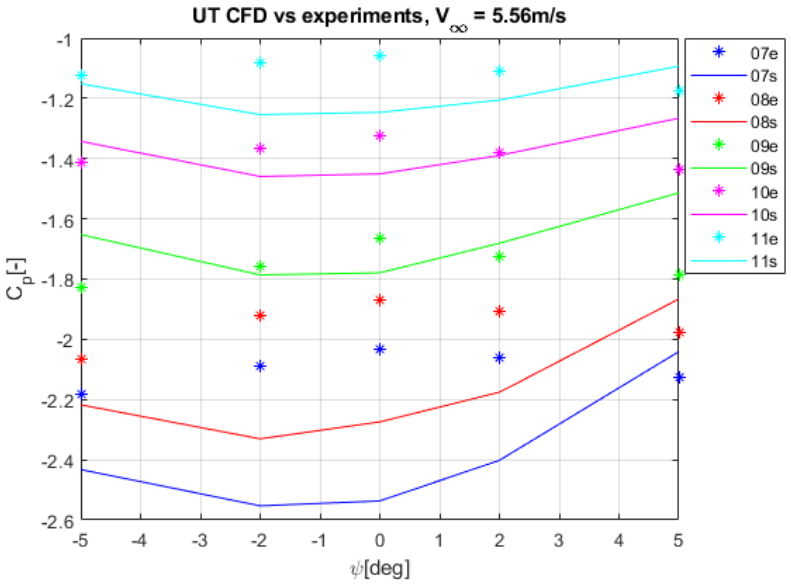

Figure B.16: Static pressure measurements for undertray taps 07-11 at $V_\infty = 20km/h = 5.56m/s$

Rear wing

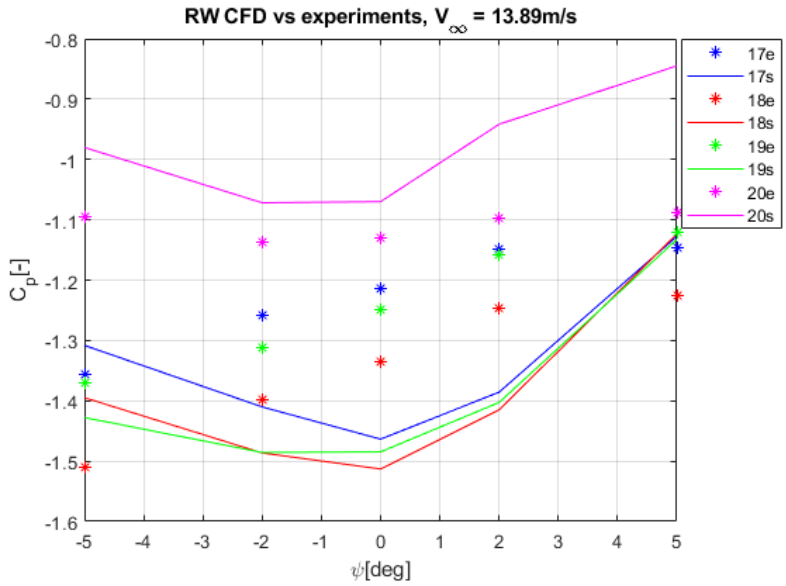

Figure B.17: Static pressure measurements for rear wing taps 17-20 at $V_\infty = 50km/h = 13.89m/s$

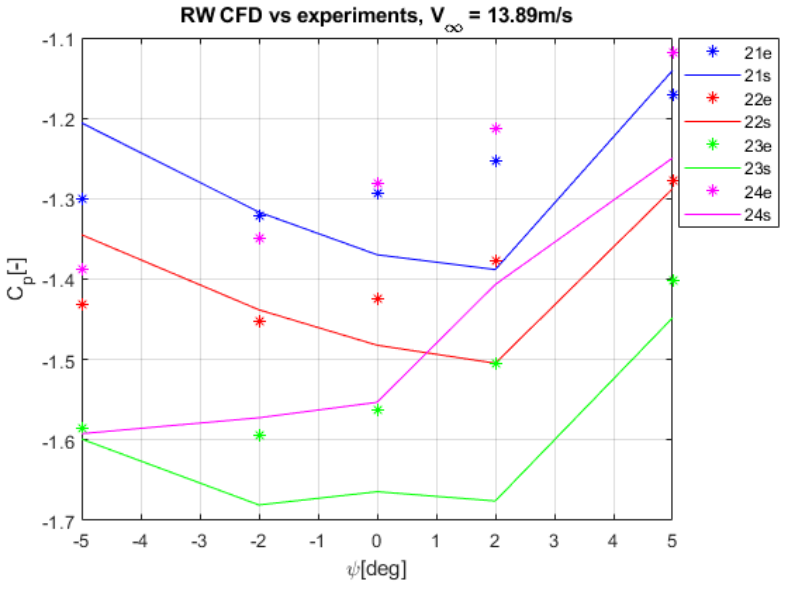

Figure B.18: Static pressure measurements for rear wing taps 21-24 at $V_\infty = 50km/h = 13.89m/s$

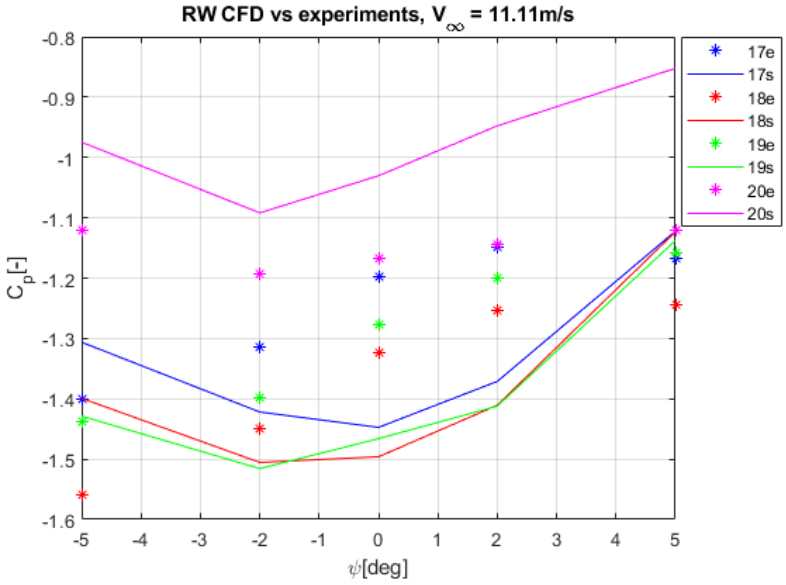

Figure B.19: Static pressure measurements for rear wing taps 17-20 at $V_\infty = 40km/h = 11.11m/s$

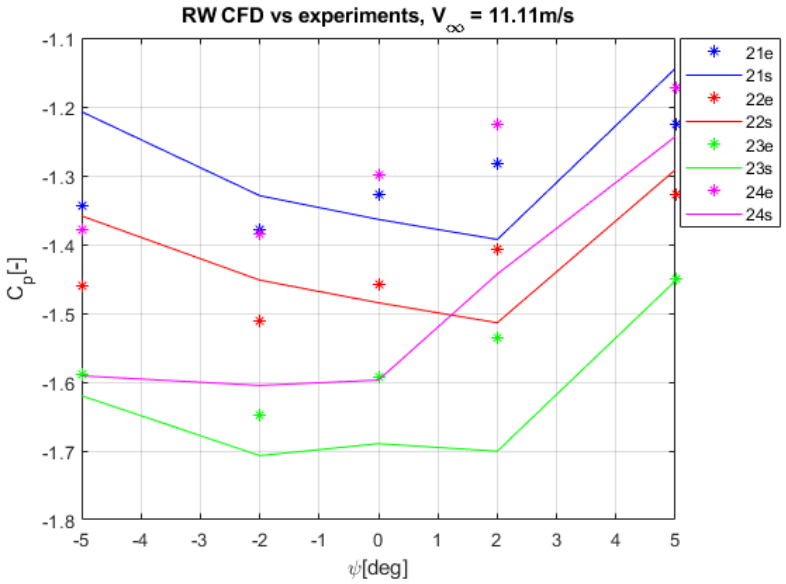

Figure B.20: Static pressure measurements for rear wing taps 21-24 at $V_\infty = 40km/h = 11.11m/s$

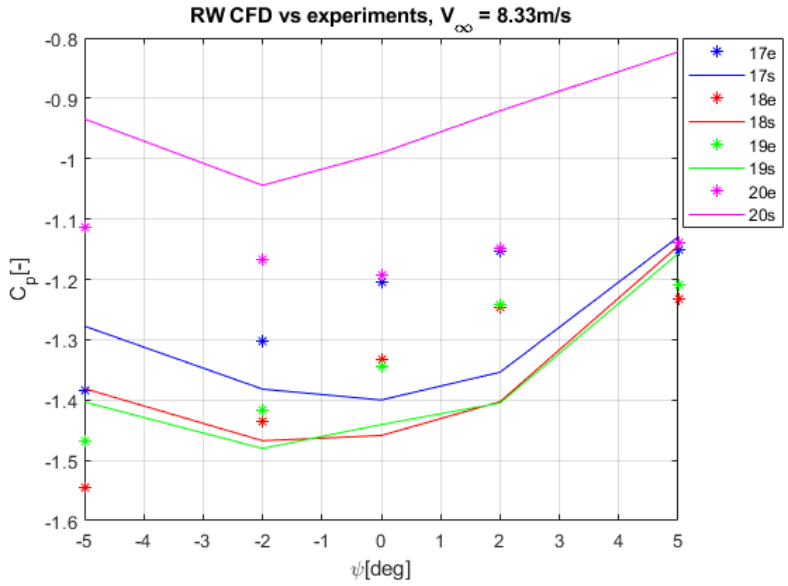

Figure B.21: Static pressure measurements for rear wing taps 17-20 at $V_\infty = 30km/h = 8.33m/s$

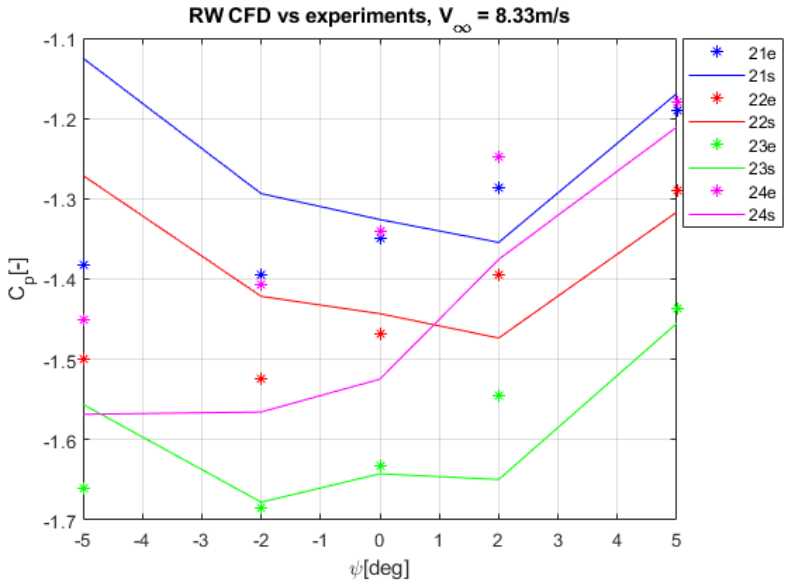

Figure B.22: Static pressure measurements for rear wing taps 21-24 at $V_\infty = 30km/h = 8.33m/s$

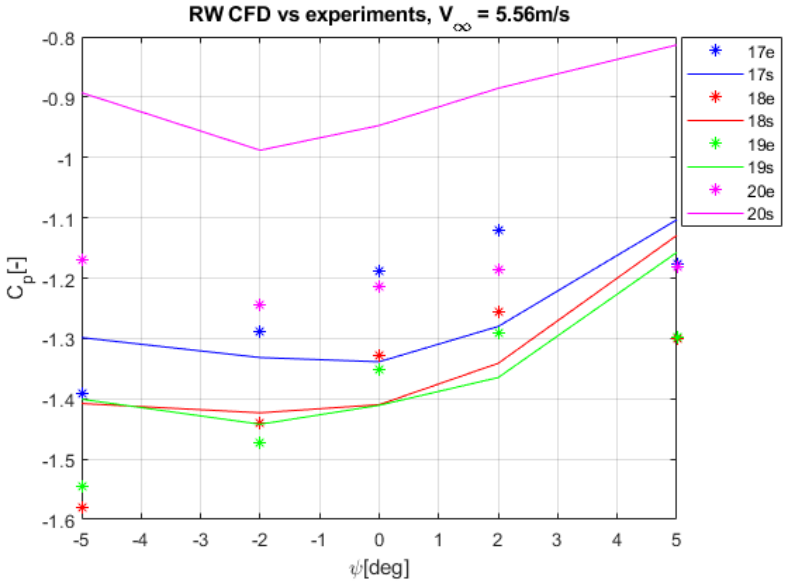

Figure B.23: Static pressure measurements for rear wing taps 17-20 at $V_\infty = 20km/h = 5.56m/s$

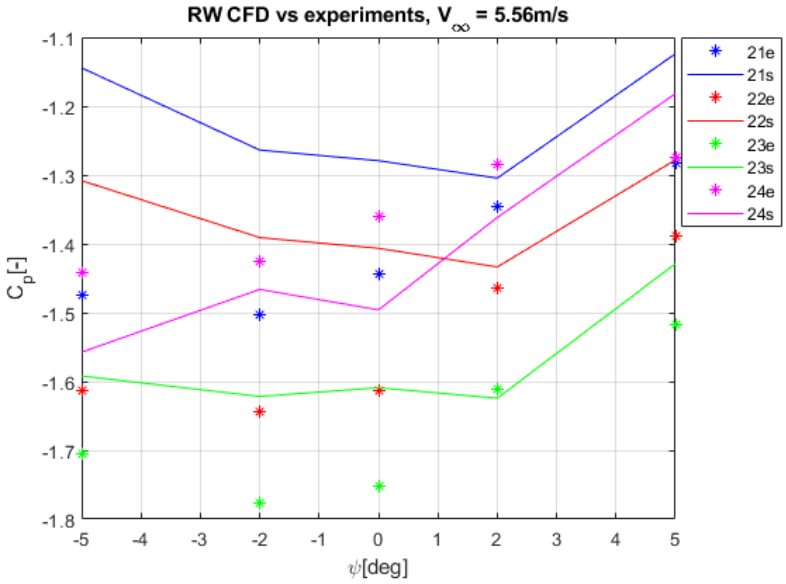

Figure B.24: Static pressure measurements for rear wing taps 21-24 at $V_\infty = 20km/h = 5.56m/s$

Appendix C

Standard deviations for pressure and force measurements

Standard deviation Pressure scanner (Pa)

10km/h	2.78m/s				
Channel	-5deg	-2deg	0deg	2deg	5deg
1	0.687531769	0.695719537	0.644974829	0.743228425	0.731544049
2	1.258019768	1.270342041	1.251170963	1.308741757	1.312137445
3	0.953058424	0.977292149	0.951091897	1.008087879	1.041849698
4	1.231420794	1.242749124	1.241004111	1.293747693	1.350333203
5	0.712262823	0.685714219	0.631918103	0.743445813	0.7981814
6	0.93334074	0.873996867	0.825184265	0.989658083	1.083834722
7	0.671739688	0.668766239	0.608337549	0.671929154	0.69678932
8	0.878194835	0.888848653	0.864391412	0.947520949	0.93822823
9	0.724860978	0.745185549	0.661408345	0.767651269	0.782546267
10	1.059387813	1.07140856	1.050420378	1.12326968	1.134646352
11	0.790891502	0.795394865	0.789963065	0.841211132	0.832552467
17	0.661652576	0.639733973	0.64460566	0.712233719	0.628306457
18	1.131619686	1.140772068	1.170807617	1.221582024	1.125161634
19	0.91938968	0.90255037	0.956876234	0.976327616	0.892753972
20	1.205376694	1.218231998	1.326819464	1.221852401	1.214283835
21	0.654360025	0.678364715	0.666562562	0.678288019	0.680726976
22	0.832522322	0.854960568	0.863416275	0.850094675	0.833217558
23	0.836054955	0.844538787	0.847238293	0.871296395	0.85842803
24	1.08276048	1.087351356	1.124952356	1.071402942	1.111397166
33	0.905374494	0.929811882	0.94836107	0.946904974	0.981353677
34	0.783159857	0.772648948	0.782802084	0.789220384	0.786107303
35	0.851912668	0.859511482	0.858706954	0.87703471	0.85998322
36	0.820504887	0.832216059	0.840974995	0.85209642	0.836536748
37	0.807797612	0.850667523	0.845921323	0.844526258	0.858450336
38	0.711052344	0.739117771	0.718975589	0.731708814	0.719754931
39	0.720199344	0.747207981	0.728085078	0.750818244	0.734555901
40	0.634630698	0.647764024	0.655120466	0.651981222	0.649332859

20km/h 5.56m/s

Channel	-5deg	-2deg	0deg	2deg	5deg
1	1.64364361	1.623277106	1.474049089	1.610094831	1.585701362
2	1.955553099	1.875275154	1.769175895	1.917792623	1.950506429
3	1.801949025	1.778687887	1.667282805	1.685160001	1.730405151
4	1.989319392	1.985519231	1.840487405	1.985411287	1.967371413
5	2.629593798	2.433924595	2.217661754	2.654148404	2.931319704
6	3.135441211	3.121972705	2.937410931	3.500285489	3.641598301
7	1.685982235	1.560373783	1.430176852	1.591763879	1.597045846
8	1.83948845	1.682780491	1.567693268	1.77106731	1.826698846
9	2.147169418	1.897596892	1.759874639	2.102462739	2.087054927
10	2.138486561	1.994212534	1.916531885	2.178718637	2.226015056
11	1.695743323	1.600186135	1.486077009	1.71859595	1.6881934
17	1.856945033	1.657230126	1.341840129	1.831678324	1.429099693
18	2.186106411	2.110735408	1.875315386	2.141691007	1.763768244
19	2.529272304	2.637346221	2.692293695	2.380026878	2.014422642
20	3.235709112	3.434017797	3.908167454	3.043443854	2.739401633
21	1.481570131	1.45925209	1.578167889	1.671131009	1.744261905
22	1.758117224	1.772129466	1.990101276	1.937994671	2.120823718
23	2.237916436	2.20072567	2.598347632	2.352155133	2.654608208
24	2.974442982	3.017815569	3.631058169	2.749481483	2.893767981
33	1.132213835	1.20268584	1.195810985	1.243414463	1.152638012
34	0.996325148	1.054411218	1.091579191	1.024207728	1.028196564
35	1.117038219	1.139566464	1.195868724	1.093840261	1.088973866
36	1.542220543	1.677306273	1.880915876	1.391275181	1.311171574
37	1.211983178	1.365124526	1.452299485	1.279014243	1.283343165
38	1.405156124	1.532642455	1.596102488	1.463543533	1.447625841
39	1.305156539	1.371530407	1.413035045	1.327306941	1.270487649
40	1.386597829	1.369440644	1.49451686	1.301372804	1.205654283

30km/h 8.33m/s

Channel	-5deg	-2deg	0deg	2deg	5deg
1	4.005414819	4.084780403	4.087422872	3.759534951	3.802677277
2	4.069446162	4.213199236	4.456322247	3.912373325	3.978663754
3	3.926722001	4.054641275	3.874236559	3.916899678	4.098281104
4	4.275016127	4.483044914	4.444324012	4.195884861	4.137062477
5	6.925705724	6.283079361	5.385310923	7.406855923	8.239902738
6	9.226568841	8.292766971	7.020686254	9.805057241	9.705176627
7	3.638496419	3.716921771	3.643880128	3.718268978	3.808669539
8	3.880557694	3.771078988	3.701709915	4.001775008	4.051340123
9	3.693877655	3.543717933	3.499168884	3.716255378	3.74881484
10	3.582950326	3.619787365	3.505125075	3.704080429	3.78642913
11	3.139647102	3.206340549	2.993591383	3.39565757	3.374962214
17	4.437510243	3.646781288	3.053458602	4.316295085	3.293517946
18	4.819157077	4.510244812	3.974598595	4.647309311	3.671355893
19	6.229339133	6.365078359	6.214821977	5.634642685	4.71838371
20	7.903943171	8.480686413	9.133267477	7.113620496	6.303097764
21	3.25445567	3.07812243	3.382211293	3.672008796	3.878770861
22	3.724803635	3.657625755	3.977666727	4.165267815	4.627462442
23	4.868358106	4.920219744	5.369078573	5.25837617	5.918203393
24	6.213481812	6.249664739	6.715183106	6.159154285	6.248218462
33	2.844322055	2.848876923	3.079967671	2.626577194	2.482280925
34	2.494398164	2.555884151	2.711658142	2.251633578	2.218825927
35	2.483745363	2.482857647	2.564099519	2.416876905	2.404526978
36	4.286941477	4.429245701	4.503582189	4.094272565	3.970928996
37	2.575943823	2.536230839	2.532387959	2.421035599	2.549862709
38	2.932561043	3.022297685	2.815491987	2.914909096	2.981055113
39	2.482578973	2.533324474	2.418200967	2.451995104	2.509876387
40	2.606086306	2.578797422	2.589955615	2.541710229	2.655777079

40km/h	11.11m/s				
Channel	-5deg	-2deg	0deg	2deg	5deg
1	8.328992051	8.285781568	8.043244025	8.205884001	8.789824339
2	7.939374846	8.36707474	8.843378607	7.715393464	8.286152369
3	7.396424716	7.806997554	7.417092861	7.493516702	8.151334306
4	8.356803775	8.737741357	8.367487292	7.980570837	8.46124526
5	12.68919362	11.34251569	10.54230227	13.71538229	16.6749389
6	15.66000957	14.75162389	12.76316145	17.30628535	19.94357924
7	7.034495464	7.064178566	7.208315992	7.267213198	7.853777334
8	7.745754642	7.480009103	7.33803752	7.596235351	8.42122497
9	6.229030283	6.296875378	6.123848482	5.982023404	6.36994661
10	6.319225944	6.448346917	6.113232012	6.275970483	6.437300084
11	5.63958369	5.602672343	5.712465687	5.820458137	6.00146711
17	7.15326453	6.569285034	5.367118248	7.325071882	6.070912455
18	8.158045716	8.08243061	7.277787171	7.653863833	6.570785227
19	11.2149567	12.30990364	11.7810474	9.922184383	8.755856899
20	15.08371883	16.44184341	17.4004449	13.36040474	11.81537011
21	5.665622885	5.308361699	5.689600991	6.248365882	6.928758935
22	6.479909267	6.292098581	6.847812721	6.830582725	8.067644213
23	8.459641618	8.778216225	9.280348415	8.579871672	10.59446875
24	10.20698338	10.50492174	10.91317404	10.10364876	11.26081249
33	5.014958528	5.442958735	5.653667766	4.907620361	5.07826908
34	4.563093424	4.926842035	5.011847525	4.475312152	4.513052924
35	4.210197008	4.333459686	4.011068965	4.464910425	4.457281778
36	6.24242168	6.499277104	5.89718127	6.705589602	6.618862403
37	4.390552524	4.219389594	4.590084746	4.295606059	4.702938246
38	5.117988279	4.91044483	5.130141055	5.254725093	5.960757363
39	4.334052714	4.067252311	4.234368445	4.416016186	4.804293252
40	4.877727139	4.437164056	4.350739728	4.840920396	4.879747922

50km/h 13.89m/s

Channel	-5deg	-2deg	0deg	2deg	5deg
1	11.69072648	11.92293536	12.08369859	11.6133536	12.66103577
2	12.94882176	14.01634	15.94601604	12.18955941	12.33234308
3	11.53782581	12.21512863	12.2046414	10.6399379	11.42857535
4	12.9483535	14.40979866	14.42130144	12.23394507	12.62306763
5	19.93632828	19.11956422	17.53035697	20.49760637	23.26325505
6	24.35115599	23.22156354	20.77233647	25.10705537	25.9518839
7	10.97361723	11.49585279	11.83118736	10.51818035	11.21853713
8	12.05088559	12.3636817	12.39373175	11.57401747	11.97291092
9	9.33084487	9.809313814	9.845809406	9.061682429	9.178551825
10	9.474836049	9.979380326	9.790611725	9.137697759	8.922214623
11	8.399142188	8.858693142	9.364995974	8.610236964	8.677623624
17	11.42366924	10.31259843	8.590241417	12.02772825	9.96972327
18	13.35886596	13.24323698	11.55738412	13.16462589	11.18566779
19	17.84518711	19.19396017	17.71912731	16.99862642	14.66373251
20	23.80212006	26.29270518	26.1891277	22.83341525	19.34766457
21	8.824878992	8.394125615	9.088365623	9.625856587	11.00364783
22	10.37912269	10.19837766	11.04574259	10.98102632	12.57086716
23	13.8136033	14.09807045	15.12862854	13.99151507	15.808192
24	15.63186901	15.89982842	16.74965377	15.27676798	16.17236187
33	7.800801523	7.770268231	7.188924368	7.840448109	7.49500039
34	7.002880943	6.783539615	6.713766989	7.272181479	7.523135151
35	5.716252466	5.188638046	5.358880653	6.296599412	6.875430729
36	6.836004298	6.63764446	7.211060377	7.538439521	8.631975773
37	7.699410052	7.116217823	7.282139463	8.112267609	7.59321223
38	9.299299165	8.516707839	8.482751374	10.04020786	9.743444936
39	7.530338315	6.789100125	6.736729941	7.995636139	7.695772108
40	7.740266928	7.623387217	6.875958625	8.098582857	8.103044088

60km/h	16.67m/s				
Channel	-5deg	-2deg	0deg	2deg	5deg
1	16.63694716	18.86226151	19.08578345	17.46889071	18.30638991
2	18.73679138	21.56445263	23.91718569	18.4884835	19.83291608
3	16.92153562	19.31214617	18.32069046	16.42576909	16.40201509
4	19.1208906	22.71627609	22.22129806	18.82715309	19.18099699
5	29.00605157	28.67019579	27.46512947	31.72703322	31.10849315
6	36.77029492	35.69128486	31.16495938	38.81870114	38.28374036
7	16.1013189	17.64099791	18.03467676	16.39695217	17.03292884
8	17.52271259	19.48582415	19.31454934	17.87941828	18.19703633
9	13.52111901	15.11310094	14.8467997	13.67301159	14.01627059
10	14.0380798	15.38624549	14.84508363	13.39567216	13.49462889
11	12.5225229	13.8304181	14.22212875	12.75898405	12.60962065
17	16.06341457	15.16297967	12.8925435	16.64415876	14.16751678
18	20.61808937	20.33631163	17.73191634	20.21986056	17.77014608
19	26.42662519	27.23656389	26.18529577	25.34609413	21.77919731
20	35.56759521	36.23814719	38.55046486	34.1352206	29.0842614
21	13.119866	12.56094287	12.67822891	13.50524422	16.08208638
22	15.14983545	15.3173178	16.01548455	15.49278214	18.985543
23	20.442575	20.99245933	22.70519025	20.7232943	24.87916724
24	21.64079337	21.52988779	22.9959287	21.93973382	24.44948925
33	10.4791114	11.07653669	9.766987933	10.7703752	13.36894311
34	9.198255255	9.700239164	9.650770713	9.580790207	13.01832947
35	7.502818102	7.355282232	7.787929925	8.289405817	10.99164565
36	8.362294127	8.725044877	10.41914541	8.620067687	11.76411589
37	12.79564585	12.27861179	12.42633629	13.40003543	12.67859375
38	15.05490795	14.33214446	13.99600882	16.02446137	15.75785508
39	11.42902288	10.78663829	10.47519473	12.24405812	11.86585651
40	11.82093617	11.34325553	10.32650461	11.82228344	11.91953384

Standard deviation Force balance (V)

10km/h	2.78m/s					
	R1	R2	R3	R4	R5	R6
-5deg	0.000765	0.000991	0.000603	0.001398	0.001227	0.001441
-2deg	0.001145	0.001022	0.000698	0.003507	0.002698	0.001847
0deg	0.000233	0.000234	0.000293	0.00032	0.000378	0.000306
2deg	0.001044	0.001405	0.000692	0.003881	0.002032	0.002342
5deg	0.000525	0.000845	0.00048	0.003179	0.001492	0.00094

20km/h	5.56m/s					
	R1	R2	R3	R4	R5	R6
-5deg	0.000789	0.001011	0.000591	0.001522	0.001371	0.001703
-2deg	0.000883	0.001053	0.000729	0.002879	0.002479	0.001867
0deg	0.000655	0.000813	0.000455	0.003624	0.001747	0.001314
2deg	0.001121	0.001309	0.000687	0.004071	0.002719	0.002971
5deg	0.000583	0.000841	0.000464	0.00318	0.001649	0.001347

30km/h	8.33m/s					
	R1	R2	R3	R4	R5	R6
-5deg	0.000797	0.001351	0.000662	0.002233	0.002256	0.002407
-2deg	0.001158	0.001036	0.000781	0.004056	0.003292	0.002731
0deg	0.000734	0.00087	0.000526	0.004033	0.002378	0.002202
2deg	0.001162	0.001427	0.00071	0.00429	0.002823	0.003021
5deg	0.000644	0.000693	0.000456	0.003101	0.002196	0.002281

40km/h	11.11m/s					
	R1	R2	R3	R4	R5	R6
-5deg	0.000983	0.001191	0.00085	0.003446	0.003911	0.004236
-2deg	0.001256	0.001116	0.000891	0.004594	0.004264	0.004021
0deg	0.000882	0.000991	0.00078	0.003831	0.004063	0.004511
2deg	0.001299	0.001525	0.001046	0.005204	0.004979	0.005393
5deg	0.000856	0.001044	0.00074	0.00447	0.003908	0.003696

50km/h	13.89m/s					
	R1	R2	R3	R4	R5	R6
-5deg	0.001258	0.001425	0.001092	0.005696	0.006386	0.005539
-2deg	0.001547	0.001513	0.001345	0.007059	0.00635	0.006168
0deg	0.001275	0.001414	0.001213	0.005769	0.006933	0.0058
2deg	0.001574	0.00186	0.001349	0.007258	0.006198	0.006823
5deg	0.001287	0.001574	0.001338	0.007402	0.005345	0.005776

60km/h	16.67m/s					
	R1	R2	R3	R4	R5	R6
-5deg	0.001572	0.001807	0.001406	0.00614	0.006917	0.008221
-2deg	0.001805	0.001727	0.001483	0.007187	0.007947	0.008275
0deg	0.001664	0.001735	0.001418	0.007406	0.007333	0.008748
2deg	0.001868	0.002002	0.001451	0.008135	0.007177	0.008812
5deg	0.001608	0.001574	0.001431	0.007343	0.007299	0.008622

Appendix D

Datasheet PLA / Tough PLA

Technical data sheet PLA

Ultimaker

Chemical composition	See PLA safety data sheet, section 3
Description	Ultimaker PLA filament provides a no-hassle 3D printing experience thanks to its reliability and good surface quality. Our PLA is made from organic and renewable sources. It's safe, easy to print with, and it serves a wide range of applications for both novice and advanced users
Key features	Good tensile strength and surface quality, easy to work with at high print speeds, user-friendly for both home and office environments, PLA allows the creation of high-resolution parts. There is a wide range of color options available
Applications	Household tools, toys, educational projects, show objects, prototyping, architectural models, as well as lost casting methods to create metal parts
Non-suitable for	Food contact and *in vivo* applications. Long term outdoor usage or applications where the printed part is exposed to temperatures higher than 50 °C

Filament specifications

	Value	**Method**
Diameter	2.85 ± 0.10 mm	-
Max roundness deviation	0.10 mm	-
Net filament weight	350 g / 750 g	-
Filament length	~ 44 m / ~ 95 m	-

Color information

Color	**Color code**
PLA Green	RAL 6018
PLA Black	RAL 9005
PLA Silver Metallic	RAL 9006
PLA White	RAL 9010
PLA Transparant	N/A
PLA Orange	RAL 2008
PLA Blue	RAL 5002
PLA Magenta	RAL 4010
PLA Red	RAL 3020
PLA Yellow	RAL 1003
PLA Pearl White	RAL 1013

Mechanical properties*

	Injection molding		3D printing	
	Typical value	**Test method**	**Typical value**	**Test method**
Tensile modulus	-	-	2,346.5 MPa	ISO 527 (1 mm/min)
Tensile stress at yield	-	-	49.5 MPa	ISO 527 (50 mm/min)
Tensile stress at break	-	-	45.6 MPa	ISO 527 (50 mm/min)
Elongation at yield	-	-	3.3%	ISO 527 (50 mm/min)
Elongation at break	-	-	5.2%	ISO 527 (50 mm/min)
Flexural strength	-	-	103 MPa	ISO 178
Flexural modulus	-	-	3,150 MPa	ISO 178
Izod impact strength, notched (at 23 °C)	-	-	5.1 kJ/m^2	ISO 180
Charpy impact strength (at 23 °C)	-	-	-	
Hardness	-	-	83 (Shore D)	Durometer

Electrical properties*

	Typical value	**Test method**	**Typical value**	**Test method**
Dissipation factor (at 1 MHz)	-	-	0.008	ASTM D150-11
Dielectric constant (at 1 MHz)	-	-	2.70	ASTM D150-11

Thermal properties

	Typical value	**Test method**
Melt mass-flow rate (MFR)	6.09 g/10 min	ISO 1133 (210 °C, 2.16 kg)
Heat detection (at 0.455 MPa)	-	-
Heat deflection (at 1.82 MPa)	-	-
Vicat softening temperature	-	-
Glass transition	~ 60 °C	ISO 11357
Coefficient of thermal expansion	-	-
Melting temperature	145 - 160 °C	ISO 11357
Thermal shrinkage	-	-

*See notes

Other properties

	Value	Test method
Specific gravity	1.24	ASTM D1505
Flame classification	-	-

Notes

Properties reported here are average of a typical batch. The 3D printed test specimens were printed in the XY plane, using the normal quality profile in Ultimaker Cura 2.1, an Ultimaker 2+, a 0.4 mm nozzle, 90% infill, 210 °C nozzle temperature, and 60 °C. The values are the average of five white and five black specimens for the tensile, flexural, and impact tests. The Shore hardness D was measured in a 7-mm-thick square printed using the normal quality profile in Utlimaker Cura 2.5, an Ultimaker 3, a 0.4 mm print core, and 100% infill. The electrical properties were measured on a 54-mm-diameter disk with 3 mm thickness printed in the XY plane, using the fine quality profile (0.1 mm layer height) in Ultimaker Cura 3.2.1, an Ultimaker 3, a 0.4 mm print core, and 100% infill. Ultimaker is constantly working on extending the TDS data.

Disclaimer

Version Version 4.002

Date November 19, 2018

Technical data sheet Tough PLA

Ultimaker

Chemical composition	See Tough PLA safety data sheet, section 3
Description	Ultimaker Tough PLA is a technical PLA filament with toughness comparable to Ultimaker ABS. Ideal for reliably printing technical models at large sizes, our Tough PLA offers the same safe and easy use as regular PLA
Key features	With an impact strength similar and higher stiffness compared to Ultimaker ABS, Tough PLA is less brittle than regular PLA and gives a more matte surface finish quality. Heat resistance is similar to standard PLA filaments, so printed parts should not be exposed to temperatures above 60 °C More reliable than ABS for larger prints, with no delamination or warping. Ultimaker Tough PLA is also compatible with Ultimaker support materials (PVA and Breakaway), giving full geometric freedom when designing parts
Applications	Functional prototyping, tooling, manufacturing aids
Non-suitable for	Food contact and *in vivo* applications. Long term outdoor usage or applications where the printed part is exposed to temperatures higher than 60 °C

Filament specifications

	Value	**Method**
Diameter	2.85 ± 0.05 mm	Ultra-fast CCS-based, dual-axis diameter gauge
Max roundness deviation	0.05 mm	Ultra-fast CCS-based, dual-axis diameter gauge
Net filament weight	750 g	-
Filament length	~ 96 m	-

Color information

Color	**Color code**
Tough PLA Black	RAL 9017
Tough PLA White	RAL 9003
Tough PLA Green	RAL 6038 (est.)
Tough PLA Red	RAL 3018

Mechanical properties*

	Injection molding		3D printing	
	Typical value	**Test method**	**Typical value**	**Test method**
Tensile modulus	-	-	1,820 MPa	ISO 527 (1 mm/min)
Tensile stress at yield	-	-	37 MPa	ISO 527 (50 mm/min)
Tensile stress at break	-	-	37 MPa	ISO 527 (50 mm/min)
Elongation at yield	-	-	3.1%	ISO 527 (50 mm/min)
Elongation at break	-	-	3.1%	ISO 527 (50 mm/min)
Flexural strength	-	-	78 MPa	ISO 178
Flexural modulus	-	-	2,490 MPa	ISO 178
Izod impact strength, notched (at 23 °C)	-	-	9 kJ/m^2	ISO 180
Charpy impact strength (at 23 °C)	-	-	-	
Hardness	-	-	79 (Shore D)	Durometer

Electrical properties*

	Typical value	**Test method**	**Typical value**	**Test method**
Dissipation factor (at 1 MHz)	-	-	0.014	ASTM D150-11
Dielectric constant (at 1 MHz)	-	-	2.62	ASTM D150-11

Thermal properties

	Typical value	**Test method**
Melt mass-flow rate (MFR)	6 - 7 g/10 min	(210 °C, 2.16 kg)
Heat detection (at 0.455 MPa)	-	-
Heat deflection (at 1.82 MPa)	-	-
Vicat softening temperature	63 °C	ISO 306
Glass transition	62 °C	DSC, 10 °C/min
Coefficient of thermal expansion	-	-
Melting temperature	151 °C	DSC, 10 °C/min
Thermal shrinkage	-	-

*See notes

Other properties

	Value	Test method
Specific gravity	1.22	ISO 1183
Flame classification	-	-

Notes

Properties reported here are average of a typical batch. The 3D printed test specimens were printed in the XY plane, using the fine quality profile in Ultimaker Cura 3.1, an Ultimaker 3, a 0.4 mm AA print core, 90% infill, 0.1 mm layer height, and 205 °C nozzle temperature. The values are the average of five white specimens for the tensile, flexural, and impact tests. The Shore hardness D was measured in a 7-mm-thick square printed as indicated above with 100% infill. The electrical properties were measured on a 54-mm-diameter disk with 3 mm thickness printed in the XY plane, using the fine quality profile (0.1 mm layer height) in Ultimaker Cura 3.2.1, an Ultimaker 3, a 0.4 mm print core, and 100% infill. Ultimaker is constantly working on extending the TDS data.

Disclaimer

Version Version 1.002

Date September 3, 2018

Adrian Leirvik Larsen

Aerodynamic validation of a Formula Student race car

NTNU
Kunnskap for en bedre verden

NTNU revolve